

Brownian Dynamics Simulations of Protein Equilibria in the Presence of a Charged Surface

Dissertation
zur Erlangung des Doktorgrades
der Naturwissenschaften

vorgelegt beim Fachbereich Physik
der Johann Wolfgang Goethe - Universität
in Frankfurt am Main

von
Christian Gorba
aus Dinslaken

Frankfurt 2004

vom Fachbereich Physik der
Johann Wolfgang Goethe-Universität als Dissertation angenommen.

Dekan: Prof. Dr. Wolf Aßmus

Gutachter: Prof. Dr. Werner Mäntele
Prof. Dr. Volkhard Helms

Datum der Disputation: 3.11.2004

Zusammenfassung

Die vorliegende Arbeit befasst sich mit der Brownschen Dynamik von Proteinen in der Nähe einer homogen geladenen ebenen Membran. Letztere kann neben der homogenen Ladung auch noch an beliebigen Stellen Ladungs- und van der Waals-Domänen enthalten. Die Dynamik der Teilchen wird hier mit Hilfe von Computersimulationen untersucht. Beispiele für solche Phänomene finden sich in der Natur in großer Zahl. Die Photosynthese, in der Sauerstoff aus Kohlendioxid erzeugt wird, war Hauptmotivation für die vorliegende Arbeit. Sie ist einer der wichtigsten Naturvorgänge in bezug auf die Entstehung von Leben auf der Erde. Die Umgebung, in der die photosynthetischen Vorgänge ablaufen, entspricht im wesentlichen dem oben beschriebenen System aus diffundierenden Teilchen und geladener Membran. Diese geladene Wand wäre somit z.B. die Lipidmembran des Teils eines Bakteriums, der für die Photosynthese zuständig ist, die Ladungs- und van der Waals-Domänen entsprechen beispielsweise den Membranproteinkomplexen, wie den lichtabsorbierenden Komplexen (Light Harvesting Complexes, kurz LHC), dem Reaktionszentrum, sowie dem sogenannten Cytochrom bc_1 -Komplex. Die Brownschen Teilchen schließlich stellen jene Moleküle (Cytochrom c Proteine, kurz cyt c) dar, welche den bei der Photosynthese notwendigen Elektronentransfer vom bc_1 -Komplex zum Reaktionszentrum (Reaction Center, kurz RC) übernehmen. Die internen Vorgänge der Photosynthese wie Lichtabsorption, Ladungstrennung usw. sind hier nicht Gegenstand der Untersuchung, sondern einzig die Dynamik der cyt c Moleküle oberhalb der Lipidmembran und deren Annäherung an das RC und den bc_1 -Komplex (Elektronenabgabe bzw. -aufnahme). In bisherigen Untersuchungen wurde eine solche Assoziation nur jeweils paarweise studiert, d.h. mit *einem* diffundierenden Protein und z.B. *einem* bc_1 -Komplex. Im sogenannten Periplasma über der Membran gibt es allerdings eine Vielzahl von Molekülen, die sich entsprechend gegenseitig beeinflussen. Es handelt sich also um Mehr-Teilchen-Systeme. Daher wird in dieser Arbeit eine Vielzahl (max. $O(100)$) von diffundierenden cyt c betrachtet. Neu an diesem Ansatz ist also die Berück-

sichtigung der Möglichkeit, daß nicht nur ein einzelnes cyt c nahe der Membranproteine lediglich zwischen RC und bc_1 -Komplex hin- und herdiffundiert, sondern auch zurück in Lösung gehen kann. Dort kann es dann mit weiteren cyt c Molekülen wechselwirken, und schließlich kann ein anderes cyt c an die Membranoberfläche gelangen und dort den Elektronentransfer bewerkstelligen. Dies hat vermutlich einen großen Einfluß auf die Häufigkeit der Elektronentransfers.

Da es bisher kein in der Literatur bekanntes Software-Werkzeug gibt, das Simulationen, wie sie in dieser Arbeit beschrieben werden, erlaubt, musste zunächst ein geeignetes Programm entworfen und entwickelt werden. Hierzu wurde C++ benutzt, weil diese Sprache einerseits schnell ist und andererseits objektorientiertes Programmieren erlaubt, wodurch der Source Code leichter zu warten und erweiterbar wird. Um den Rechenaufwand bewältigen zu können, war eine vereinfachende Systemmodellierung notwendig. Daher werden die cyt c Moleküle in dieser Arbeit als sphärische Teilchen mit einem Monopol- und einem Dipolmoment beschrieben. Die Bewegung der Teilchen wird mittels Brownscher Dynamik berechnet. D.h., erstens werden Zeitskalen betrachtet, auf denen sich die Teilchen im thermischen (Geschwindigkeits-) Gleichgewicht mit dem Solvens befinden, und zweitens wird der Solvens selbst nicht explizit modelliert. Die Membran wird als starre, geladene Oberfläche beschrieben, und Membranproteine können als geladene van der Waals-Kugeln in die Oberfläche eingebettet werden. Damit schließt sich sozusagen der Kreis zum einleitenden Satz: es wurde ein Programm zur Untersuchung der Brownschen Dynamik von Proteinen in der Nähe einer homogen geladenen ebenen Wand entwickelt. Dieses recht allgemeine Modellsystem kann auf verschiedene biologische Systeme angewandt werden, wobei es in der vorliegenden Arbeit ausschließlich um eine Beschreibung der Gleichgewichtsdynamik von cyt c über einer Membran geht.

Bevor im letzten Kapitel Ergebnisse von Rechnungen inklusive Membranproteinen beschrieben werden, liegt das Hauptaugenmerk auf der Untersuchung von Konzentrationsprofilen in der Simulationsbox mit strukturloser, geladener Membran. Damit ist die Verteilung der Modellproteine im Simulationsvolumen oberhalb der Membran gemeint. Diese Proteinverteilung ist naturgemäß stark abhängig von der Art der Wechselwirkungen sowohl der Teilchen untereinander als auch von der Art der Wechselwirkungen mit der Wand. Es werden elektrostatische und van der Waals Wechselwirkungen zwischen den Brownschen Partikeln, sowie ebenso elektrostatische und van der Waals Kräfte zwischen Brownschen Teilchen und Membran berücksichtigt. Im folgenden wird auf die wichtigsten Teile der einzelnen Kapitel

näher eingegangen.

Im Einführungskapitel 1 werden zunächst grundsätzliche Bemerkungen über das Wechselspiel zwischen Theorie, Experiment und Computersimulation gemacht. Die Simulation ist demnach eine nützliche Schnittstelle zwischen den anderen beiden „Disziplinen“. Im Anschluß daran wird in Abschnitt 1.1 erklärt, was mit Brownscher Bewegung gemeint ist und welche immense Bedeutung sie für viele Prozesse in biologischen Zellen hat. Weiter geht es mit kurzen Beschreibungen der wichtigsten zwei „Referenzsysteme“ für die vorliegende Arbeit in den Abschnitten 1.2 und 1.3. Neben der schon mehrfach erwähnten Photosynthese gehört auch die Atmungskette dazu. Der darauffolgende Abschnitt 1.4 beschreibt das in allen Simulationen als Brownsches Teilchen benutzte Protein *cyt c*. Eine bekannte 3D-Kristallstruktur (stellvertretend aus Pferdeherz) wird dargestellt und gezeigt, daß die Ladungsverteilung tatsächlich gut durch einen Monopol- und einen Dipolterm beschrieben werden kann. Es folgt mit den Abschnitten 1.5 und 1.6 eine Einführung in den Aufbau biologischer Membranen, und es werden wichtige Experimente zur Bindung von *cyt c* an Membranen vorgestellt. Danach werden in Abschnitt 1.7 zwei wichtige Simulationstechniken gegenübergestellt. Dies sind die Moleküldynamik und die Brownsche Dynamik. Warum, wie schon zuvor gesagt, letztere in dieser Arbeit benutzt wird, wird dort ausführlicher erläutert.

Im Kapitel 2 werden die (mathematischen) Methoden zur Beschreibung der zu simulierenden Systeme und die Behandlung der Randbedingungen erläutert. Die Brownsche Dynamik und ihre statistische Natur wird ausführlich in Abschnitt 2.1 erklärt. In Unterabschnitt 2.1.2 findet man die Bewegungsgleichungen (Langevin Gleichungen) sowie deren Lösung. Die Wechselwirkungsterme, die in die Bewegungsgleichungen einfließen, werden im Abschnitt 2.2 hergeleitet (siehe auch: C. Gorba and V. Helms. Diffusional dynamics of cytochrome *c* molecules in the presence of a charged surface. *Soft Materials*, 1:187, 2003). Dazu gehört die hydrodynamische Wechselwirkung, welche durch den Solvens vermittelt wird und durch Matrizen beschrieben werden kann (Unterabschnitt 2.2.1). Ferner gibt es die durch Ladungen hervorgerufenen elektrostatischen Kräfte (Unterabschnitt 2.2.2) und die bei geringen Abständen dominierenden van der Waals Kräfte. Letztere sind quantenmechanischer Natur und werden hier durch empirische Potentiale beschrieben (Unterabschnitt 2.2.3). Eine Beschreibung des Simulationssystems und der Randbedingungen findet man im Abschnitt 2.3. Benutzt werden sowohl eine Kombination aus reflektierenden und 2-dimensionalen periodischen Randbedingungen (Unterabschnitt 2.3.2), als auch eine

Kombination aus reflektierenden Rändern und einer offenen Wand (Unterabschnitt 2.3.3). Durch diese können Brownsche Teilchen in die Simulationsbox herein- oder aus ihr herausfließen. Diese als Schnittstelle zwischen Simulationsbox und Gebieten mit freier Diffusion fungierende offene Wand wird mittels eines neuentwickelten Einfügealgorithmus realisiert (siehe auch: T. Geyer, C. Gorba and V. Helms. Interfacing Brownian dynamics simulations. *J. Chem. Phys.*, 120:4573, 2004).

Das Kapitel 3 beschreibt Details des entwickelten Computerprogramms. Es werden die entwickelten Klassen, welche die Eigenschaften und Funktionalitäten der verschiedenen Teilobjekte des Simulationssystems, wie z.B. des Objektes „Protein“, modellieren, vorgestellt. Außerdem findet man eine Analyse der Programmpformance, d.h. Aussagen darüber, welche Teilberechnungen während einer Simulation wieviel CPU-Zeit verbrauchen.

Danach geht es schließlich zu den einzelnen Simulationen und deren Ergebnissen. Als erstes behandelt Kapitel 4 Simulationen mit geschlossener Wand oberhalb der Membran. D.h., Teilchen können die Simulationsbox weder verlassen, noch können neue Teilchen hinzukommen. Diese Form der Randbedingungen war im Laufe des Projektes als erstes verfügbar und dienten im wesentlichen als Test für verschiedene Szenarien. Im Abschnitt 4.1 wird ein einfacher Test des Source Codes vorgestellt, mit dem geprüft wird, ob der Algorithmus zur Lösung der Langevin Gleichungen richtig implementiert wurde. Dabei handelt es sich um die freie Brownsche Bewegung zweier Teilchen. Es folgt die Auswertung einiger Rechnungen mit und ohne hydrodynamische Wechselwirkung in Abschnitt 4.2. Es werden hier Diffusionskoeffizienten und Konzentrationsprofile ermittelt. Der Vergleich liefert Aussagen über den Einfluß der verwendeten Standardhydrodynamik. Der nächste Abschnitt 4.3 befasst sich mit dem Phänomen des „molecular crowding“. Biologische Zellen sind in der Regel sehr stark von allen möglichen Molekülen bevölkert. Man sollte daher erwarten, daß es häufig einen indirekten Einfluß von nicht direkt an den betrachteten Prozessen beteiligten Teilchen gibt. Dem wird hier in einem vorsichtigen ersten Schritt dadurch Rechnung getragen, daß zusätzliche Brownsche Teilchen in die Box gepackt werden, die ungeladen sind und somit nicht an der elektrostatischen Wechselwirkung mit der Membran teilnehmen. Allein durch ihre Teilnahme an der hydrodynamischen und an den van der Waals Wechselwirkungen verändern sie das Diffusionsverhalten der hier interessierenden cyt *c* Moleküle und deren Verteilung oberhalb der Membran.

Kapitel 5 basiert auf den Ausführungen in „C. Gorba, T. Geyer and V. Helms. Brownian dynamics simulations of simplified cytochrome *c* molecules in the presence of a charged sur-

face. *J. Chem. Phys.*, 121:457". Dort werden nun mit Hilfe des weiter oben schon erwähnten Einfügealgorithmus Teilchenfluktuationen zugelassen. Auf diese Weise ist es möglich, den interessierenden Bereich nahe der Wand von einem Bereich freier Diffusion (bulk) zu entkoppeln und damit u.a. Rechenzeit zu sparen. Mit Simulationen, die dieses neue Verfahren benutzen, ist es gelungen, experimentelle Ergebnisse zum Bindungsverhalten von cyt *c* an Lipidmembranen qualitativ zu reproduzieren [1]. Es geht hier im wesentlichen um das Sättigungsverhalten der sogenannten Bindungsisotherme (u.a. Abschnitt 5.3). Diese beschreiben den Anteil der an die Membran gebundenen cyt *c* Moleküle in Abhängigkeit von der Gesamtkonzentration. Nachdem in Abschnitt 5.4 gezeigt wird, wie man durch Verwendung einer effektiven Simulationsbox periodische Randbedingungen umgehen kann, wird in Abschnitt 5.5 ein erster Schritt in Richtung Einbeziehung von Membranproteinen unternommen. Bisher wurde ja nur eine strukturlose Oberfläche benutzt. Bevor diese sehr einfachen als Punktladungen realisierten Reaktionszentren in Unterabschnitt 5.5.2 eingebaut werden, beschreibt Unterabschnitt 5.5.1 den Einfluß der van der Waals Wechselwirkung der Membran mit den Brownschen Teilchen. Dieser erweist sich als recht gering. Die Reaktionszentren bewirken eine effektive Verringerung der zur Verfügung stehenden Membranfläche und damit das Einsetzen der cyt *c*-Sättigung bei kleineren Konzentrationen als ohne diese zusätzlichen Ladungen.

Im Kapitel 6 werden dann schließlich vereinfachende Modelle für ein Photosystem vorgestellt. Anhand mittlerweile bekannter 3D-Strukturen wurde die Geometrie der beteiligten Membranproteine und deren Ladung abgeschätzt und auf das Simulationssystem angewandt. Wesentliche Bestandteile dieses Modells sind die Reaktionszentren innerhalb eines Rings aus Lichtsammelkomplexen (LHC). Es zeigt sich, daß die Verteilung von cyt *c*, welches mit diesen Membrankomplexen wechselwirkt, deren Struktur in etwa abbildet. Ein Elektronentransfer kann nur stattfinden, wenn cyt *c* auch tatsächlich die Möglichkeit besitzt, das Reaktionszentrum einer photosynthetischen Einheit zu erreichen, um dort sein Elektron abzugeben. Die farbcodierten Verteilungsdiagramme zeigen aber für unsere Modelle eine vernachlässigbare Dichte. Cyt *c* kommt also gar nicht durch den Wall von Lichtsammelkomplexen mit seiner ringförmigen Struktur hindurch und damit auch nicht nahe genug an das Reaktionszentrum heran. Die Schlußfolgerung ist, daß die benutzten Modelle für solche Photosysteme offensichtlich nicht ausreichen. Es ist möglich, daß diese Art der Modellierung der photosynthetischen Einheiten prinzipiell zu ungenau ist. Es läßt sich aber auch die Hypothese aufstellen, daß der Ring aus Lichtsammelkomplexen in Wirklichkeit nicht voll-

ständig geschlossen ist, sondern an einer Stelle eine „Lücke“ aufweist. Durch diese könnten sich die *cyt c* Moleküle hindurchbewegen und zum Reaktionszentrum gelangen. Das gegenwärtig in der Literatur diskutierte PufX Polypeptid an einer Stelle des Ringes, wo eigentlich ein Lichtsammlerkomplex zu erwarten wäre, könnte dafür verantwortlich sein, daß an dieser Stelle genug Platz für *cyt c* bliebe, um den Ring zu „durchtunneln“.

Es folgt dann in Kapitel 7 die Zusammenfassung der Arbeit mit den Schlußfolgerungen und einem Ausblick auf die Forschung, die mit Hilfe der vorliegenden Ergebnisse und des Source Codes möglich sein sollte. Der Anhang gibt dann noch einen Überblick über die benutzten Systemparameter in den verschiedenen Simulationen und zeigt einige Details der Ein- und Ausgabe des vorgestellten Programms.

Contents

1	Introduction	5
1.1	Brownian motion in biological cells	5
1.2	Respiratory chain	9
1.3	Photosynthesis	9
1.4	Horse heart cytochrome <i>c</i>	14
1.5	Biological membranes	16
1.6	Binding of cyt <i>c</i> to membranes	17
1.7	Molecular simulation techniques	18
1.7.1	Molecular dynamics	19
1.7.2	Brownian dynamics	22
2	Brownian dynamics methods	25
2.1	Brownian dynamics (BD)	25
2.1.1	Introduction	25
2.1.2	Equations of motion and their solution	27
2.2	Interactions	29
2.2.1	Hydrodynamic interaction	29
2.2.2	Electrostatic interaction	34
	Interaction between two cyt <i>c</i> molecules: dipolar sphere model	34
	Poisson-Boltzmann equation	35
	Interaction between cyt <i>c</i> and a charged planar surface	35
2.2.3	Van der Waals interaction	37
	Interaction between two cyt <i>c</i> molecules	37
	Interaction between cyt <i>c</i> and a planar surface	38

2.3	Simulation system and boundary conditions	40
2.3.1	Reflecting boundary conditions	41
2.3.2	2-dimensional periodic boundary conditions in <i>xy</i> -direction.	42
2.3.3	Dynamic particle insertion algorithm	43
3	Implementation	45
3.1	Structure of CESIP	45
3.2	Computational performance	47
4	Simulations and results for $N=\text{const.}$	51
4.1	A simple test of the source code	51
4.2	The influence of hydrodynamic interactions	54
4.3	A first step towards macromolecular crowding	59
5	Simulations and results for $N\neq\text{const.}$	65
5.1	Equilibration	65
5.2	Concentration profiles and bond length	66
5.3	Binding isotherms	68
5.4	Effective membrane area	69
5.5	Towards membrane proteins	71
5.5.1	Influence of the van der Waals potential depth and the surface charge of the membrane	72
5.5.2	Reaction centres	74
6	Simulations and results including a simple model for photosynthetic units	79
7	Summary, conclusions and outlook	87
7.1	Summary and conclusions	87
7.2	Outlook	90
A	System parameters	93
B	Input files	101
C	Output files	105

Chapter 1

Introduction

This thesis presents results from computer simulations for the Brownian motion of cytochrome *c* (cyt *c*) molecules in the presence of a charged surface. These were obtained with a program called CESIP (Cellular Simulation Package) which was especially developed by the author for that purpose. The motivation for studying Brownian motion of these molecules is the diversity of biological processes in which cyt *c* is involved, especially in photosynthesis and in the respiratory chain. Furthermore, in almost all biological systems membranes and thus, charged surfaces, are present. In this thesis the underlying methods, the way they are implemented (shortly) and the results of various simulations using the code are presented. At this point it is instructive to point out the role that simulations play in natural sciences. Figure 1.1 illustrates their dual role: simulations are supposed to build a bridge between models and theoretical predictions on the one hand, and between models and experimental results on the other [2]. Thus, simulations are some kind of hybrid of theory and experiment. Because of this connecting role and the way in which simulations are conducted and analysed, these techniques are often referred to as “computer experiments”.

1.1 Brownian motion in biological cells

Brownian motion is named after the Botanist Robert Brown. In 1827 he observed the irregular motion of pollen grains in water [3]. The origins of that motion are collisions of these grains with the water molecules. In more general terms, Brownian motion is a unique form of random motion of “large molecules” in solution powered by thermal energy, i.e., by ran-

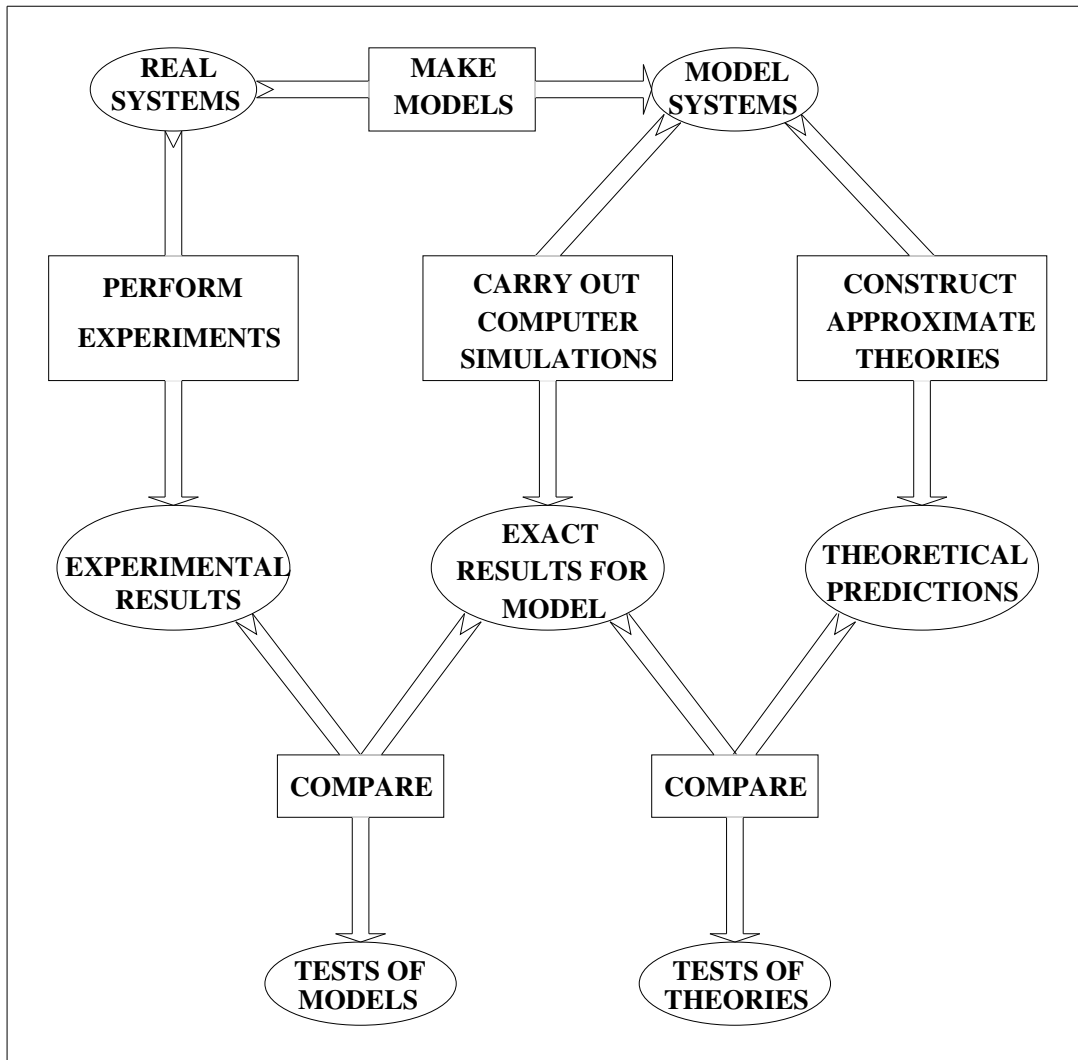


Figure 1.1: The connection between experiment, theory and computer simulation (from ref. [2]).

dom collisions with the solvent molecules. These “large molecules” are called colloidal or Brownian particles. It has to be explained what is meant by “large molecules”. The quotation marks hint that it is quite a wide range of system sizes that can be handled by Brownian dynamics techniques. This is very well explained in an introductory section in ref. [4]:

“[...] Colloidal systems are thus solutions of ‘large molecules’. The large molecules are the colloidal or Brownian particles. These should be large compared to the solvent molecules, but still small enough to exhibit thermal motion (in the present context more commonly referred to as Brownian motion). Particles in solution are colloidal particles when ‘they are large, but not too large’. The lower and upper limits for the size of a particle to be classified as a colloidal particle are not sharply defined.

The minimum size of a colloidal particle is set by the requirement that the structure of the solvent on the molecular length scale enters the interaction of the colloidal particle with the solvent molecules only in an averaged way. Many solvent molecules are supposed to interact simultaneously with the surface of a single colloidal particle. The interaction of the colloidal particle and the solvent molecules can then be described by macroscopic equations of motion for the fluid, with boundary conditions for the solvent flow on the surface of the colloidal particle. Brownian motion is then characterised through macroscopic properties of the solvent (such as its viscosity and temperature). This is feasible when the size of the colloidal particle is at least about ten times the linear dimension of a solvent molecule. The minimum size of a Brownian particle is therefore $\simeq 1$ nm.

The maximum size of a colloidal particle is set by the requirement that it behaves as ‘a large molecule’, that is, when it shows vivid thermal motion (=Brownian motion). Thermal motion is relevant only when thermal displacements are a sizable fraction of the linear dimension of the particle during typical experimental time ranges. A brick in water (before it sunk to the bottom of the container) shows thermal motion also, but the displacements relative to its own size on a typical experimental time scale are extremely small. Thermal motion of bricks in water is irrelevant to the processes in such systems. As soon as thermal motion is of importance to processes in solutions of large objects, these objects are classified as colloidal or Brownian particles. This limits the size of colloidal particles to $\simeq 10$ μm . Besides the very small thermal excursions of the position of a brick due to thermal collisions with solvent molecules, it also moves to the bottom of a container in a relatively short time. This may also happen for smaller objects than a brick (and is then referred to as sedimentation) in a time span that does not allow for decent experimentation on, for example,

Brownian displacements. This provides a more practical definition of the upper limit on the size of an object to be classified as a Brownian particle: displacements under the action of the earth's gravitational field should be limited to an extent that allows for experimentation on processes for which Brownian motion is relevant. For practical systems this sets the upper size limit again to about $\simeq 10 \mu\text{m}$, and sometimes less, depending on the kind of experiment one wishes to perform [...] Clearly, without a gravitational field being present, the latter definition of the upper limit for the colloidal size is redundant..."

As mentioned above, Brownian motion plays an important role in many processes in biological cells. Apart from photosynthesis and the respiratory chain which are the systems that are addressed in this work, Brownian motion is vital for the functioning of many "motor" proteins [5]. E.g., new research suggests that random motion of such "motors" plays the major role in moving enzymes and other chemicals inside cells. Kinesin is such a protein: within a cell these molecules work like "cellular tow trucks" which pull small packages of chemicals along pathways called microtubules. The common explanation is that this motion is a deliberate one along the microtubule paths, supplied by energy from ATP (adenosine triphosphate): the kinesins are widely believed to use their two leg-like "heads" to walk along the microtubules. In ref. [6], however, the authors argue that the same motion is really random motion constrained by chemical switching carried out by ATP. They call that kind of motion rectified motion. The authors' conclusion goes as far as saying: "We're arguing that Brown really had discovered the secret of life."

Another example for Brownian motion in cells is the aggregation and segregation of photosystems in higher plant thylakoid membranes [7]. The Brownian motion in that case is the lateral movement of the photosystems within the membrane plane.

Especially association processes between proteins are governed by Brownian dynamics. It should be noted that many kinds of forces are involved in Brownian dynamics. The random nature of Brownian motion without any external forces always leads to a zero displacement on average and Brownian processes would therefore never have a direction. Any directionality observed is always caused by interparticle and external forces. In association kinetics, e.g., electrostatics is the most important force as long as particles are not too close.

As already mentioned, Brownian motion is also an important part of the machineries of respiratory and photosynthesis, the two processes that initially gave the motivation for the work presented in this thesis. The role that Brownian motion plays there is described in the next two sections.

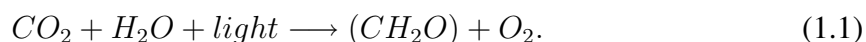
1.2 Respiratory chain

Respiration is a fundamental process in molecular bioenergetics, in which food molecules are oxidised to carbon dioxide and water [8]. The released energy is stored in ATP (adenosine triphosphate) and can be used for many activities of the cell. The respiratory chain consists of three membrane enzyme complexes which are connected by two mobile electron-carriers. The integral membrane proteins are the NADH reductase, cytochrome *c* reductase and cytochrome *c* oxidase. The electron-carriers are ubiquinone and cyt *c*. The latter is the molecule of interest in this work. This will become clearer in the next section. Since the systems are very similar, the connection to Brownian motion will be explained in the following section about photosynthesis.

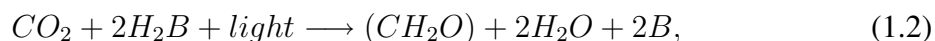
1.3 Photosynthesis

Photosynthesis is the second fundamental process in molecular bioenergetics forming the basis for life on earth together with respiration [9, 10]. Briefly, in photosynthesis energy from sunlight is transformed into chemical energy. That chemical energy is stored in carbohydrates and other organic molecules. The whole machinery includes photoexcitation, transfer of electrons and protons, and various chemical reactions. All these steps take place in several large integral membrane proteins, characterised over the past 15 years by X-ray and electron diffraction.

The following is based on comments in the textbooks of refs. [9] and [10]. About 3.5 billion years ago a new type of prokaryote bacteria appeared on earth that were able to do photosynthesis by using electrons from water. The overall reaction in photosynthesis of plants and the aforementioned cyanobacteria is the production of carbohydrates together with molecular oxygen which can be considered as a waste product; obviously a waste product with extraordinary consequences. The light induced reaction can be written in the following form:



More generally, one has to write



where H_2B is a reduced reactant and B an oxidised product like sulfur S , e.g., because purple bacteria do not produce molecular oxygen from water as electron source.

Figure 1.2 illustrates the machinery for the photosynthesis of purple bacteria and represents the major membrane proteins involved. **The diffusion of the cyt c molecules (green rectangle) is the subprocess which is addressed in this thesis. In other words, the topic is the dynamics in the periplasm above the membrane.**

The organisation of the photosynthetic apparatus of the purple non-sulfur bacterium *Rhodospira rubra* was elucidated in 1999 by electron microscopy [12]. It is the reference system used to build the simulation model for this thesis: the photosynthetic machinery is located in tubular membranes that are subcompartments of spheroplasts within the cell. These spheroplasts have a diameter of about $3.5 \mu\text{m}$. Figure 1.3 shows an electron micrograph of such a spheroplast. The tubular membranes within the spheroplasts were obtained by freeze-drying. One single tube is depicted in Figure 1.4. From their experiments Jungas *et al.* derived a model for the photosynthetic units and their distribution on the tubular membranes. From 1.4 one might already guess a regular, grid-like, pattern of photosynthetic units on the tubular membrane surface. The proposed pattern and the suggested model for the units are shown in Figs. 1.5 and 1.6, respectively. From the dimensions shown in Figures 1.5 and 1.6 the minimum size of a simulation box can be derived. That is the box volume which should be available for properly simulating diffusional behaviour of cyt c molecules in such a system. The length of a photosynthetic unit is roughly $x \simeq 20 \text{ nm}$, its width about $y \simeq 12 \text{ nm}$. Therefore the membrane area should not be smaller than that. Furthermore, the minimum height of the box can be estimated from the diameter of cyt c which is $2R = 3.32 \text{ nm}$. It should not be smaller than a couple of molecule diameters. For that reason a typical box size used in our simulations is $20 \text{ nm} \times 20 \text{ nm} \times 20 \text{ nm}$ (see later). Of course the real geometry is more complicated than a simple rectangular box, but on the desired level of approximation (namely learning about the overall diffusional behaviour) this should be a good choice.

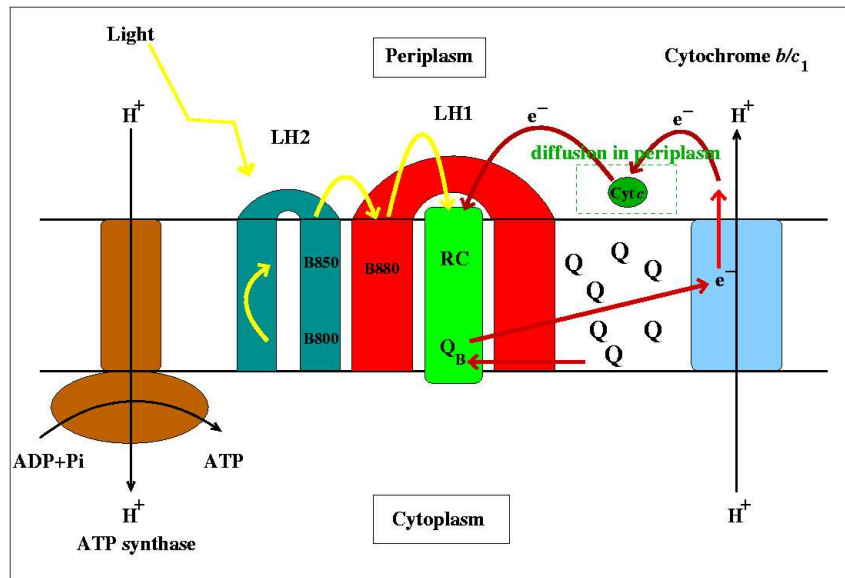


Figure 1.2: Overview of photosynthetic processes as they occur in purple bacteria (from ref. [11]). The photon energy (yellow arrows) is captured by the bacteriochlorophyll *a* (Bchl_a) pigments (labelled B800 and B850 to indicate the approximate wavelength in nanometres of maximal absorption) in the antenna light harvesting complex 2 (LH2) (cyan). It is then passed to the LH1 Bchl_a (B880, red, which also acts as a light-harvester), and then to a pair of Bchl_a molecules (not shown) in the reaction centre (RC). The direction of the electron flow (red arrows) across the photosynthetic membrane is from Bchl_a, which is oxidised, to a primary electron acceptor, ubiquinone (UQ_A, not shown), which is reduced. Subsequently, the electron is transferred from UQ_A to the secondary electron acceptor ubiquinolone UQ_B (shown here as Q_B). A second RC turnover results in the complete reduction of UQ_B⁻ to UQ_BH₂. The fully reduced UQ_BH₂ is replaced in the RC with an oxidised ubiquinolone (shown as Q) and passes its electrons to the next redox component in the cyclic electron transport path, the cytochrome *b/c*₁ complex (blue). The electrons (e^-) are returned to the RC through cyt *c* (dark green). A transmembrane proton gradient is established which drives ATP synthase (brown), producing ATP (ADP + P_i, adenosine diphosphate and inorganic phosphate).

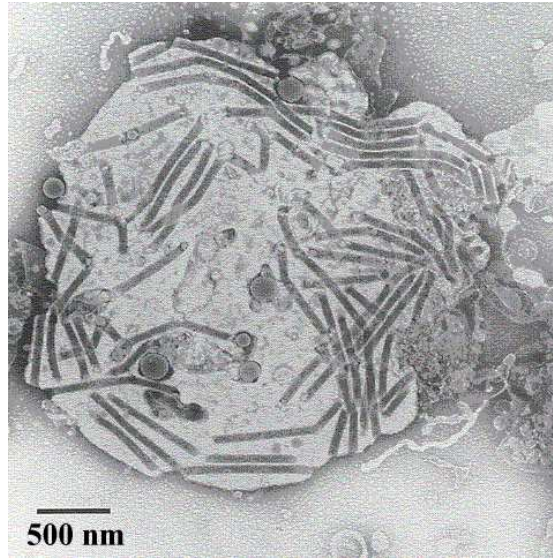


Figure 1.3: Electron micrograph of a spheroplast of *Rhodospirillum rubrum* (from ref. [12]).

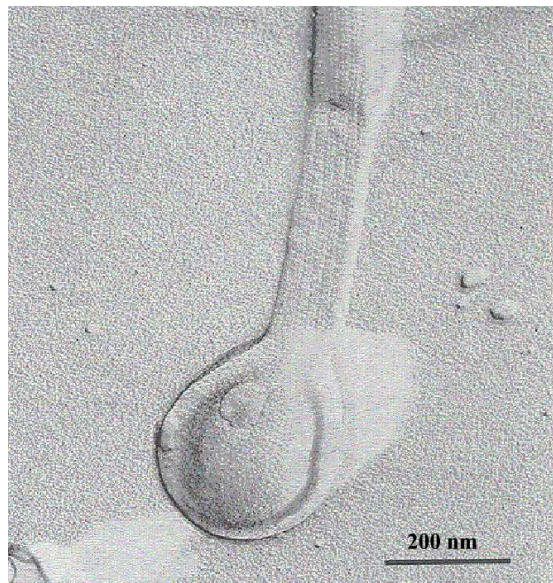


Figure 1.4: Tubular membrane of *Rhodospirillum rubrum* (from ref. [12]).

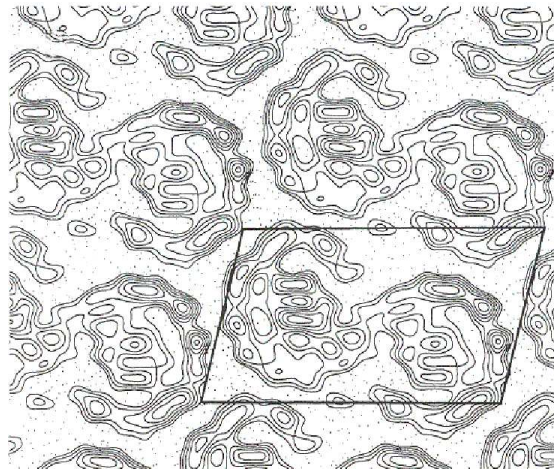


Figure 1.5: Projection map at 2 nm resolution of the tubular flat membrane from *Rhodobacter sphaeroides*. The unit cell ($a = 19.8$ nm, $b = 12.0$ nm and $\gamma = 103^\circ$) is outlined in black. Positive density representing the protein is shown as solid lines and negative density as dotted lines (from ref. [12]).

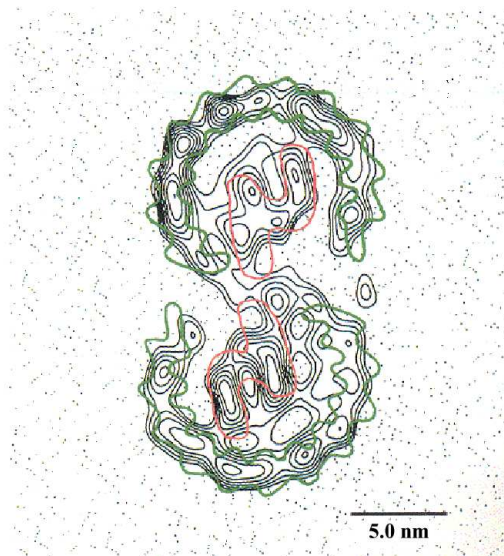


Figure 1.6: Proposed model of the photosynthetic unit of *Rhodobacter sphaeroides*. The photosynthetic unit is viewed from above the membrane. The projection structure of the RC of *Rhodobacter sphaeroides* [13] and the projection map of 3/4 of LH1 of *Rhodospirillum rubrum* [14] are shown in red and green, respectively (from ref. [12]).

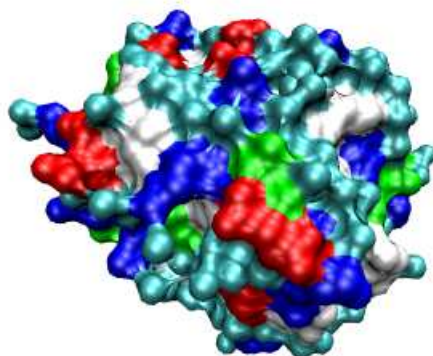


Figure 1.7: Surface representation of horse heart cyt *c* (elucidated by X-ray diffraction, resolution 0.19 nm, PDB (Protein Data Bank at <http://www.rcsb.org/pdb/>) code 1HRC [15]). Colours are chosen according to the residue types. Basic (positively charged) residues are coloured in blue, acidic (negatively charged) residues are coloured in red. Green is chosen for polar and white for non-polar residues.

1.4 Horse heart cytochrome *c*

In this section the main characteristics of the Brownian molecule of interest in this work are briefly resumed. Cyt *c* is essentially a spherical protein. Figures 1.7 and 1.8 show two representations from different perspectives of horse heart cyt *c* to get an idea of its approximate geometry and its secondary structure. Though photosynthesis was already mentioned very often, in the following we refer to cyt *c* from horse heart which is very well known. Cyt *c* molecules from different species are usually very similar in their structures (homologous) and on the level of approximation used here the use of the physical properties of horse heart cyt *c* should be sufficient. In ref. [16] it was shown that the charges in cyt *c* are distributed asymmetrically. The conclusion is that besides a monopole it also has a dipole moment. Figure 1.9 shows the equipotential lines around horse ferrocytochrome *c* in one parallel section perpendicular to the *y*-axis and the projection of the resulting dipole axis. From that the so-called dipolar sphere model (DSM) was developed [17]. In this work we assume a spherical protein of radius $R = 1.66$ nm with a net monopole of $q \simeq +7.3 e_0$ and a dipole moment of $\mu = 250$ Debye.

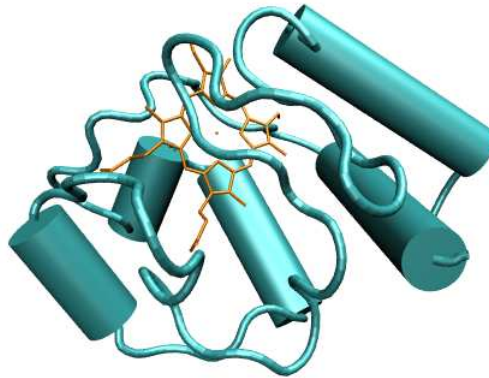


Figure 1.8: Cartoon representation of horse heart cyt *c* including the heme complex (PDB code 1HRC [15]).

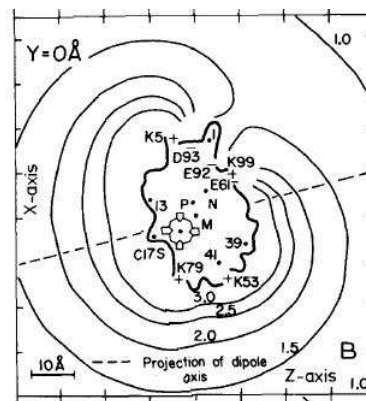


Figure 1.9: Equipotential lines around horse ferredoxin *c* in a parallel section perpendicular to the *y*-axis which contains the heme and the centre of mass M. The potentials are given in units of $k_B T/e_0$. Only charges (+, -) and α -carbons (.) of amino acids between $y + 2 \text{ \AA}$ and $y - 2 \text{ \AA}$ are indicated. The following abbreviations are used: D (aspartic acid), E (glutamic acid), K (lysine), R (arginine), P (centre of positive charge), N (centre of negative charge), M (centre of mass). The projection of the dipole axis on the plane $y = 0$ is represented by the dashed line (from ref. [16]).

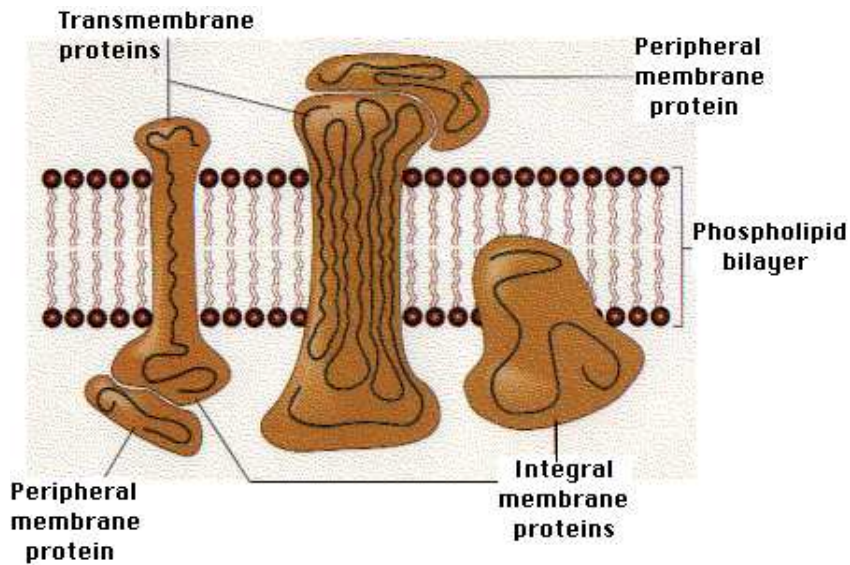


Figure 1.10: A typical phospholipid bilayer with its transmembrane and integral membrane proteins. This picture is taken from the internet resource at <http://biology-pages.info>.

1.5 Biological membranes

Biological membranes consist of lipid bilayers usually interspersed with a variety of membrane proteins. Figure 1.10 shows a schematic picture of a typical membrane. The lipid bilayers themselves are essentially made of phospholipids. Figure 1.11 shows their basic components. Phospholipids consist of two fatty acids (one saturated and one unsaturated) and a head group. The head is hydrophilic and the fatty acid tails are hydrophobic. There is a “special” region of the head group that differs between various phospholipids.

Such membranes are of course not static, immobile structures. But the processes that are supposed to be studied here (namely the overall behaviour of the surrounding Brownian particles) do not necessarily need to include the dynamics of the bilayer (this would actually be a very costly task with regard to the necessary computer power). Thus, in our coarse-grained description the bilayer is modelled as flat, immobile and homogeneously charged. The surface charge of a membrane therefore mostly depends on the charge of the head groups and it can be estimated as follows. Consider a membrane only consisting of a homogeneous distribution of dioleoyl phosphatidylglycerol (DOPG). The head of DOPG is negatively charged ($q = -1 e_0$) and at room temperature it has an average surface area of 0.77 nm^2 [18]. This

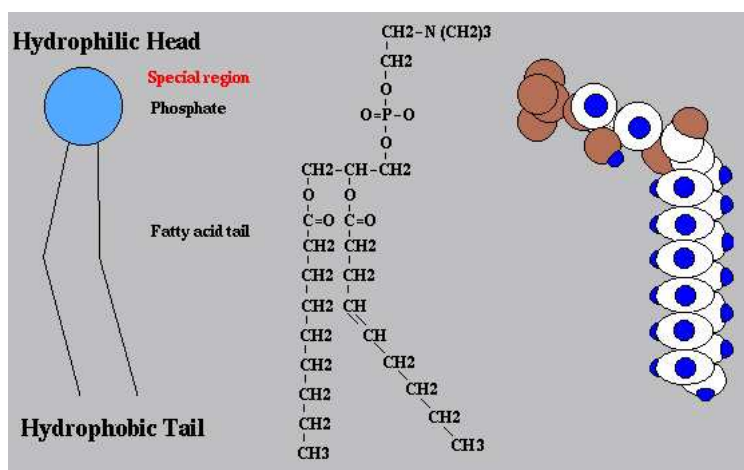


Figure 1.11: Chemical and geometric structure of phospholipids. This picture is taken from the Web Cell Biology Course at the University of Minnesota at <http://www.cbc.umn.edu/>.

yields a surface charge density of $\sigma = -1.3 e_0/\text{nm}^2$. The value can then be used for evaluating the electrostatic potential of the membrane as described in subsection 2.2.2.

1.6 Binding of cyt *c* to membranes

The ultimate test for both theories and computer simulations is always the experiment.

In their work Heimburg *et al.* focussed on the binding of cyt *c* to mixed lipid membranes composed of the negatively charged dioleoyl phosphatidylglycerol (DOPG) and of the neutral dioleoyl phosphatidylcholine (DOPC) [1]. So-called binding isotherms were measured for the association of horse heart cyt *c* with the aforementioned bilayer membranes. These curves represent the amount of bound cyt *c* depending on the total concentration in the test tube. Since the simulation box in this work also contains cyt *c* as well as a membrane surface, these measurements are ideal for comparison with simulation results. Both for testing the model and for tuning the free parameters necessary for the computer experiments, these measurements serve as a reference. Figure 1.12 shows the measured cyt *c* binding isotherms at ionic strength $c_{Na^+} = 90$ mM.

Membrane association and detachment of cyt *c* in the millisecond to second time domain was also investigated using stopped-flow fluorescence spectroscopy [19]. It was found that the speed of cyt *c* dissociation is very sensitive to the amount of acidic phospholipid in the

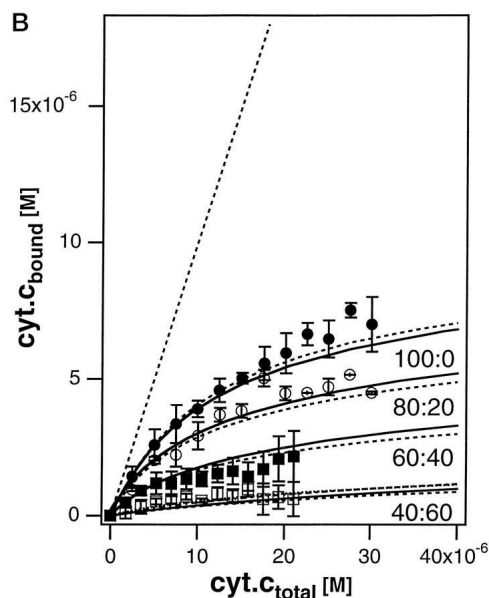


Figure 1.12: Measured cytochrome *c*-binding isotherms for various mixed lipid membranes [1]. Results for ionic strength $[\text{Na}^+] = 90$ mM and four different DOPG:DOPC (mol/mol) compositions are shown. The solid and dashed lines are theoretical curves developed in ref. [1].

membrane. Unfortunately, the large dissociation times in the millisecond range can still not be simulated properly because this time scale is not accessible even by Brownian dynamics.

Another problem is the variation of the diffusion coefficient when considering lateral diffusion. In ref. [20] lateral diffusion coefficients for cyt *c* in membranes of giant mitoplasts using the technique of fluorescence redistribution after photobleaching (FRAP) were measured. Very small values of $3.5 - 7 \times 10^{-14}$ m²/s depending on the assay medium were determined. This is more than four orders of magnitude smaller than the free diffusion coefficient utilised for our simulations.

1.7 Molecular simulation techniques

The following two sections outline two successful computer simulation techniques. From that survey it will become clear why Brownian dynamics is the method of choice for handling the aforementioned model system.

1.7.1 Molecular dynamics

Experimental values of physical quantities of a many-particle system can be determined by ensemble averaging over all the accessible states of that system. However, most experimental systems are so large that it is impossible to find the ensemble average by summing over all states in a computer. The idea to solve this problem is to find a method which is able to calculate physical quantities from statistical averages over a restricted set of states. Two such techniques are molecular dynamics (MD) and Monte Carlo (MC) [21]. Basically, one generates a conformational ensemble consisting of a big number of correlated system configurations which are determined successively from each other.

MD is preferentially used for studying classical many-particle systems. Since essentially the equations of motion are solved numerically, MD represents the system as it evolves in time. Besides evaluating statical physical quantities MD is also useful for studying dynamical phenomena far from equilibrium.

Now consider a system consisting of N classical particles interacting with each other located in a rectangular box of volume $V = L_1 \times L_2 \times L_3$. Their positions are denoted $\vec{r}_1, \vec{r}_2, \dots, \vec{r}_N$. In many cases the total force \vec{F}_i on one of the particles i can be written as a sum over pair forces $F(|\vec{r}_i - \vec{r}_j|)$. The magnitude of those only depends on the relative distance between the particles:

$$\vec{F}_i(\vec{r}_1, \vec{r}_2, \dots, \vec{r}_N) = \sum_{j=1, j \neq i}^N F(|\vec{r}_i - \vec{r}_j|) \frac{\vec{r}_{ij}}{|\vec{r}_i - \vec{r}_j|}. \quad (1.3)$$

In practical situations there are also always external forces present. In the situations described above such a force would be the force exerted by the membrane on the cyt c molecules, e.g. However, for simplicity, in this subsection it is assumed that there are no external forces. The equations of motion can then be written as

$$\frac{d^2 \vec{r}_i(t)}{dt^2} = \frac{\vec{F}_i(\vec{r}_1, \vec{r}_2, \dots, \vec{r}_N)}{m_i}, \quad (1.4)$$

which is Newton's second law. The approximate character of MD becomes clear if one considers the following points. First of all, the systems are treated classically though in principle they are of course quantum mechanically by nature. Secondly, the forces are not known exactly. They are usually given in parametrised forms which are derived from *ab initio* calculations or by fitting simulation results to experimental data. The third point is

the finiteness of a system or in other words the small systems size in simulations compared to experimental systems. The presence of a boundary has to be considered because it leads to side effects. The usual procedure is the use of periodic boundary conditions (PBC): one assumes that for these boundary conditions the system behaviour is very similar to one that is embedded in an infinite system. In periodic boundary conditions the central simulation box (the “system”) is surrounded by exact copies of that box including the complete particle configurations. This includes entering and leaving the box of particles that pass over one of the six box boundaries. Figure 1.13 illustrates the use of these boundary conditions. Since every particle has an infinite number of interaction partners one can write the total force between two particles i and j as

$$\vec{F}_{PBC}(\vec{r}_i - \vec{r}_j) = \sum_{n_1, n_2, n_3 = -\infty}^{\infty} \vec{F} \left(\left| \vec{r}_i - \vec{r}_j + \sum_{\mu=1}^3 \vec{L}_{\mu} n_{\mu} \right| \right). \quad (1.5)$$

\vec{L}_{μ} are vectors along the box edges as indicated in figure 1.13 and n_{μ} are integer coefficients. In practice the sum needs only to be calculated until it converges. One possibility is the use of the so-called minimum image convention, where only the nearest image neighbours of each particle are considered in the force calculation. The fourth remark concerning the approximate character of MD simulations is about the finite accuracy of the numerical integration algorithm. The computed trajectories will therefore always deviate from the ones a system would follow in reality. A standard MD simulation for studying equilibrium systems consists of three steps:

- Initialisation
- starting the simulation and waiting for equilibration
- continuing simulation and storing results

Details can be found in many textbooks on MD, e.g., in ref. [22]. To get an idea just one possible integration algorithm is mentioned here: a special form of the so-called Verlet algorithm, namely the leap-frog algorithm. The positions \vec{r} after one time step h are iteratively evaluated from the positions at the beginning of the time step. The idea is now to evaluate the velocities \vec{v} at time steps in between those at which the positions are evaluated:

$$\vec{v}(t + h/2) = \vec{v}(t - h/2) + h\vec{F}[\vec{r}(t)]/m \quad (1.6)$$

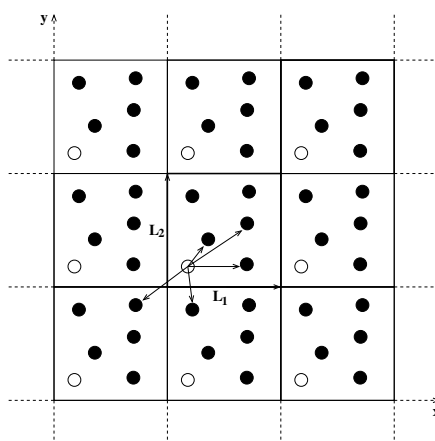


Figure 1.13: 2-dimensional periodic boundary conditions in computer simulations (3 dimensions is straightforward). Every particle inside the central box interacts with every particle in the periodically repeated surrounding box copies. The interactions of the white particle with its next neighbours only are indicated by arrows.

and

$$\vec{r}(t+h) = \vec{r}(t) + h\vec{v}(t+h/2). \quad (1.7)$$

A survey of the origin and early uses of biomolecular simulations is given in ref. [23]. Examples for systems that can be studied by MD simulations are the following:

- Protein stability [24]
- Protein folding and conformational changes [25]
- Molecular recognition: proteins, DNA, membranes, complexes [26]
- Ion transport in biological systems [27]

MD is also used as a tool for drug design [28] and structure determination [29]. Typical time scales that can be reached by MD are a few picoseconds up to ~ 100 ns for systems with thousands up to one hundred thousands of atoms [23] in simulation boxes of about $(1..10 \text{ nm})^3$.

1.7.2 Brownian dynamics

The discussion above indicates that systems like the ones that are supposed to be studied here with dimensions of more than 1000 nm^3 and tens to hundreds (even simplified) molecules cannot be handled by MD if one is really interested in large time scales.

The method of choice is the Brownian dynamics (BD) technique as already partly discussed in section 1.1. If one is interested only in processes with time scales larger than the solvent relaxation time of about 10^{-14} s an important approximation can be made: instead of filling the simulation box with explicit solvent (mostly water) molecules which largely contributes to the number of atoms that have to be kept track of during a simulation, an implicit solvent approach is possible. In fact, this is the basic idea of BD. Thus, BD is a statistical method which reduces the computational costs immensely.

A comprehensive review on theoretical simulations of protein-protein interactions can be found in [30]. Especially protein association kinetics can be studied using the BD method. It has been applied, e.g., to the association and the electron transfer between horse ferricytochrome *c* and bovine ferrocytochrome *b₅* in [17]. An important BD package is UHBD (University of Houston Brownian Dynamics Program) which can be used to compute pK(a)s of ionisable groups in proteins [31]. Protein association studies of two proteins have also been made using the SDA (Simulation of Diffusional Association of Proteins) package by Gabdouliline (see, e.g., refs. [32], [33]). Common to all these studies is the small number of molecules (mostly two). These can be modelled atomistically and only simulation times of several μs are reached.

In this work, however, the motion of several (tens to hundreds) particles needs to be examined. Therefore, besides using BD instead of atomistic MD, a second approximation has to be made concerning the model of the participating molecules. To summarise, one can say that for the purposes here a coarse-grained BD is necessary. Figure 1.14 shows the simulation box as it is used in this work. It contains the Brownian particles and the membrane surface at the bottom. The model is explained in detail in the method sections.

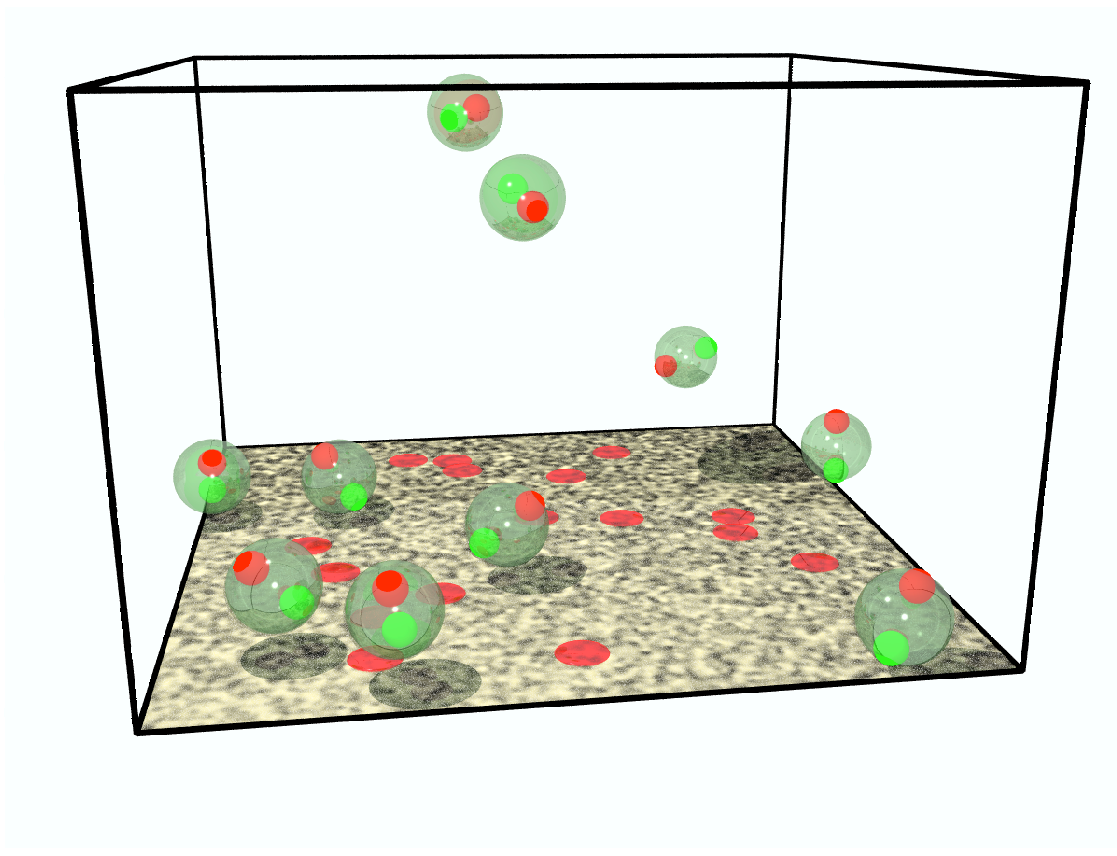


Figure 1.14: The simulation box and a snapshot of a simulation output of the program CESIP (cf. Chapter 3). The spherical particles represent the simplified cyt *c* molecules that are diffusing above the charged membrane surface at the bottom. Cyt *c*'s dipole charges are shown in red (negative) and green (positive). The filled circles in red represent additional simplified membrane proteins with negative net charge. The box dimension is $30 \times 30 \times 20 \text{ nm}^3$.

Chapter 2

Brownian dynamics methods

This chapter is partly based on a paper published by Gorba and Helms [34] where the basic techniques going along with simple test simulations are described. Additionally, section 2.3.3 is taken from a publication by Geyer, Gorba and Helms [35] where a new particle insertion algorithm is explained. As discussed in the previous sections, the systems under study in this work contain many, i.e., typically two up to about 200 particles. They can therefore be considered as multi-protein systems. The method of choice for such systems is Brownian dynamics. In this chapter the equations of motion, the interactions and the simulation system with its boundary conditions are presented.

2.1 Brownian dynamics (BD)

2.1.1 Introduction

As explained in the introductory section 1.1 Brownian motion is powered by random forces due to collisions with solvent molecules. These random collision forces \vec{f}_{ran} fluctuate on the so called solvent time scale of about 10^{-14} s and as a consequence a Brownian particle attains an equilibrium velocity $\vec{v} = \vec{p}/m$, with m the mass of the Brownian particle and \vec{p} its momentum. This equilibrium motion leads to systematic collisions with the solvent and therefore to a friction force \vec{f}_{fri} . For not too large velocities (small *Reynolds number*, cf. subsection 2.2.1, eq. (2.17)) it is proportional to \vec{v} :

$$\vec{f}_{fri} = -\gamma\vec{p}/m. \quad (2.1)$$

This is *Stoke's* friction law. γ is the friction coefficient which is proportional to the radius a of a macroscopically large sphere:

$$\gamma = 6\pi\eta a, \quad (2.2)$$

where η is the solvent's viscosity. Using the two force contributions Newton's equation of motion for a free Brownian particle can be written as [4]

$$d\vec{p}/dt = \vec{f}_{ran} + \vec{f}_{fri} = \vec{f}_{ran}(t) - \gamma\vec{p}/m. \quad (2.3)$$

The (ensemble) average of the random forces \vec{f}_{ran} vanishes and, since in BD one is only interested in a description of times large with respect to the solvent time scale, one can assume that there is no correlation between random forces \vec{f}_{ran} at different times t and t' . Mathematically, this is described by a delta correlation. Hence, the two statistical properties of the fluctuating forces \vec{f}_{ran} are

$$\langle \vec{f}_{ran}(t) \rangle = 0 \quad (2.4)$$

and¹

$$\langle \vec{f}_{ran}(t) \vec{f}_{ran}(t') \rangle = \mathbf{G}\delta(t - t'), \quad (2.5)$$

where \mathbf{G} is a 3×3 matrix representing the strength of the fluctuating force. According to the *fluctuation-dissipation theorem* \mathbf{G} is given by

$$\mathbf{G} = 2\gamma k_B T \mathbf{I}, \quad (2.6)$$

where k_B is Boltzmann's constant, T the temperature and \mathbf{I} the 3×3 unit matrix. The deterministic eq. (2.3) together with the statistical eqs. (2.4) and (2.5) is called a Langevin equation. The Langevin equation is only valid for time scales much larger than the solvent time scale. More precisely, for $t \gg m/\gamma$ one finds $\langle \vec{p}(t) \vec{p}(t) \rangle = const$ and $\langle |\vec{r}(t) - \vec{r}(0)|^2 \rangle \propto t$. This is the so-called Diffusive, Smoluchowski or Brownian time scale (BTS). To summarise, on the BTS the mean squared displacement of the Brownian particles increases linearly with time and their momenta are relaxed to equilibrium with the solvent. Thus, one can drop momentum coordinates in such a description which reduces computational costs significantly. In the following the full Langevin equation for a many particle system and its solution is explained.

¹Note that the following product of vectors is a dyadic product resulting in a matrix. For two vectors \vec{a} and \vec{b} it is defined as $(\vec{a}\vec{b})_{ij} := a_i b_j$. A scalar product or a product of a matrix and a vector will be denoted by a dot explicitly.

2.1.2 Equations of motion and their solution

The equations of Brownian motion of N particles can be written as $6N$ Langevin equations, $3N$ each for translation and for rotation [36]:

$$m_i \frac{d\vec{v}_i}{dt} = - \sum_{j=1}^N [\Gamma_{ij}^{\mathbf{T}} \cdot \vec{v}_j + \Gamma_{ij}^{\mathbf{TR}} \cdot \vec{\omega}_j] + \vec{F}_i + \sum_{j=1}^{6N} f_j \vec{\alpha}_{ij} \quad (2.7)$$

and

$$I_i \frac{d\vec{\omega}_i}{dt} = - \sum_{j=1}^N [\Gamma_{ij}^{\mathbf{RT}} \cdot \vec{v}_j + \Gamma_{ij}^{\mathbf{R}} \cdot \vec{\omega}_j] + \vec{T}_i + \sum_{j=1}^{6N} f_j \vec{\alpha}_{(i+N)j}, \quad (2.8)$$

with $1 \leq i \leq N$. $\vec{v}_i = \frac{d\vec{r}_i}{dt}$ is the velocity vector of particle i with position \vec{r}_i and $\vec{\omega}_i = \frac{d\vec{\varphi}_i}{dt}$ is the angular velocity of particle i with rotation angle vector $\vec{\varphi}_i$. The mass of particle i is denoted by m_i and I_i is its momentum of inertia. $\Gamma_{ij}^{\mathbf{T}}$ is a 3×3 matrix describing the translational hydrodynamic interaction between particles i and j . It is therefore called the translational friction matrix. Analogously, $\Gamma_{ij}^{\mathbf{R}}$ is the rotational and $\Gamma_{ij}^{\mathbf{TR}(\mathbf{RT})}$ the coupling translational-rotational (rotational-translational) friction matrix. These four matrices can be interpreted as sub-matrices of a $6N \times 6N$ grand friction matrix²:

$$\Gamma = \begin{pmatrix} \Gamma^{\mathbf{T}} & \Gamma^{\mathbf{TR}} \\ \Gamma^{\mathbf{RT}} & \Gamma^{\mathbf{R}} \end{pmatrix}. \quad (2.9)$$

\vec{F}_i is the external force vector and \vec{T}_i the torque on particle i . The terms $f_j \vec{\alpha}_{ij}$ describe forces and torques due to random collisions of fluid molecules with the particles. The $6N$ numbers f_j are Gaussian variables with mean value $\langle f_j \rangle = 0$ and covariance $\langle f_i(0) f_j(t) \rangle = 2\delta_{ij} \delta(t)$. Finally, the column vectors $\vec{\alpha}_{ij} = (\alpha_{(3i-2)j}, \alpha_{(3i-1)j}, \alpha_{(3i)j})^T$ are composed of the $6N \times 6N$ elements of a matrix α connected to the elements of the grand friction matrix by $\Gamma_{ij} = \beta \sum_{l=1}^{6N} \alpha_{il} \cdot \alpha_{jl}$, with $\beta = 1/k_B T$.

Starting from the translational Langevin equation, Ermak and McCammon derived an iteration algorithm for the spatial coordinates of the particles which is valid for time steps $\Delta t \gg \beta m D_0$ [37]. D_0 is the free diffusion coefficient of a single sphere with radius a . It is defined as the inverse of the friction coefficient from eq. (2.2) multiplied by $k_B T$:

$$D_0 = k_B T / \gamma = k_B T / 6\pi\eta a. \quad (2.10)$$

²For a detailed description and the connection between friction and diffusion matrices, see subsection 2.2.1.

The time interval $\Delta t \gg \beta m D_0$ characterises the Brownian regime which is much larger than the momentum relaxation time (BTS, see previous subsection). Thus, the algorithm gives the position displacements after each time step Δt :

$$\vec{r}_i = \vec{r}_i^0 + \Delta t \sum_{j=1}^N \mathbf{D}_{ij}^{\mathbf{T},0} \cdot \overleftarrow{\nabla}_{\vec{r}_j} + \beta \Delta t \sum_{j=1}^N \mathbf{D}_{ij}^{\mathbf{T},0} \cdot \vec{F}_j + \vec{R}_i(\mathbf{D}^{\mathbf{T},0}, \Delta t). \quad (2.11)$$

The superscript 0 indicates variables to be evaluated at the beginning of each time step. $\mathbf{D}_{ij}^{\mathbf{T}}$ is the 3×3 translational diffusion matrix² for the hydrodynamic interaction between particles i and j . $\overleftarrow{\nabla}_{\vec{r}_j}$ is the column vector of derivatives acting on the variable to the left with respect to the space coordinates of particle j : $\overleftarrow{\nabla}_{\vec{r}_j} = \left(\overleftarrow{\partial} / \partial x_j, \overleftarrow{\partial} / \partial y_j, \overleftarrow{\partial} / \partial z_j \right)^T$. $\vec{R}_i(\mathbf{D}^{\mathbf{T},0}, \Delta t)$ is the 3-component random displacement vector for particle i according to the last term in the translational Langevin equation. It depends on the full translational diffusion matrix $\mathbf{D}^{\mathbf{T}}$ evaluated at each time step and on the time step Δt . Its ensemble average value is $\langle \vec{R}_i \rangle = 0$ and its variance-covariance is $\langle \vec{R}_i \vec{R}_j \rangle = 2 \mathbf{D}_{ij}^{\mathbf{T},0} \Delta t$. Based on this approach a generalised algorithm also taking into account the coupling between translational and rotational movement was developed in ref. [36]:

$$\begin{aligned} \vec{r}_i = & \vec{r}_i^0 + \Delta t \sum_{j=1}^N \mathbf{D}_{ij}^{\mathbf{T},0} \cdot \overleftarrow{\nabla}_{\vec{r}_j} + \Delta t \sum_{j=1}^N \mathbf{D}_{ij}^{\mathbf{TR},0} \cdot \overleftarrow{\nabla}_{\vec{\varphi}_j} \\ & + \beta \Delta t \sum_{j=1}^N \mathbf{D}_{ij}^{\mathbf{T},0} \cdot \vec{F}_j + \beta \Delta t \sum_{j=1}^N \mathbf{D}_{ij}^{\mathbf{TR},0} \cdot \vec{T}_j + \vec{R}_i(\mathbf{D}^0, \Delta t) \end{aligned} \quad (2.12)$$

and

$$\begin{aligned} \vec{\varphi}_i = & \vec{\varphi}_i^0 + \Delta t \sum_{j=1}^N \mathbf{D}_{ij}^{\mathbf{RT},0} \cdot \overleftarrow{\nabla}_{\vec{r}_j} + \Delta t \sum_{j=1}^N \mathbf{D}_{ij}^{\mathbf{R},0} \cdot \overleftarrow{\nabla}_{\vec{\varphi}_j} \\ & + \beta \Delta t \sum_{j=1}^N \mathbf{D}_{ij}^{\mathbf{RT},0} \cdot \vec{F}_j + \beta \Delta t \sum_{j=1}^N \mathbf{D}_{ij}^{\mathbf{R},0} \cdot \vec{T}_j + \vec{R}_{i+N}(\mathbf{D}^0, \Delta t). \end{aligned} \quad (2.13)$$

Analogous to the space derivatives $\overleftarrow{\nabla}_{\vec{r}_j}$, $\overleftarrow{\nabla}_{\vec{\varphi}_j}$ denotes the column vector of derivatives with respect to the angular coordinates³: $\overleftarrow{\nabla}_{\vec{\varphi}_j} = \left(\overleftarrow{\partial} / \partial \varphi_{x,j}, \overleftarrow{\partial} / \partial \varphi_{y,j}, \overleftarrow{\partial} / \partial \varphi_{z,j} \right)^T$. These two

³The arrow to the left is necessary because of the matrix notation. The product in the sums of eqs. (2.11), (2.12) and (2.13) requires the order matrix, column vector, if a column vector shall be the result.

equations can be written in the following compact form by using the generalised $6N$ dimensional vectors

$$\vec{y} = (\vec{r}_1, \dots, \vec{r}_N, \vec{\varphi}_1, \dots, \vec{\varphi}_N)^T \quad (2.14)$$

and

$$\vec{F} = \left(\vec{F}_1, \dots, \vec{F}_N, \vec{T}_1, \dots, \vec{T}_N \right)^T, \quad (2.15)$$

yielding

$$\vec{y} = \vec{y}^0 + \Delta t \mathbf{D}^0 \cdot \overleftarrow{\nabla} + \beta \Delta t \mathbf{D}^0 \cdot \vec{F}^0 + \vec{R}(\mathbf{D}^0, \Delta t). \quad (2.16)$$

\mathbf{D} is the $6N \times 6N$ grand diffusion matrix consisting of the 4 sub-matrices \mathbf{D}^T , \mathbf{D}^{TR} , \mathbf{D}^{RT} and \mathbf{D}^R from eqs. 2.12 and 2.13 (for details, see subsection 2.2.1).

$\overleftarrow{\nabla} = \left(\overleftarrow{\nabla}_{\vec{r}_1}, \dots, \overleftarrow{\nabla}_{\vec{r}_N}, \overleftarrow{\nabla}_{\vec{\varphi}_1}, \dots, \overleftarrow{\nabla}_{\vec{\varphi}_N} \right)^T$ is the $6N$ -dimensional gradient vector. The $6N$ -dimensional random displacements have mean values $\langle \vec{R} \rangle = 0$ and variance-covariance $\langle \vec{R} \vec{R} \rangle = 2\mathbf{D}^0 \Delta t$.

2.2 Interactions

There are basically three different kinds of interactions that have to be modelled in order to simulate a biological system. There are direct interactions between molecules, namely electrostatics and van der Waals interactions. Furthermore, since in such systems there is always a solvent present, also indirect interactions mediated by the fluid occur. We start by describing these indirect interactions, the so-called hydrodynamic interactions.

2.2.1 Hydrodynamic interaction

A moving particle in a fluid induces a fluid flow in the solvent. The fluid flow propagates through the solvent and encounters other particles. The motion of these is then subsequently affected by the incoming waves. This is the origin of the so-called hydrodynamic interactions [4]. Provided that the particles are macroscopic bodies, these interactions can be described on the basis of the Navier-Stokes equation.

A general scheme to evaluate diffusion tensors of an arbitrary number of spheres, immersed in a viscous fluid, is presented in [38]. Here, only the basic ideas are summarised. Consider N spherical particles of masses m_i and radii a_i immersed in an incompressible

fluid. The particle centres are located at $\vec{r}_i(t)$ at time t . The motion of an incompressible fluid (infinite propagation velocity of sound waves) obeys the Navier-Stokes equation. This equation can be written in a form so that the so-called Reynolds number occurs:

$$Re := \frac{\rho a_i v}{\eta}. \quad (2.17)$$

ρ denotes the fluid's constant mass density and η is its viscosity. A typical fluid flow velocity is the velocity v of the immersed particles. For small Reynolds numbers and on the BTS the Navier-Stokes equation can be linearised. The result is the so-called Creeping⁴ Flow equations:

$$\left. \begin{aligned} \nabla \cdot \mathbf{P}(\vec{r}, t) &= 0, \\ \nabla \cdot \vec{v}(\vec{r}, t) &= 0 \end{aligned} \right\} \text{for all } |\vec{r} - \vec{r}_i(t)| > a_i, \quad (2.18)$$

with

$$P_{\alpha\beta} = p\delta_{\alpha\beta} - \eta \left(\frac{\partial v_\beta}{\partial r_\alpha} + \frac{\partial v_\alpha}{\partial r_\beta} \right), \quad (2.19)$$

being the elements of the pressure tensor \mathbf{P} . \vec{v} is the fluid's velocity field, p the hydrostatic pressure and η its viscosity. Here, greek indices run from 1 to 3 and the sphere labels i run from 1 to N . Assuming no external forces on the particles (only hydrodynamics in this subsection) the equations of motion for particle i with velocity $\vec{u}_i(t)$ and angular velocity $\vec{\omega}_i(t)$ can be written as

$$m_i \frac{d\vec{u}_i(t)}{dt} = - \int_{S_i(t)} \mathbf{P}(\vec{r}, t) \cdot \hat{n}_i dS =: \vec{K}_i(t), \quad (2.20)$$

$$I_i \frac{d\vec{\omega}_i(t)}{dt} = - \int_{S_i(t)} [\vec{r} - \vec{r}_i(t)] \times \mathbf{P}(\vec{r}, t) \cdot \hat{n}_i dS =: \vec{T}_i(t). \quad (2.21)$$

\vec{K}_i and \vec{T}_i are the force and torque exerted on particle i , respectively, defined by the integrals over the particle's surface $S_i(t)$ at time t . \hat{n}_i is a unit vector perpendicular to this surface pointing outwards. Assuming a homogeneous mass distribution within sphere i , its moment of inertia is $I_i = 2m_i a_i^2/5$. As boundary conditions for the set of equations above so-called stick conditions are assumed here, meaning that the fluid velocity is equal to the particle velocity on the particle's surface: the fluid sticks to the spheres so that

$$\vec{v}(\vec{r}, t) = \vec{u}_i(t) + \vec{\omega}_i(t) \times [\vec{r} - \vec{r}_i(t)] \quad \text{for } |\vec{r} - \vec{r}_i(t)| = a_i. \quad (2.22)$$

⁴“Creeping” refers to the fact that the Reynolds numbers are small when the typical fluid flow velocity is small [4].

In the so-called method of induced forces the eqs. (2.18) are extended to the inside of the spheres:

$$\left. \begin{aligned} \nabla \cdot \mathbf{P}(\vec{r}, t) &= \sum_{j=1}^N \vec{F}_j(\vec{r}, t), \\ \nabla \cdot \vec{v}(\vec{r}, t) &= 0 \end{aligned} \right\} \text{for all } \vec{r}, \quad (2.23)$$

with $\vec{F}_j(\vec{r}, t) = 0$ outside sphere j , i.e., for $|\vec{r} - \vec{r}_j(t)| > a_j$. The conditions for the extension of the fluid field inside the spheres are

$$\vec{v}(\vec{r}, t) = \vec{u}_i(t) + \vec{\omega}_i(t) \times [\vec{r} - \vec{r}_i(t)] \quad \text{for } |\vec{r} - \vec{r}_i(t)| \leq a_i \quad (2.24)$$

and

$$p(\vec{r}, t) = 0 \quad \text{for } |\vec{r} - \vec{r}_i(t)| < a_i. \quad (2.25)$$

Due to discontinuities of the pressure tensor (zero inside the spheres, non-zero outside) the induced force density must have the form of a delta-function:

$$\vec{F}_i(\vec{r}, t) = a_i^{-2} f_i(\hat{n}_i, t) \delta(|\vec{r} - \vec{r}_i(t)| - a_i). \quad (2.26)$$

Using the pressure tensor from eqs. (2.23) the force $\vec{K}_i(t)$ and the torque $\vec{T}_i(t)$ exerted on sphere i by the fluid can be expressed in terms of the induced force density:

$$\vec{K}_i(t) = - \int_{S_i(t)} \mathbf{P}(\vec{r}, t) \cdot \hat{n}_i dS = - \int_{|\vec{r} - \vec{r}_i(t)| \leq a_i} \nabla \cdot \mathbf{P}(\vec{r}, t) d^3r = - \int \vec{F}_i(\vec{r}, t) d^3r, \quad (2.27)$$

$$\vec{T}_i(t) = - \int_{S_i(t)} [\vec{r} - \vec{r}_i(t)] \times \mathbf{P}(\vec{r}, t) \cdot \hat{n}_i dS = - \int [\vec{r} - \vec{r}_i(t)] \times \vec{F}_i(\vec{r}, t) d^3r. \quad (2.28)$$

By introducing the Fourier transforms of the velocity $\vec{v}(\vec{k}) = \int \vec{v}(\vec{r}) e^{-i\vec{k} \cdot \vec{r}} d^3r$, of the pressure $p(\vec{k}) = \int p(\vec{r}) e^{-i\vec{k} \cdot \vec{r}} d^3r$ and of the induced force density

$\vec{F}_i(\vec{k}) = \int \vec{F}_i(\vec{r}) e^{-i\vec{k} \cdot (\vec{r} - \vec{r}_i)} d^3r$, the fluid eqs. (2.23), together with the pressure tensor in eq. (2.19) become in wavevector representation

$$\eta k^2 \vec{v}(\vec{k}) = -i\vec{k} p(\vec{k}) + \sum_{j=1}^N e^{-i\vec{k} \cdot \vec{r}_j} \vec{F}_j(\vec{k}), \quad (2.29)$$

with

$$\vec{k} \cdot \vec{v}(\vec{k}) = 0. \quad (2.30)$$

By applying the operator $\mathbf{1} - \vec{k}\vec{k}/k^2$ to both sides of eq. (2.29) one obtains together with eq. (2.30)

$$\eta k^2 \vec{v}(\vec{k}) = \sum_{j=1}^N e^{-i\vec{k}\cdot\vec{r}_j} \left(\mathbf{1} - \vec{k}\vec{k}/k^2 \right) \cdot \vec{F}_j(\vec{k}). \quad (2.31)$$

The formal solution for that equation is

$$\vec{v}(\vec{k}) = \vec{v}^0(\vec{k}) + \sum_{j=1}^N \eta^{-1} k^{-2} e^{-i\vec{k}\cdot\vec{r}_j} \left(\mathbf{1} - \vec{k}\vec{k}/k^2 \right) \cdot \vec{F}_j(\vec{k}), \quad (2.32)$$

where $\vec{v}^0(\vec{k})$ is the unperturbed fluid velocity field and the solution of eq. (2.29). In the linear regime the relation between forces and velocities on the one hand and torques and angular velocities on the other hand can be written as a set of coupled linear equations of the form

$$\vec{u}_i = - \sum_j \mu_{ij}^{\mathbf{TT}} \cdot \vec{K}_j - \sum_j \mu_{ij}^{\mathbf{TR}} \cdot \vec{T}_j, \quad (2.33)$$

$$\vec{\omega}_i = - \sum_j \mu_{ij}^{\mathbf{RT}} \cdot \vec{K}_j - \sum_j \mu_{ij}^{\mathbf{RR}} \cdot \vec{T}_j. \quad (2.34)$$

Eq. (2.32) is the starting point for the calculation of the forces and torques that act on the N spheres in the fluid. After having obtained these forces and torques, one can then construct the mobility tensors μ by comparison with the set of eqs. (2.33) and (2.34). The actual calculation of the forces and torques, leading to expressions for the mobility tensors, is not presented here because it is very difficult and lengthy. Several slightly different definitions of the mobility tensor exist⁵. Sometimes it is called mobility tensor μ , in some publications it is the diffusion tensor \mathbf{D} . Also friction matrices $\mathbf{\Gamma}$ are used very often. The connection between these is simply $\mathbf{D} = \beta^{-1} \mu = \beta^{-1} \mathbf{\Gamma}^{-1}$. Here, we only use diffusion matrices \mathbf{D} as in ref. [4]. The grand diffusion matrix \mathbf{D} contains 4 sub-matrices $\mathbf{D}^{\mathbf{T}}$ (translation-translation coupling), $\mathbf{D}^{\mathbf{TR}}$ (translation-rotation coupling), $\mathbf{D}^{\mathbf{RT}}$ (rotation-translation coupling), $\mathbf{D}^{\mathbf{R}}$ (rotation-rotation coupling), and each of these is a $3N \times 3N$ matrix containing $N^2 \ 3 \times 3$ “sub-sub-matrices”. Thus, \mathbf{D} itself is a $6N \times 6N$ matrix:

$$\mathbf{D} = \begin{pmatrix} \mathbf{D}^{\mathbf{T}} & \mathbf{D}^{\mathbf{TR}} \\ \mathbf{D}^{\mathbf{RT}} & \mathbf{D}^{\mathbf{R}} \end{pmatrix}. \quad (2.35)$$

⁵Since tensors can be represented by matrices, both of these two terms are used in this work.

To clarify the convention used here, e.g., $\mathbf{D}^{\mathbf{R}}$ without any indices denotes the $3N \times 3N$ rotational diffusion matrix, so that $\mathbf{D}_{ij}^{\mathbf{R}}$ with $(i, j) \in [1, N]$ is its (i, j) -th 3×3 sub-matrix which determines the hydrodynamic (rotational) coupling between particles i and j . Eqs. (2.32), (2.33) and (2.34) describe the general hydrodynamic interaction of N particles immersed in a fluid in the creeping flow approximation. But there exists no general solution to these equations and one therefore needs to solve eq. (2.32) iteratively by calculating the correction to \vec{v}^0 from \vec{v}^0 itself using this solution to start the next iteration. For small particle densities, or correspondingly interparticle distances much larger than their radii, the first order already captures the main features of the hydrodynamic interaction. Two such approximations are known from literature: the very simple Oseen- and the Rotne-Prager approximation which takes the iteration one step further [4]. The corresponding entries of the mobility or diffusion tensors according to eqs. (2.33) and (2.34) have the following forms:

Translation $\mathbf{D}^{\mathbf{T}}$ (Rotne-Prager tensor approximation) :

$$\mathbf{D}_{ij}^{\mathbf{T}} = \begin{cases} D_0 \mathbf{I} & \text{for } i = j, \\ D_0 \left[\frac{3}{4} \frac{a}{r_{ij}} (\mathbf{I} + \hat{r}_{ij} \hat{r}_{ij}) + \frac{1}{2} \left(\frac{a}{r_{ij}} \right)^3 (\mathbf{I} - 3\hat{r}_{ij} \hat{r}_{ij}) \right] & \text{for } i \neq j. \end{cases} \quad (2.36)$$

Rotation $\mathbf{D}^{\mathbf{R}}$:

$$\mathbf{D}_{ij}^{\mathbf{R}} = \begin{cases} D_0 \frac{3}{4a^2} \mathbf{I} & \text{for } i = j, \\ D_0 \frac{3a}{8r_{ij}^3} [3\hat{r}_{ij} \hat{r}_{ij} - \mathbf{I}] & \text{for } i \neq j. \end{cases} \quad (2.37)$$

Translation-Rotation $\mathbf{D}^{\mathbf{TR}}$ and $\mathbf{D}^{\mathbf{RT}}$:

$$\mathbf{D}_{ij}^{\mathbf{TR}} = \mathbf{D}_{ij}^{\mathbf{RT}} \begin{cases} \mathbf{0} & \text{for } i = j, \\ -D_0 \frac{3a}{4r_{ij}^2} \varepsilon \cdot \hat{r}_{ij} & \text{for } i \neq j. \end{cases} \quad (2.38)$$

Here, $r_{ij} = |\vec{r}_{ij}|$ is the distance between particles i and j and $\hat{r}_{ij} = \vec{r}_{ij} / |\vec{r}_{ij}|$ is their unit separation vector. The product $\hat{r}_{ij} \hat{r}_{ij}$ is the dyadic product explained in footnote 1. ε is the total antisymmetric 3rd rank tensor defined by $\varepsilon_{lmn} := \vec{e}_l \cdot (\vec{e}_m \times \vec{e}_n)$, where \vec{e}_l is the unit vector in direction of axis l (here, $(l, m, n) \in [1, 3]$). The product of ε and \hat{r}_{ij} is defined as a matrix with elements $(k, l) \in [1, 3]$: $(\varepsilon \cdot \hat{r}_{ij})_{kl} := \sum_{m=1}^3 \varepsilon_{klm} (\hat{r}_{ij})_m$. $D_0 = k_B T / 6\pi\eta a$ is the free diffusion coefficient of a single sphere with radius a . A consequence of

the leading term $1/r_{ij}$ in eq. (2.36) is that hydrodynamics is a long-range interaction. As can be seen from eq. (2.36), in the Rotne-Prager approximation interactions due to interparticle distances up to to order r^{-3} are taken into account. Only pair-interactions are considered. The computational cost using this approximate approach is still maintainable but anything beyond this description, e.g., considering three body interactions would be too costly. In the wide field of polymer physics hydrodynamics is very often simulated on a grid using the lattice Boltzmann method (see, e.g., ref. [39]). This method is not utilised here and the correct way to include this interaction into simulations on large systems like ours is still being investigated. Nevertheless, some results using the approximate method described above are presented and discussed in Chapter 4.

Two kinds of external forces on the proteins are applied in the simulations: a protein experiences the sum of electrostatic and van der Waals forces both from the other molecules in the simulation box and from the charged membrane. These interactions are discussed in the following subsections.

2.2.2 Electrostatic interaction

Interaction between two cyt *c* molecules: dipolar sphere model

The electrostatic interaction between the diffusing proteins is approximated by the dipolar sphere model (DSM) [30]: a horse heart cyt *c* model molecule is represented as a sphere of radius $R = 1.66$ nm containing a monopole charge $q \simeq +7 e_0$ in the centre and two charges of $q = \pm 1.7 e_0$ forming a dipole. The dipole charges are embedded $b_i = 0.15$ nm into the sphere from the surface. The choice of these two charges at these positions inside the sphere is made in order to reproduce the appropriate dipole moment calculated from the molecule's coordinate set [16]. The interaction potential between two such spheres with these three charges each is then given by the following screened Coulomb/Debye potential:

$$W_{12} = \frac{1}{4\pi\epsilon\epsilon_0} \sum_{i=1}^3 \sum_{j=1}^3 q_i q_j \frac{e^{-\kappa(r_{ij}-B_{ij})}}{(1 + \kappa B_{ij}) r_{ij}}, \quad (2.39)$$

where r_{ij} is the distance between charge i of protein 1 and charge j of protein 2. ϵ_0 and ϵ are the dielectric constants for vacuum and the solvent, respectively. $B_{ij} = b_i + b_j$ is an empirical distance shifting factor taking into account the finite ion size of the surrounding fluid [17]. The exponential screening of the interactions between the charges due to counter

ions is not modelled explicitly but it is described by the Debye length $l_D = 1/\kappa$. κ is defined in the following subsection.

Poisson-Boltzmann equation

Electrostatic interactions between diffusing particles and the charged membrane surface also need to be considered. To derive the potential ϕ of a flat charged surface with charge density σ one has to start from Poisson's equation [40]:

$$\Delta\phi = -\frac{1}{\varepsilon_0\varepsilon}\rho. \quad (2.40)$$

A solvent usually contains positive and negative salt ions which, according to the boundary conditions, form the space charge density ρ . Boltzmann's theorem states that the average ion concentration at a certain point in space can be calculated from the electrostatic potential at that point:

$$n_{\pm} = n \exp(\mp v_{\pm} e_0 \beta \phi), \quad (2.41)$$

where n is the number of ions per volume element in the region where $\phi = 0$. v_+ and v_- are the valencies of the positive and negative ions, respectively. In a symmetrical electrolyte ($v_+ = v_- = v$) the space charge density is thus

$$\rho = v e_0 (n_+ - n_-) = -2n v e_0 \sinh(v e_0 \beta \phi). \quad (2.42)$$

Inserting this into Poisson's eq. (2.40) one yields the so-called Poisson-Boltzmann equation:

$$\Delta\phi = -\frac{2n v e_0}{\varepsilon_0\varepsilon} \sinh(v e_0 \beta \phi). \quad (2.43)$$

This equation governs all electrostatic effects in a solvent and therefore has to be solved if one needs the space dependent electrostatic potential.

Interaction between cyt c and a charged planar surface

In the case of a flat membrane surface as studied here, eq. (2.43) can be transformed into a simpler form [40]. For symmetry reasons the potential only depends on the normal coordinate z with respect to the planar surface at $z = 0$. By introducing the substitutions

$$y := v e_0 \beta \phi, \quad (2.44)$$

$$\begin{aligned} y_0 &:= ve_0\beta\phi_0, \\ \kappa^2 &:= \frac{2ne_0^2v^2\beta}{\varepsilon_0\varepsilon}, \\ \xi &:= \kappa z, \end{aligned}$$

the Poisson-Boltzmann equation takes on the following simple form:

$$\frac{d^2y}{d\xi^2} = \sinh y. \quad (2.45)$$

Using the boundary conditions $y = 0$ and $dy/d\xi = 0$ for $\xi = \infty$ and $y = y_0$ for $\xi = 0$ (fixed surface potential $\phi(z=0) = \phi_0$), one finds after integrating twice:

$$e^{y/2} = \frac{e^{z/2} + 1 + (e^{z/2} - 1)e^{-\xi}}{e^{z/2} + 1 - (e^{z/2} - 1)e^{-\xi}}. \quad (2.46)$$

After solving this equation for y , using $c := ve_0\beta/2$ and reinserting the substitutions (2.44), one finally gets the electrostatic potential ϕ of the model surface with charge density σ surrounded by a fluid with dielectric constant ε and Debye length $l_D=1/\kappa$ at a vertical distance z from the plane:

$$\phi(z) = \frac{1}{c} \ln \left[\frac{e^{c\phi_0} + 1 + (e^{c\phi_0} - 1)e^{-\kappa z}}{e^{c\phi_0} + 1 - (e^{c\phi_0} - 1)e^{-\kappa z}} \right] = \frac{2}{c} \operatorname{artanh} \left(\tanh \left(\frac{c}{2} \phi_0 \right) e^{-\kappa z} \right). \quad (2.47)$$

The relation between the surface charge density σ and the surface potential ϕ_0 is determined by Poisson's eq. (2.40): integration of the space charge density along the normal coordinate, i.e., $\sigma = -\int_0^\infty \rho dz = \varepsilon_0\varepsilon \int_0^\infty \frac{d^2\phi}{dz^2} dz = -\varepsilon_0\varepsilon \left(\frac{d\phi}{dz} \right)_{z=0}$ finally yields

$$\phi_0 = \frac{1}{c} \ln \left(\frac{c\sigma}{\varepsilon_0\varepsilon\kappa} + \sqrt{\left(\frac{c\sigma}{\varepsilon_0\varepsilon\kappa} \right)^2 + 1} \right). \quad (2.48)$$

It should be noted that the Poisson-Boltzmann equation can be linearised for small surface potentials $y_0 \ll 1$. In this case the potential function takes on a simple exponential form. This special solution is the so-called Gouy-Chapman law:

$$\phi = \phi_0 e^{-\kappa z}. \quad (2.49)$$

2.2.3 Van der Waals interaction

Interaction between two cyt *c* molecules

For achieving a realistic behaviour in situations in which particles come very close to each other or when they get into the vicinity of the membrane surface, attractive and repulsive van der Waals potentials are included. The mathematical expressions are derived in this subsection. After a couple of test simulations the well-depth of both particle-particle and particle-surface interactions was set to $E_{min,vdW} = -1 k_B T$ which equals the thermal energy of the fluid that drives the free Brownian motion⁶. For numerical reasons the repulsive potentials are linearised (constant forces) at short distances. By doing so, one avoids very high repulsive forces when the particles are about to penetrate the membrane surface or each other. To speed up the calculations it is possible to only consider interactions between particles closer than an adjustable cutoff distance.

Hamaker [41] derived formulas for the interaction energy between two spherical particles with radii R_1 , R_2 and constant atom densities ρ_1 , ρ_2 and also for the interaction of a sphere with a planar surface. He assumed an attractive interaction potential proportional to r^{-6} between each pair of atoms in the particles. In this work Hamaker's integration method was also used to find formulas for a short-ranged repulsive potential proportional to r^{-12} . Generally, for potentials r^{-n} the energy is

$$E = - \int_{V_1} \int_{V_2} C r^{-n} dV_1 dV_2, \quad (2.50)$$

where C is a constant depending essentially on the particle atom densities, V_i is the volume of sphere i and r is the distance between dV_1 and dV_2 . For particles at a separation distance $d = R - R_1 - R_2$ Hamaker obtained

$$E_{sp-sp}^{n=6}(x) = -A^2 \frac{1}{12} \left[\frac{y}{x^2 + xy + x} + \frac{y}{x^2 + xy + x + y} + 2 \ln \left(\frac{x^2 + xy + x}{x^2 + xy + x + y} \right) \right], \quad (2.51)$$

using the definitions $x := \frac{d}{2R_1}$ and $y := \frac{R_2}{R_1}$ (see Figure 2.1). A is an empirical parameter which determines the strength of the attractive forces between two spheres. In the same

⁶In some simulations slightly different values were used. See detailed listing of parameters in Tables A.1, A.2, A.3, A.4, A.5 and A.6.

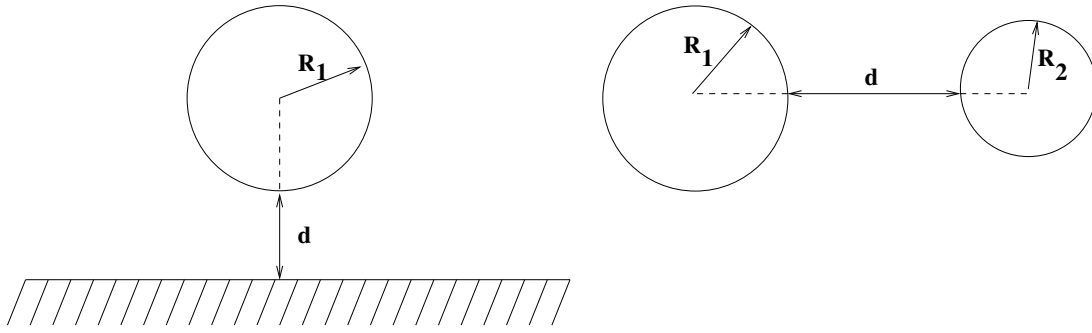


Figure 2.1: Definition of contact distance d between a sphere and a planar surface and two spheres.

way, for the purposes in this work an analogous equation for the repulsive r^{-12} interatomic potential was derived:

$$\begin{aligned}
 E_{sp-sp}^{n=12}(x) = & \frac{B^2}{1260R_1^6} \frac{1}{1+y+2x} \times & (2.52) \\
 & \left[\frac{1}{160} \left(\frac{1}{(1+y+x)^5} - \frac{1}{(1+x)^5} - \frac{1}{(y+x)^5} + \frac{1}{x^5} \right) \right. \\
 & - \frac{1}{384} (-5+y+2x) \left(\frac{1}{(1+y+x)^6} - \frac{1}{(1+x)^6} \right) \\
 & + \frac{1}{384} (7+y+2x) \left(\frac{1}{(y+x)^6} - \frac{1}{x^6} \right) \\
 & + \frac{1}{128} (2+y+2x) \left(-\frac{1}{(1+y+x)^7} + \frac{1}{(1+x)^7} \right) \\
 & \left. - \frac{1}{128} (y+2x) \left(\frac{1}{(y+x)^7} - \frac{1}{x^7} \right) \right].
 \end{aligned}$$

The empirical parameter B determines the strength of the repulsive forces between two spheres.

Interaction between cyt c and a planar surface

The interaction between a sphere (sp) and a planar surface (pl) immediately follows from eqs. (2.51) and (2.52) by making sphere 2 infinitely large ($y \rightarrow \infty$), because a sphere with infinite radius is equivalent to an infinite non-curved surface. The attractive energy function

becomes

$$E_{sp-pl}^{n=6}(x) = -A\tilde{A}\frac{1}{12} \left[\frac{1}{x} + \frac{1}{x+1} + 2 \ln \left(\frac{x}{x+1} \right) \right]. \quad (2.53)$$

The corresponding equation for the repulsive energy (r^{-12} interatomic potential) is given by

$$E_{sp-pl}^{n=12} = \frac{B\tilde{B}}{161280R_1^6} \left[\frac{1}{3(1+x)^6} - \frac{1}{3x^6} + \frac{1}{(1+x)^7} + \frac{1}{x^7} \right]. \quad (2.54)$$

\tilde{A} and \tilde{B} are empirical parameters which determine the strength of the attractive and repulsive forces between a sphere and a plane.

Similar formulas were derived by Bicout and Field (although not given in their paper) and were fitted for convenience by cubic splines [42]. Figure 2.2 shows the energy curves for the van der Waals interactions in comparison with a simple Lennard-Jones 12-6 pair potential which can be written as

$$E^{LJ}(x) = 4E_0^{LJ} \left[\left(\frac{\sigma}{x} \right)^{12} - \left(\frac{\sigma}{x} \right)^6 \right], \quad (2.55)$$

where E_0^{LJ} denotes the well-depth and σ characterises the steeply rising repulsive wall at distances less than $x \sim \sigma$ [2]. The derived potentials are slightly less steep and have a longer range than the Lennard-Jones potential.

Note that the derivation of the preceding equations only considers interatomic forces. However, since the strength of the interactions is given by adjustable parameters, we assume that interactions like hydrophobic interactions can be included into these expressions via A , B , \tilde{A} and \tilde{B} . Thus, the term van der Waals is used in a more general way throughout this work than is usually done.

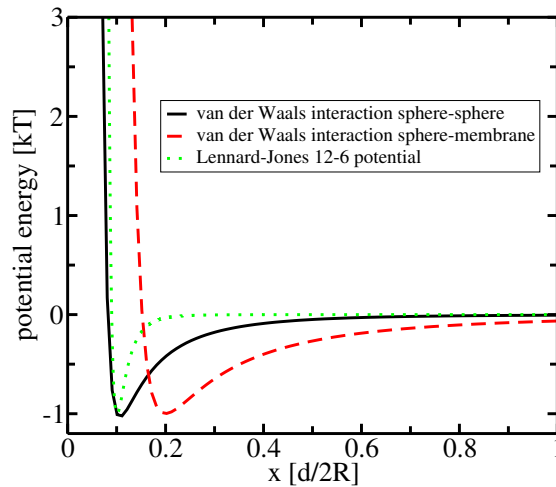


Figure 2.2: Distance dependence of the van der Waals interaction between two spheres (solid line) and between a sphere and the surface (dashed line). The dotted line illustrates the run of a simple Lennard-Jones 12-6 pair potential for the same energy minimum.

2.3 Simulation system and boundary conditions

The simulation system with its different boundary conditions is sketched in Figures 2.3, 2.4 and 2.5. In any case the actual simulation box is rectangular with the origin at the lower left corner and the membrane surface located at $z = 0$. In all simulations except the ones in Chapter 6 it is $x_0 = y_0$.

Besides the integration algorithm one also needs to specify the boundary conditions for actually solving the equations of motion. Three different boundary conditions can be applied using the Brownian dynamics package CESIP. Firstly, the system can be finite assuming that all walls except the membrane are reflecting. Secondly, the system can be infinitely large by applying 2-dimensional periodic boundary conditions on the side walls and reflecting boundary conditions on the upper wall. Thirdly, the upper wall at $z = z_0$ can be assumed to be an interface to a continuous bulk region using a particle insertion algorithm. In this case the side walls are reflecting ones. The boundary conditions are described in detail in the following subsections 2.3.1, 2.3.2 and 2.3.3. The simulation parameters are summarised in Tables A.1, A.2, A.3, A.4, A.5 and A.6. The parameters for the moving particles are taken from ref. [17] and mimic horse heart cyt *c* molecules. A Debye length of 1 nm corresponds to an ionic strength of 90 mM [1]. The membrane surface charge density of $\sigma = -1.3 e_0/\text{nm}^2$

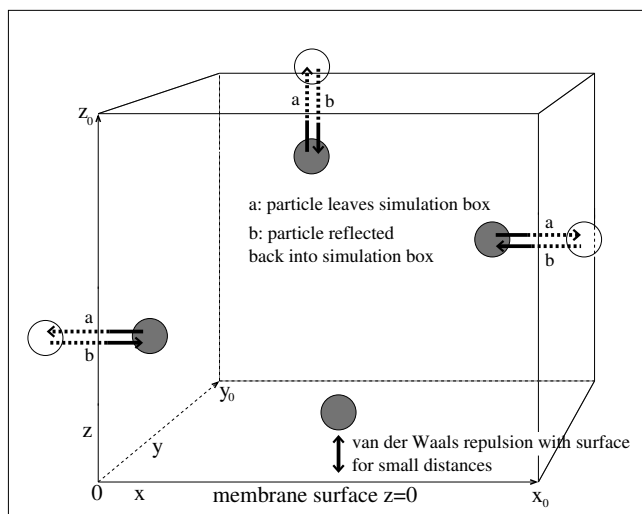


Figure 2.3: Sketch of the simulation box with reflecting boundary conditions. The particles, denoted by the grey spheres, are simulated explicitly between $z = 0$ and $z = z_0$ and simply reflected from the walls except from the membrane at $z = 0$.

corresponds to a lipid layer composed to 100 % of negatively charged DOPG lipids with a surface per lipid headgroup of $A \simeq 0.77 \text{ nm}^2$ [18].

2.3.1 Reflecting boundary conditions

The simplest boundary conditions are reflecting boundaries as illustrated in Figure 2.3. The box walls at $x = 0$, $x = x_0$, $y = 0$, $y = y_0$ and $z = z_0$ serve as reflecting borders. In practice, the particles are simply mirrored back into the box when they try to penetrate the walls. It is also possible to reflect the particles from the walls using small random displacements. As to the membrane at $z = 0$, the van der Waals repulsion described in the previous section prevents particles from leaving the box through the membrane surface at $z = 0$. Thus, no particles can leave the simulation box and their number remains constant: $N = \text{const}$. These boundary conditions were applied in simulations from our initial work [34]. For the simulations presented in this thesis, however, they were not utilised because one has to use very large boxes in order not to have too strong side effects. As a consequence very long simulation times are necessary so that the particles are able to sample the whole space available properly.

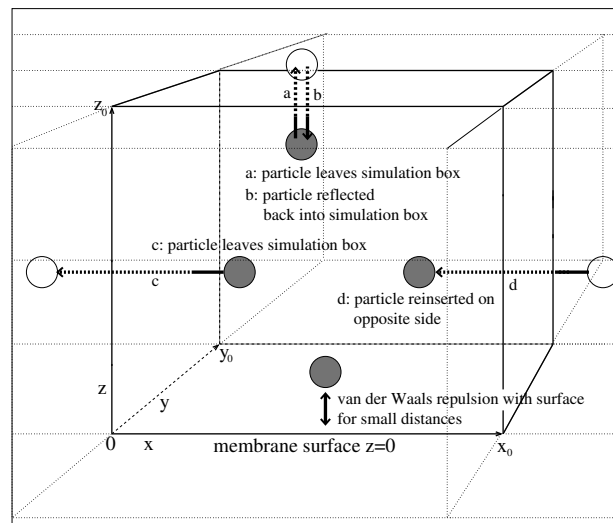


Figure 2.4: Sketch of the simulation box with 2-dimensional periodic boundary conditions. The dotted lines indicate the box copies in x - and y -directions. The particles, denoted by the grey spheres, are simulated explicitly between $z = 0$ and $z = z_0$ and are reinserted on the opposite side if they are about to leave the box through one of the side walls. The upper wall at $z = z_0$ is again a reflecting border like in Figure 2.3.

2.3.2 2-dimensional periodic boundary conditions in xy -direction.

One of the major characteristics in the simulations presented is the membrane surface at $z = 0$. Thus, periodic boundary conditions in all directions would imply periodically repeated membranes in z -direction. Therefore, a different approach is chosen. The wall at $z = z_0$ is again reflecting like in subsection 2.3.1 but the system is assumed to be infinitely large in xy -direction. The system consists of exact periodic copies in two dimensions as indicated by the dotted lines in Figure 2.4. Particles are simulated explicitly only in the central box (the actual simulation box). Particles trying to penetrate one of the side walls are simply reinserted on the opposite side (see also Figure 1.13 in section 1.7). With these boundary conditions the minimum image convention can be used. Particle-particle interactions are only considered for distances smaller than half the box width (here it is $x_0 = y_0$). As a consequence an interaction cutoff with maximum radius $r_{cutoff,max} = x_0/2$ must be applied. Since as many particles leave the simulation box as are reinserted, the number of particles remains constant: $N = const$. Simulations using these boundary conditions are presented in Chapter 4.

2.3.3 Dynamic particle insertion algorithm

Due to the fixed finite height of the simulation box no independent bulk concentration can be established in simulations using boundary conditions like in 2.3.1 and 2.3.2. This problem is alleviated by using constant density boundary conditions that are explained in detail in [35]. As shown in Figure 2.5 a continuous bulk region, indicated by grey zigzag lines, begins at $z = z_0$. In that region it is assumed that the molecules can diffuse freely and only particles between the membrane at $z = 0$ and the interface at $z = z_0$ are simulated explicitly. The side walls in this case are reflecting borders like in subsection 2.3.1. As a result, the amount of particle in the simulation box varies: $N \neq const.$ In the following a short derivation of the insertion algorithm is presented. Briefly, one starts with a system composed of a region close to the membrane surface, where particle-membrane interactions are important and an infinite non-interaction region, where these interactions are negligible. In this bulk region we have a constant density of particles that behave like non-interacting Brownian particles. The conditional probability for a Brownian particle with position \vec{r}' at time $t = 0$ to move to a new position \vec{r} in the time interval τ is given by a Gaussian distribution [4]:

$$P(\vec{r}, \tau | \vec{r}', 0) = \frac{1}{\pi^{\frac{3}{2}} a_0^3} \exp\left[-\frac{(r - r')^2}{a_0^2}\right], \quad (2.56)$$

where $a_0 = \sqrt{4D_0\tau}$ is a typical step size of the Brownian motion with the free diffusion coefficient D_0 (cf. subsection 2.1.2). From $P(\vec{r}, \tau | \vec{r}', 0)$ the particle flux through the surface $z = z_0$ is easily calculated: the probability of finding a particle at a position \vec{r} with $z < z_0$ after one time step τ is given by

$$\rho(z, \tau) = \int_{z' > z_0} P(\vec{r}, \tau | \vec{r}', 0) \rho(\vec{r}') d^3r'. \quad (2.57)$$

After integration one finds that this is proportional to the complementary error function $\text{erfc}(z) = \frac{2}{\sqrt{\pi}} \int_z^\infty e^{-\xi^2} d\xi$:

$$\rho(z, \tau) = \frac{\rho_0}{2} \text{erfc}\left(\frac{z_0 - z}{a_0}\right). \quad (2.58)$$

According to this formula, a Monte Carlo algorithm was added to the program package CESIP. This algorithm decides if a particle is added to the simulation next to $z \leq z_0$ or not. Particles crossing the interface at z_0 in opposite direction (away from the membrane) are simply removed from the simulation box. The program CESIP is described in the next

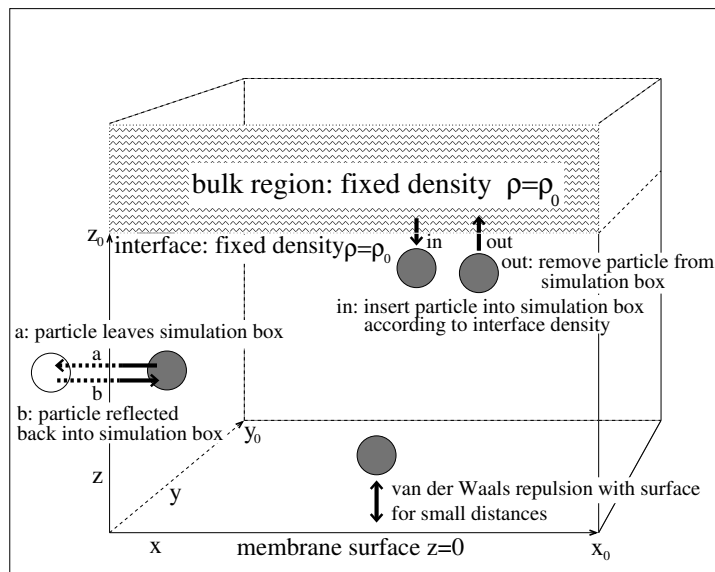


Figure 2.5: Sketch of the simulation box. The particles, denoted by the grey spheres, are simulated explicitly between $z = 0$ and $z = z_0$. The bulk is indicated by the grey zigzag lines. With the particle insertion algorithm only reflecting side walls are available in CESIP.

chapter. Simulations using particle insertion/deletion together with reflecting side walls are presented in Chapters 5 and 6.

Chapter 3

Implementation

3.1 Structure of CESIP

The Brownian dynamics package CESIP (Cellular Simulation Package) was developed and used for the simulations presented in Chapters 4, 5 and 6. It is written in C++ and consists of about 7000 lines of code. It can be compiled using the GNU compiler g++ (version 2.96) using a makefile coming along with the package. An object-oriented approach was chosen in order to alleviate maintenance and upgradeability. For object-oriented programming (OOP) the so-called Unified Modelling Language (UML) is available - a collection of graphical symbols and rules for connecting these symbols in order to describe the source code [43,44]. In OOP modules are called classes which represent basic entities of a model on which a program is based. E.g., in this work such a basic entity is a Protein. This indicates that one such basic class would be a Protein class. Figure 3.1 illustrates the classes assumed for the present implementation of our Brownian dynamics package. There are seven classes which together build up the simulation systems. The most important class is `Protein` which contains a protein's attributes like its position, its charges etc. Such class attributes are always shown below the class name. Below the attributes one finds possible operations or methods available for that class. Since a protein has a force field (which can contain various interactions) a method `forceField()` is necessary. The program distinguishes between "static" proteins (like membrane proteins) and such that can move. Thus, a class `MovingProtein` is derived from the parent class `Protein`. `MovingProtein` is a child class and contains all of `Protein`'s features plus the ability to move in space. The membrane is represented by

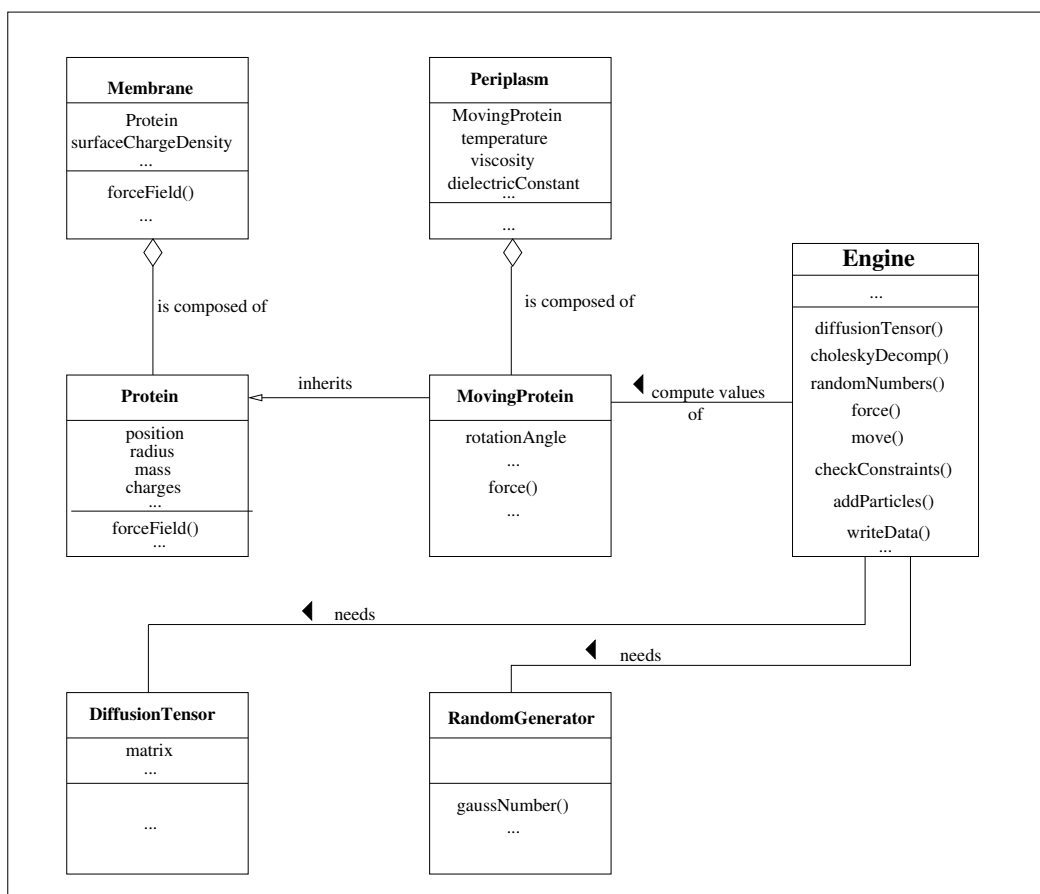


Figure 3.1: UML representation of the classes used in the Brownian dynamics package CESIP.

Membrane. As one would expect a membrane has attributes like a surface charge density and can contain membrane proteins. As a consequence `Membrane` can contain instances of the `Protein` class. Furthermore, due to the surface charges, e.g., it also creates a force field which acts on molecules present. The `Periplasm` class models the environment in which the molecules are embedded and thus contains instances of `MovingProtein`. Additionally, it has attributes like temperature, viscosity and electric permeability. The main class of the package is `Engine`. This class contains all the methods for computing the trajectories of the moving proteins according to eq. (2.16) and it uses the helper classes `DiffusionTensor` and `RandomGenerator` which can determine the diffusion tensor and the random numbers for the Brownian motion. The methods shown in `Engine` represent the sequence of calculations as they occur in the program's main loop. I.e., at first the diffusion tensor is calculated by the method `diffusionTensor()` from the N particle positions. The resulting matrix is then decomposed (both only in case hydrodynamics is included) in `choleskyDecomp()` in order to subsequently compute the Gaussian random numbers in `randomNumbers()` [45]. After that the interparticle and external forces are evaluated in method `force()`. All these ingredients are then used by `move()` to move the Brownian particles to their new positions. The new positions need to be consistent with the boundary conditions which are controlled in `checkConstraints()`. If, e.g., a Brownian particle reaches the box walls it will be handled either according to reflecting or periodic boundary conditions. In the case of simulations using the interfacing algorithm `checkConstraints()` also serves as particle annihilator, i.e., a Brownian particle is removed from the simulation box if it reaches the upper box wall at $z = z_0$. The creation of particles according to eq. (2.58) is handled in method `addParticles()`. Finally, when all the new positions fulfilling the boundary conditions are determined, the coordinates for that time step are written into the output file by the method `writeData()`. Figure 3.2 illustrates the aforementioned by means of a flow chart.

3.2 Computational performance

The CPU time needed for the computation of the particle trajectories mostly depends on the number N of particles in the simulation box. Particle-particle interactions involve $\frac{N(N-1)}{2}$ calculations per time step for electrostatic and van der Waals forces and torques each. The interaction of the Brownian particles with the membrane only scales linearly: N calculations

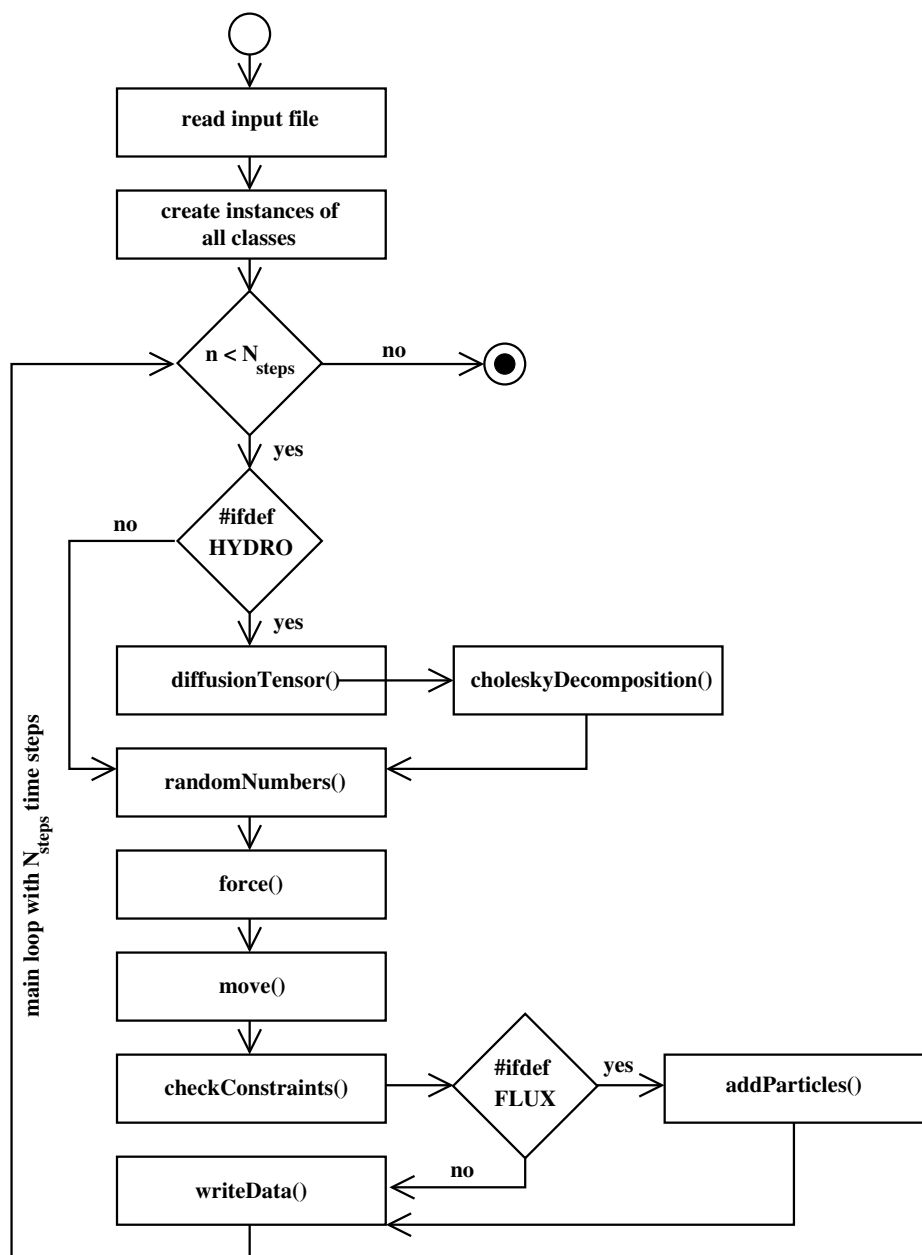


Figure 3.2: Flow chart of the Brownian dynamics program CESIP. The condition `#ifdef HYDRO` is a preprocessor directive. That means, that this condition is checked by the compiler only while creating the executable but not during runtime. The functions `diffusionTensor()` and `choleskyDecomposition()` are only invoked if the executable was created for the use with hydrodynamic interaction. Analogously, particles can only be added (particle flux enabled) if the executable was created with the `FLUX` directive set. In that case `checkConstraints()` also serves as particle annihilator and contains additional code for removing particles if they reach the upper box wall.

are necessary for both the electrostatic and van der Waals forces and torques. The calculation of the random displacements is straightforward in the case that no hydrodynamics is considered: $6N$ uniform random numbers using one of the “ran” functions described in ref. [45] are computed and then transformed into Gaussian numbers using the Box-Muller method [45]. However, if hydrodynamic interaction is considered it becomes more expensive. Besides the computational cost for the evaluation of the diffusion matrix which scales quadratically like the particle-particle interactions mentioned above, hydrodynamics also influences the cost for the calculation of the random displacements. Actually, the Gaussian random numbers are now taken from a different ensemble. As described in ref. [45], it is necessary to decompose the diffusion matrix (Cholesky decomposition) at each time step. The Gaussian random numbers are then weighted with the decomposed matrix. The Cholesky decomposition is very expensive. It involves $(6N)^3/6$ operations per time step. The cubic scaling of this decomposition makes standard hydrodynamics a very unpleasant feature for large particle numbers.

In the following Tables 3.1 and 3.2 the amount of time needed by the different main functions is listed for a couple of test simulations (simulation time T_{sim}) in a $30 \times 30 \times 30$ nm³ box. These simulations were performed on single nodes of a Dell Linux Cluster with 1 GB memory and two Intel XEON 2.8 GHz processors each. A profile was created using the program gprof. The differences between the total measured CPU time $T_{real,cpu}$ and the time measured by gprof T_{gprof} are due to the fact that gprof does not take into account the time needed for the execution of system libraries. The times measured for the different functions are therefore calculated with respect to T_{gprof} . As shown in Table 3.1 the average time per time step $T_{av/step}$ is of course largest for the 50 particle simulation including hydrodynamics. Without hydrodynamics the calculation of the electrostatic and van der Waals forces almost consumes the whole time measured, whereas with hydrodynamics included the random number computation and thus the Cholesky decomposition become expensive as well. Table 3.2 illustrates how CPU time scales with the number of particles in the box. As already mentioned, the Cholesky decomposition involves about N^3 computational steps and thus the difference factor between a 22 and 50 particle simulation using hydrodynamics should be $(50/22)^3 \simeq 11.74$. In this case the measured values agree very well with the theoretical value. For the computation of the diffusion tensor and the forces the scaling is a bit worse than the theoretical quadratic scaling $(50(50 - 1)/(22(22 - 1))) \simeq 5.3$ which is probably due to the larger amount of memory needed.

number of particles	22 (no HI)	50 (no HI)	22 (HI)	50 (HI)
T_{sim} (μ s)	1.0	1.0	0.5	0.5
$T_{real,cpu}$ (s)	1899.79	8453.06	1237.07	6301.16
$T_{av/step}$ (s)	0.019	0.085	0.025	0.126
T_{gprof} (s)	364.40	1931.11	261.76	1888.45
T_i [% of T_{gprof}] for $i =$				
1: diffusionTensor()	–	–	11.2	11.3
2: randomNumbers()	0.9	0.4	18.6	28.3
[3: choleskyDecomposition()]	–	–	16.5	26.7
4: force()	96.3	98.4	64.9	57.3
5: move()	2.5	1.1	5.1	3.0
6: checkConstraints()	0.1	0.1	0.1	0.0
7: writeData()	0.0	0.0	0.0	0.0

Table 3.1: Performance test: comparison between times needed for simulations with and without hydrodynamics and for two different particle numbers (boundary conditions as in subsection 2.3.2: reflecting and 2-dimensional periodic boundary conditions). Data were written after 50 time steps each.

	50p/22p no HI		50p/22p HI	
$i =$	sim. $T_{50p,i}/T_{22p,i}$	theo. $T_{50p,i}/T_{22p,i}$	sim. $T_{50p,i}/T_{22p,i}$	theo. $T_{50p,i}/T_{22p,i}$
1: diffusionTensor()	—	—	7.28	5.30
2: randomNumbers()	2.36	2.27	—	—
[3: choleskyDecomposition()]	—	—	11.67	11.74
4: force()	5.41	5.30	6.37	5.30

Table 3.2: Comparison between the measured and theoretical scaling of times needed for the most important main functions for the simulations from Table 3.1. Without hydrodynamics the agreement is very good. E.g., the expected linear scaling for the calculation of random numbers agrees almost exactly with the measurement.

Chapter 4

Simulations and results for $N=\text{const.}$

In this chapter results from simulations with a constant number N of particles are presented. In x - and y -directions 2-dimensional periodic boundary conditions were applied, whereas the wall at $z = z_0$ was assumed to be a reflecting boundary (see subsection 2.3.2).

4.1 A simple test of the source code

To test the code, especially with respect to the implementation of hydrodynamic interactions, a simple test simulation from ref. [36] was repeated. Two spheres with radius a were positioned with their centre at coordinates $(-a, 0, 0)$ (particle 1) and $(a, 0, 0)$ (particle 2), i.e., with their surfaces touching each other. Using this initial configuration, 10^6 Brownian displacements, i.e., 10^6 single-step simulations were made. From the displacements $\Delta y = y_i - y_i^0$ (see eq. (2.16)) normalised correlation factors C_{ij} of the form

$$C_{ij} = \frac{\langle \Delta y_i \Delta y_j \rangle}{\sqrt{\langle \Delta y_i^2 \rangle \langle \Delta y_j^2 \rangle}}, \text{ with } 1 \leq (i, j) \leq 12, \quad (4.1)$$

were calculated. For the translational diffusion matrix only the Oseen approximation (first term of the Rotne-Prager tensor in eq. (2.36)) was used here. The grand diffusion tensor for

a 2-particle system is a 12×12 matrix:

$$\mathbf{D} = \begin{pmatrix} \mathbf{D}_{11}^{\mathbf{T}} & \mathbf{D}_{12}^{\mathbf{T}} & \mathbf{D}_{11}^{\mathbf{TR}} & \mathbf{D}_{12}^{\mathbf{TR}} \\ \mathbf{D}_{21}^{\mathbf{T}} & \mathbf{D}_{22}^{\mathbf{T}} & \mathbf{D}_{21}^{\mathbf{TR}} & \mathbf{D}_{22}^{\mathbf{TR}} \\ \mathbf{D}_{11}^{\mathbf{RT}} & \mathbf{D}_{12}^{\mathbf{RT}} & \mathbf{D}_{11}^{\mathbf{R}} & \mathbf{D}_{12}^{\mathbf{R}} \\ \mathbf{D}_{21}^{\mathbf{RT}} & \mathbf{D}_{22}^{\mathbf{RT}} & \mathbf{D}_{21}^{\mathbf{R}} & \mathbf{D}_{22}^{\mathbf{R}} \end{pmatrix}, \quad (4.2)$$

with the following sub-matrices:

$$\mathbf{D}_{11}^{\mathbf{T}} = \mathbf{D}_{22}^{\mathbf{T}} = \begin{pmatrix} D_0 & 0 & 0 \\ 0 & D_0 & 0 \\ 0 & 0 & D_0 \end{pmatrix}, \quad (4.3)$$

$$\mathbf{D}_{12}^{\mathbf{T}} = \mathbf{D}_{21}^{\mathbf{T}} = \begin{pmatrix} \frac{3D_0a}{4r_{12}^3} (r_{12}^2 + x_{12}^2) & \frac{3D_0a}{4r_{12}^3} x_{12}^2 y_{12}^2 & \frac{3D_0a}{4r_{12}^3} x_{12}^2 z_{12}^2 \\ \frac{3D_0a}{4r_{12}^3} y_{12}^2 x_{12}^2 & \frac{3D_0a}{4r_{12}^3} (r_{12}^2 + y_{12}^2) & \frac{3D_0a}{4r_{12}^3} y_{12}^2 z_{12}^2 \\ \frac{3D_0a}{4r_{12}^3} z_{12}^2 x_{12}^2 & \frac{3D_0a}{4r_{12}^3} z_{12}^2 y_{12}^2 & \frac{3D_0a}{4r_{12}^3} (r_{12}^2 + z_{12}^2) \end{pmatrix}, \quad (4.4)$$

$$\mathbf{D}_{11}^{\mathbf{TR}} = \mathbf{D}_{22}^{\mathbf{TR}} = \mathbf{D}_{11}^{\mathbf{RT}} = \mathbf{D}_{22}^{\mathbf{RT}} = \begin{pmatrix} 0 & 0 & 0 \\ 0 & 0 & 0 \\ 0 & 0 & 0 \end{pmatrix}, \quad (4.5)$$

$$\mathbf{D}_{12}^{\mathbf{TR}} = -\mathbf{D}_{21}^{\mathbf{TR}} = \mathbf{D}_{12}^{\mathbf{RT}} = -\mathbf{D}_{21}^{\mathbf{RT}} = \begin{pmatrix} 0 & -\frac{3D_0a}{4r_{12}^3} z_{12} & \frac{3D_0a}{4r_{12}^3} y_{12} \\ \frac{3D_0a}{4r_{12}^3} z_{12} & 0 & -\frac{3D_0a}{4r_{12}^3} x_{12} \\ -\frac{3D_0a}{4r_{12}^3} y_{12} & \frac{3D_0a}{4r_{12}^3} x_{12} & 0 \end{pmatrix}, \quad (4.6)$$

$$\mathbf{D}_{11}^{\mathbf{R}} = \mathbf{D}_{22}^{\mathbf{R}} = \begin{pmatrix} \frac{3D_0}{4a^2} & 0 & 0 \\ 0 & \frac{3D_0}{4a^2} & 0 \\ 0 & 0 & \frac{3D_0}{4a^2} \end{pmatrix} \text{ and} \quad (4.7)$$

$$\mathbf{D}_{12}^{\mathbf{R}} = \mathbf{D}_{21}^{\mathbf{R}} = \begin{pmatrix} \frac{3D_0a}{8r_{12}^5} (3x_{12}^2 - r_{12}^2) & \frac{9D_0a}{8r_{12}^5} x_{12}^2 y_{12}^2 & \frac{9D_0a}{8r_{12}^5} x_{12}^2 z_{12}^2 \\ \frac{9D_0a}{8r_{12}^5} y_{12}^2 x_{12}^2 & \frac{3D_0a}{8r_{12}^5} (3y_{12}^2 - r_{12}^2) & \frac{9D_0a}{8r_{12}^5} y_{12}^2 z_{12}^2 \\ \frac{9D_0a}{8r_{12}^5} z_{12}^2 x_{12}^2 & \frac{9D_0a}{8r_{12}^5} z_{12}^2 y_{12}^2 & \frac{3D_0a}{8r_{12}^5} (3z_{12}^2 - r_{12}^2) \end{pmatrix}. \quad (4.8)$$

In the test case of close-touching spheres $r_{ij} = 2a$. The grand diffusion matrix is positive definite and symmetric. In this special case this can be verified easily by looking at the grand diffusion matrix after putting all the sub-matrices into eq. (4.2). Using the iteration algorithm

(a)	Δx	Δy	Δz	$\Delta\varphi_x$	$\Delta\varphi_y$	$\Delta\varphi_z$
Δx	0.75	0	0	0	0	0
Δy	0	0.375	0	0	0	-0.2165
Δz	0	0	0.375	0	0.2165	0
$\Delta\varphi_x$	0	0	0	0.125	0	0
$\Delta\varphi_y$	0	0	-0.2165	0	-0.0625	0
$\Delta\varphi_z$	0	0.2165	0	0	0	-0.0625
(b)	Δx	Δy	Δz	$\Delta\varphi_x$	$\Delta\varphi_y$	$\Delta\varphi_z$
Δx	0.7509	-0.0001	-0.0012	0.0008	0.0016	0.0004
Δy	0.0012	0.3760	0.0009	-0.0011	-0.0011	-0.2168
Δz	-0.0011	-0.0002	0.3739	-0.0011	0.2167	0.0005
$\Delta\varphi_x$	0.0009	-0.0001	0.0000	0.1246	-0.0004	0.0003
$\Delta\varphi_y$	0.0003	-0.0006	-0.2166	-0.0010	-0.0621	0.0004
$\Delta\varphi_z$	-0.0008	0.2173	-0.0007	-0.0004	0.0005	-0.0630

Table 4.1: Components of the correlation factors C_{ij} for translational and rotational displacements of two spherical particles with radii a positioned at coordinates $(-a, 0, 0)$ (particle 1) and $(a, 0, 0)$ (particle 2): (a) theoretical values, (b) results according to eq. (4.9), calculated from 10^6 single-step simulations. Columns correspond to particle 1 and rows correspond to particle 2.

eq. (2.16), the cross-correlation factors from eq. (4.1), i.e., the sub set of C_{ij} for different particles translate into

$$\begin{aligned}
C_{kl}^T &= (\mathbf{D}_{12}^{\mathbf{T}})_{kl} / (\mathbf{D}_{11}^{\mathbf{T}})_{kk}, \\
C_{kl}^{TR} &= C_{kl}^{RT} = (\mathbf{D}_{12}^{\mathbf{TR}})_{kl} / \sqrt{(\mathbf{D}_{11}^{\mathbf{T}})_{kk} (\mathbf{D}_{11}^{\mathbf{R}})_{kk}} \text{ and} \\
C_{kl}^R &= (\mathbf{D}_{12}^{\mathbf{R}})_{kl} / (\mathbf{D}_{11}^{\mathbf{R}})_{kk}, \text{ with } 1 \leq (k, l) \leq 3.
\end{aligned} \tag{4.9}$$

The theoretical values computed from eqs. (4.9) for the example discussed above are shown in Table 4.1 (a). Comparison with the corresponding values calculated with eq. (4.1) from the simulation shows very good agreement (cf. Table 4.1 (b)). It should be emphasised that this is meant only as a test for the correctness of the code developed for this work. As mentioned in ref. [36], in the case of close-touching spheres, i.e. strong hydrodynamic coupling, the asymptotic expansions of the diffusion tensor are not valid and one would expect all the non-zero coefficients in Table 4.1 to equal unity.

4.2 The influence of hydrodynamic interactions

An important point before starting more detailed simulations is to check the influence of standard hydrodynamics. For that purpose several simulations with and without hydrodynamics for different concentrations were performed. A possible influence should then manifest in different diffusion coefficients and also in different particle distributions in the simulation box.

In computer experiments diffusion coefficients are usually measured by using the Einstein relation

$$D(t) = \frac{1}{6Nt} \left\langle \sum_{i=1}^N (\vec{r}_i(t) - \vec{r}_i(0))^2 \right\rangle, \quad (4.10)$$

for various time intervals $\Delta t = t$ and N particles. The measurement of diffusion coefficients only makes sense in an infinite system. That is the reason why we assumed periodic boundary conditions in x - and y -directions, reflecting boundary conditions at the upper wall and the usual membrane at $z = 0$. With these boundary conditions diffusion parallel to the membrane surface is determined as

$$D_{\parallel}(t) = \frac{1}{4Nt} \left\langle \sum_{i=1}^N ((x(t) - x(0))^2 + (y(t) - y(0))^2) \right\rangle. \quad (4.11)$$

We investigated two different regimes separately, a low and medium and a large concentration regime. Technically, this was achieved by simulating in two different boxes. The low and medium concentration calculations were performed in a $30 \times 30 \times 30 \text{ nm}^3$ box and the large concentrations were achieved by using a $20 \times 20 \times 20 \text{ nm}^3$ box. All these simulations were performed both with and without standard hydrodynamics which were then compared to each other. It has to be mentioned that due to the periodic boundaries in x - and y -directions the next-neighbour image procedure was used for all kinds of interactions, i.e., a cutoff-radius of half the box width. On the other hand, due to the leading $1/r$ terms in the Rotne-Prager matrix hydrodynamic interaction must be considered as long-ranged. That would suggest the use of Ewald summation [46]. But the use of a cutoff can be justified in the following way: consider the velocity of sound waves in water which is about 1400 m/s. During one Brownian time step of 10 ps such a wave would cover a distance of about 15 nm which is half of the box length used above. Consequently, in the common Rotne-Prager creeping flow picture hydrodynamic interaction cannot be mediated between

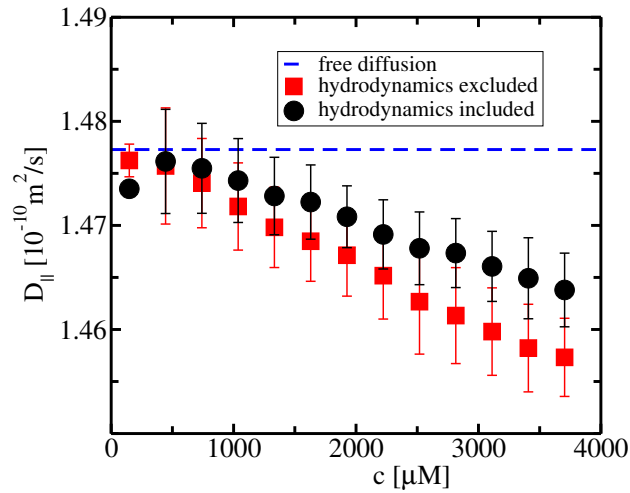


Figure 4.1: Diffusion coefficients $D_{||}$ parallel to the membrane surface in the small/medium particle concentration regime. Since data were usually written to file after 50 time steps of 10 ps each, we chose $\Delta t = 0.5$ ns in eq. (4.11) for all diffusion measurements presented.

particles at larger distances than 15 nm anyway. Thus, Ewald summation would not make any sense within one time step.

Figure 4.1 shows the diffusion coefficients computed using eq. (4.11) for small and medium concentrations. For very dilute solutions the particles diffuse almost freely in both cases with and without hydrodynamic interaction. With growing particle concentration the diffusion coefficients decrease only slightly. For $c_{\text{cyt}} \simeq 3700 \mu\text{M}$ the difference between free diffusion and diffusion with hydrodynamics is only about 0.9%. Without hydrodynamics that difference accounts to 1.4%. Figure 4.2 illustrates the progression of the diffusion coefficients in the large particle concentration regime. As expected, diffusion becomes slower with growing concentrations in both cases with and without hydrodynamics. But after reaching minima at about $c_{\text{cyt}} = 7500 \mu\text{M}$ without and at about $c_{\text{cyt}} = 9000 \mu\text{M}$ with hydrodynamics, diffusion becomes faster.

The slight decrease of diffusional speed in the low concentration regime is what one would expect. The more particles are present the slower they get because there is less space. As a consequence the friction coefficient increases and the diffusion coefficient (its inverse) decreases. This effect could also be shown using mean-field-hydrodynamics Brownian dynamics which yielded good agreement with experimental results [47, 48]. The decreasing free space is illustrated by the particle density profiles which show how many particles

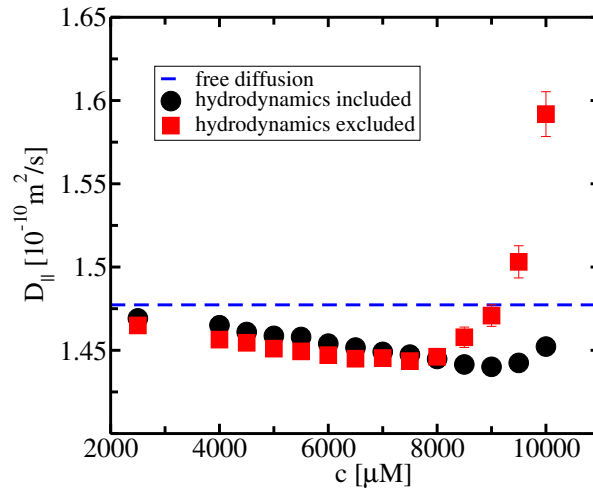


Figure 4.2: Diffusion coefficients $D_{||}$ parallel to the membrane surface in the high particle concentration regime.

are to be found at a certain distance from the membrane. Figure 4.3 shows the profiles in z -direction for three different small/medium concentrations, $c_{\text{cyt}} \simeq 148 \mu\text{M}$, $c_{\text{cyt}} = 741 \mu\text{M}$ and $c_{\text{cyt}} = 2222 \mu\text{M}$. The differences between the hydrodynamic and non-hydrodynamic situations are negligible. The peaks close to the membrane surface due to the electrostatic and van der Waals attraction of the membrane are higher for larger densities. Consequently, the free space close to the membrane becomes smaller and thus the diffusion coefficient decreases.

A hint why the effect of increasing diffusion coefficients occurs in the large concentration regime is given again by the according density profiles. The high concentration regime is represented by $c_{\text{cyt}} = 4000 \mu\text{M}$, $c_{\text{cyt}} = 7500 \mu\text{M}$ and $c_{\text{cyt}} = 10000 \mu\text{M}$ and is shown in Figure 4.4. Because of the larger amount of particles that are attracted by the membrane, the peaks are higher than for smaller particle densities. Also important is the fact that the side-effect from the reflecting wall at $z = z_0 = 20 \text{ nm}$ becomes larger: the box is slowly getting full. In the regions close to the membrane and in the vicinity of the upper wall, where the densities are high the particles cannot move properly anymore. Due to the high repulsive van der Waals forces at close distances a particle in these regions does quite long jumps from one interaction partner to the other. This results in larger values of the mean squared displacements. The growing, unphysical side-effects will become more distinct in the next

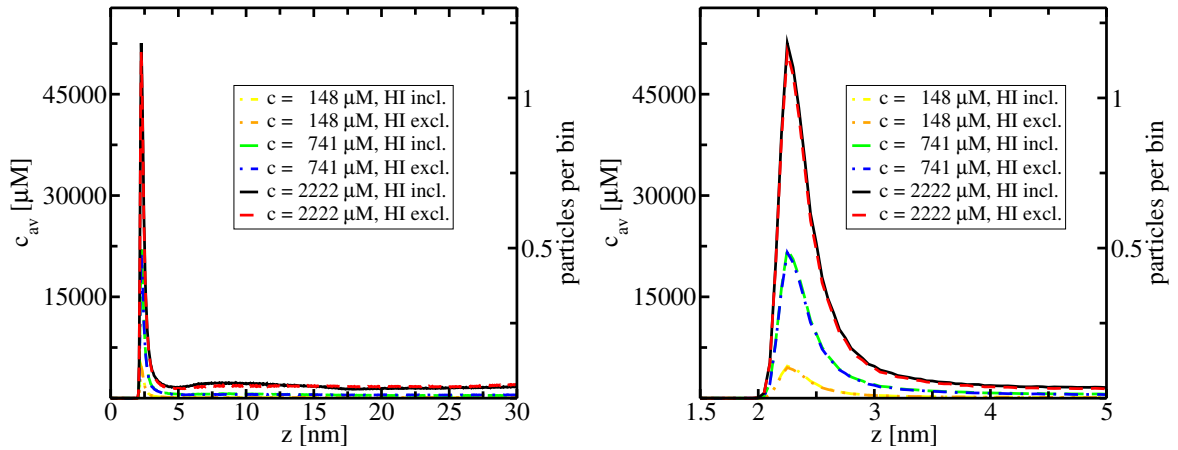


Figure 4.3: Left panel: cyt c distribution along the z -axis for three different low/medium concentrations, each with and without hydrodynamics. z is the particles' centre-of-mass distance from the membrane surface. For this analysis the box was divided into 600 bins of volume $\Delta V = 30 \times 30 \times 0.05 \text{ nm}^3$ each. c_{av} is the average concentration per bin in moles per litre. Right panel: cyt c distribution from the left panel zoomed in on the vicinity of the membrane surface.

section for even larger particle densities.

Before moving towards macromolecular crowding in the next section, the orientation of the particle dipole and the influence of the van der Waals interaction between cyt c and the membrane are briefly examined. Figure 4.5 shows the average cosine of the rotation angle as illustrated in the inset. Far from the membrane, i.e., for $z \geq 6 \text{ nm}$ the values fluctuate around zero with very small amplitudes. This means that on average the dipoles of the N particles in that region can have all possible orientations with respect to the membrane. The closer the Brownian particles get to the negatively charged surface the more do the dipole angles shift towards values larger than $\alpha = 90^\circ$. The positive dipole charges are thus orienting towards the negative surface charge at short distances. Hydrodynamics does not have an influence on that.

Figure 4.6 shows the density profiles from two simulations without hydrodynamics. The first simulation is the one studied also in Figure 4.5 (surface charge density $\sigma = -1.3 \text{ e}_0/\text{nm}^2$). The second one is the same except that it excludes electrostatic interaction between cyt c and the membrane, i.e., $\sigma = 0$. The profile for the uncharged membrane shows a smaller peak and a larger tail (particle number must be the same in total). The particle

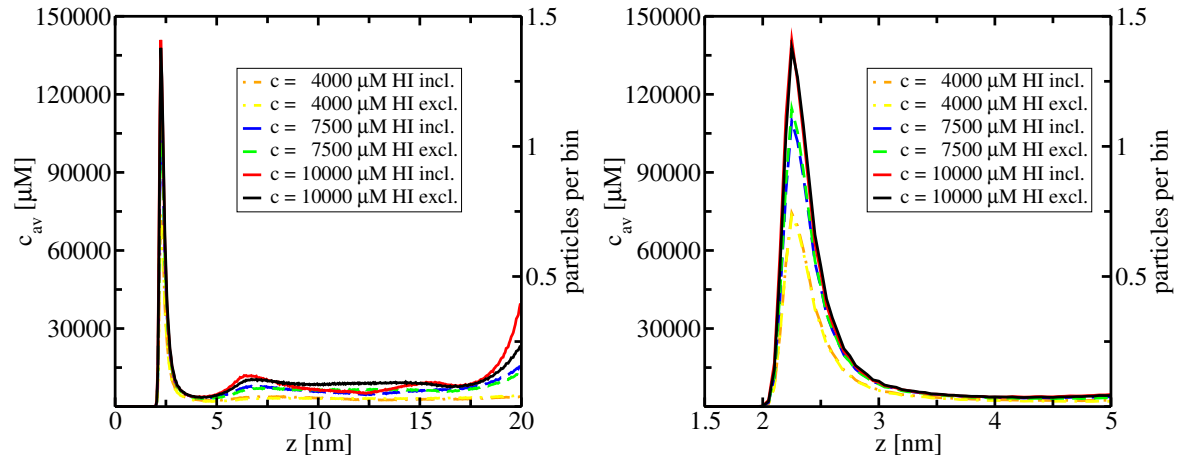


Figure 4.4: Left panel: c_{av} distribution along the z -axis for three different large concentrations, each with and without hydrodynamics. z is the particles' centre-of-mass distance from the membrane surface. For this analysis the box was divided into 400 bins of volume $\Delta V = 20 \times 20 \times 0.05 \text{ nm}^3$ each. Right panel: c_{av} distribution from the left panel zoomed in on the vicinity of the membrane surface.

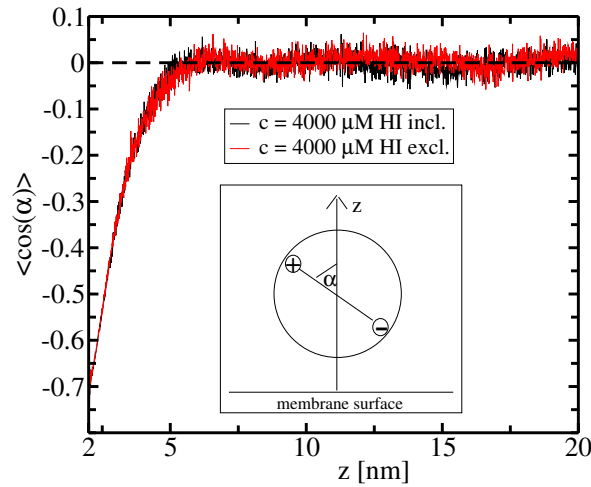


Figure 4.5: Average of the cosine of the dipole orientation as illustrated in the inset for two simulations with and without hydrodynamic interaction. The average is computed with respect to bins of length $\Delta z = 0.01 \text{ nm}$. The angle trajectories from two simulations which were also analysed in Figure 4.4 are used for this analysis (box dimension: $20 \times 20 \times 20 \text{ nm}^3$).

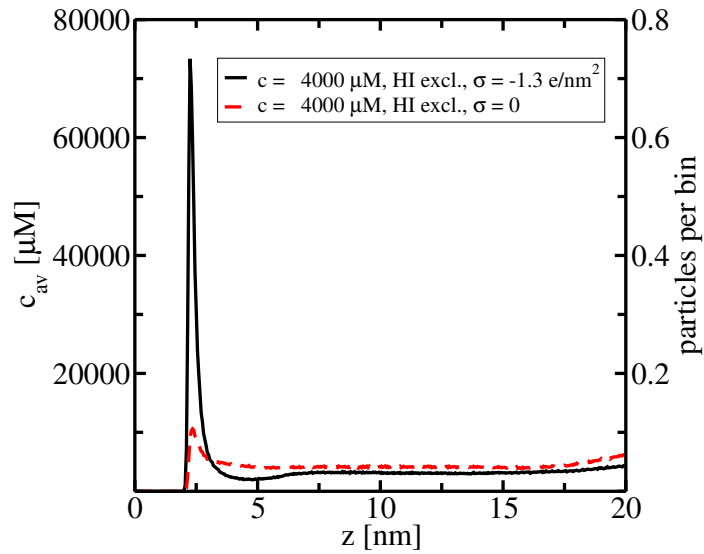


Figure 4.6: Comparison between cyt c distributions along the z -axis for simulations with charged and uncharged membrane surface. For this analysis the box was divided into 400 bins of volume $\Delta V = 20 \times 20 \times 0.05 \text{ nm}^3$ each (box dimension: $20 \times 20 \times 20 \text{ nm}^3$).

attraction is only a result of the van der Waals interaction and therefore much weaker. From the fact that the peak for the charged membrane is about 7 times higher one can conclude that “binding” to the membrane is only about 14% due to van der Waals interaction.

4.3 A first step towards macromolecular crowding

As discussed in ref. [49] macromolecular crowding apparently plays an important role in many cellular processes. The last section already addressed this problem partially by varying the concentrations of one particle species. But crowding also implies the existence of various different molecules. A first step towards crowding in this work is to put additional spherical molecules into the simulation box. These particles are supposed to interact only via van der Waals and hydrodynamic forces with the cyt c molecules.

Again, we split the analysis into small/medium and high concentration regimes and compare the diffusional behaviour and the resulting particle distributions between hydrodynamic and non-hydrodynamic situation. The small density simulations were performed in a $30 \times 30 \times 30 \text{ nm}^3$ box with 20 additional dummy particles of the same size as cyt

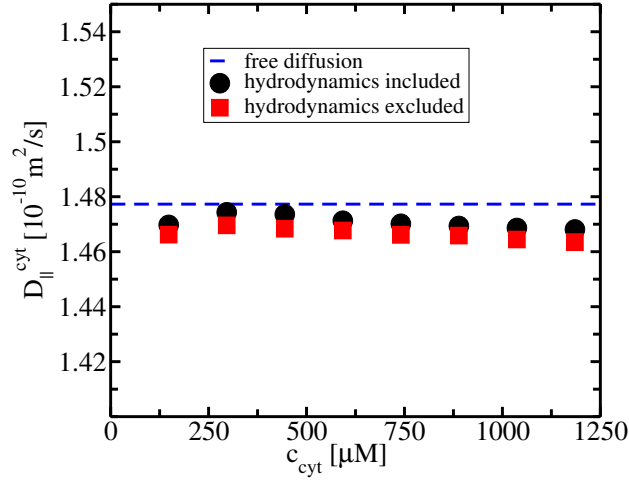


Figure 4.7: Diffusion coefficients D_{\parallel} parallel to the membrane surface in the small/medium particle concentration regime with additional dummy particles (box dimension: $30 \times 30 \times 30 \text{ nm}^3$).

c (radius $R = 1.66 \text{ nm}$), i.e., $c_{dummy} \simeq 1481 \mu\text{M}$. Considering their van der Waals radii, these particles occupy only 2% of the box volume. The effect due to the additional particles should be negligible. Because of the higher computational cost for extra dummies, the large concentration simulations were carried out in a $15 \times 15 \times 15 \text{ nm}^3$ box with the same amount of dummy particles. So, in this case the dummies occupy 15% of the box volume and $c_{dummy} \simeq 11852 \mu\text{M}$. In this case one would expect an influence of the extra particles.

Figures 4.7 and 4.8 show the resulting cyt c diffusion coefficients D_{\parallel}^{cyt} for the two concentration regimes in the presence of additional dummy particles. Like in the situation without dummies the diffusion coefficients for cyt c are at first decreasing with growing concentrations in the small/medium density regime but on a much lower level. In fact, the diffusion is almost the same like for free diffusion. The slight decrease indicates that the dummies simply hinder the motion of the cyt c molecules a little bit in this density regime. The results are nearly equal for simulations with and without hydrodynamics and in both cases diffusion is slower than for free particles but the differences are almost negligible.

That changes drastically for higher densities. In that regime the diffusion coefficients at first rise up to more than two orders of magnitude at $c_{cyt} \simeq 3500 \mu\text{M}$ without hydrodynamics. The increase using hydrodynamics is slower but the same peak at $D_{\parallel} \simeq 190 \times 10^{-10} \text{ m}^2/\text{s}$ is reached at $c_{cyt} \simeq 6000 \mu\text{M}$. For even higher concentrations the diffusion decreases again with

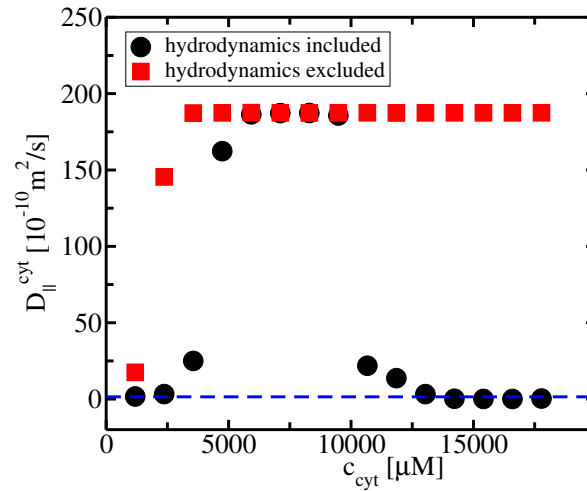


Figure 4.8: Diffusion coefficients D_{\parallel} parallel to the membrane surface in the high particle concentration regime with additional dummy particles (box dimension: $15 \times 15 \times 15 \text{ nm}^3$).

hydrodynamics and apparently approaches free diffusion. Without hydrodynamics, however, the diffusional speed remains constant at the “saturation” diffusion coefficient of $D_{\parallel} \simeq 190 \times 10^{-10} \text{ m}^2/\text{s}$.

In order to understand these effects we have again a look at the particle distribution profiles for the small/medium and high density regimes. The small/medium regime is again characterised by very distinct peaks close to the membrane without significant side effects close to the reflecting wall at $z = z_0 = 30 \text{ nm}$ as is shown in Figure 4.9. The situation is very similar to the one without additional particles where the slight decrease of the diffusion coefficients also occurred. In the large density regime growing side-effects occur. Figure 4.10 and the according distributions of the dummy particles in Figure 4.11 illustrate that. Larger $\text{cyt } c$ concentrations do not result in higher peaks close to the membrane because many particles stick more or less to the reflecting border at $z = z_0 = 15 \text{ nm}$ and do not reach the membrane (Figure 4.10). There is an additional problem both for $\text{cyt } c$ and dummy particles: the region $z \leq 2 \text{ nm}$ which used to be free of particles shows a non-vanishing particle density now. The reason is that the box is getting too crowded. Due to the high densities close to the membrane it can happen that particles jump to $z \leq 0$. In such cases CESIP simply reflects the particles back into the box. Unfortunately, one has to conclude that these high concentration simulations do not make sense physically: the large diffusion

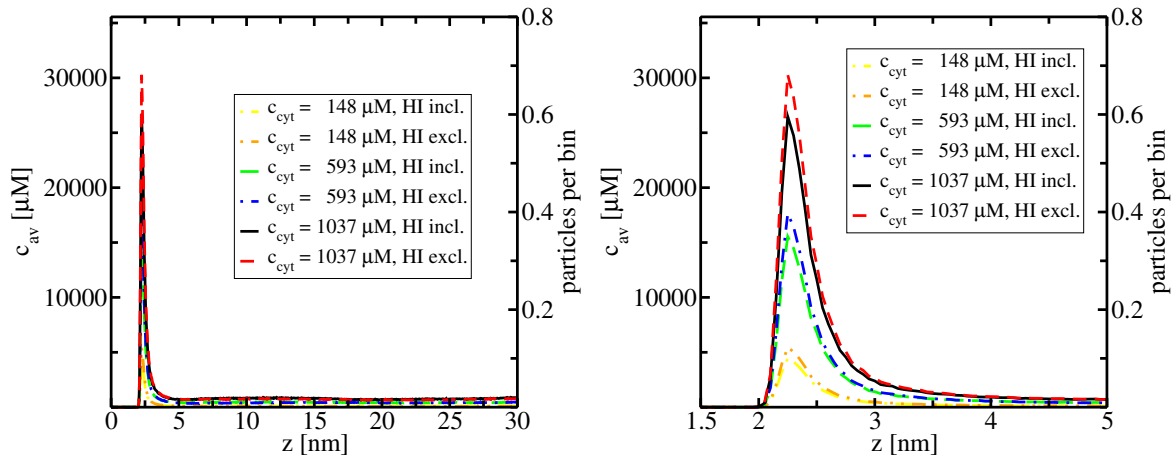


Figure 4.9: Left panel: cyt c distributions in z -direction in the presence of additional dummy particles of radii $R_{dummy} = 1.66$ nm for three different small/medium cyt c densities each with and without hydrodynamics (small/medium concentration regime, box dimension: $30 \times 30 \times 30$ nm³, bin length $\Delta z = 0.05$ nm). Right panel: cyt c distributions from the left panel zoomed in on the vicinity of the membrane surface.

coefficients shown in Figure 4.8 can again be attributed to “jumping” particles close to the membrane and close to the reflecting wall. But interestingly, the effect is less dramatic with hydrodynamics close to the membrane. Hydrodynamics weakens the effect of particles crossing the membrane as can be seen from the profiles.

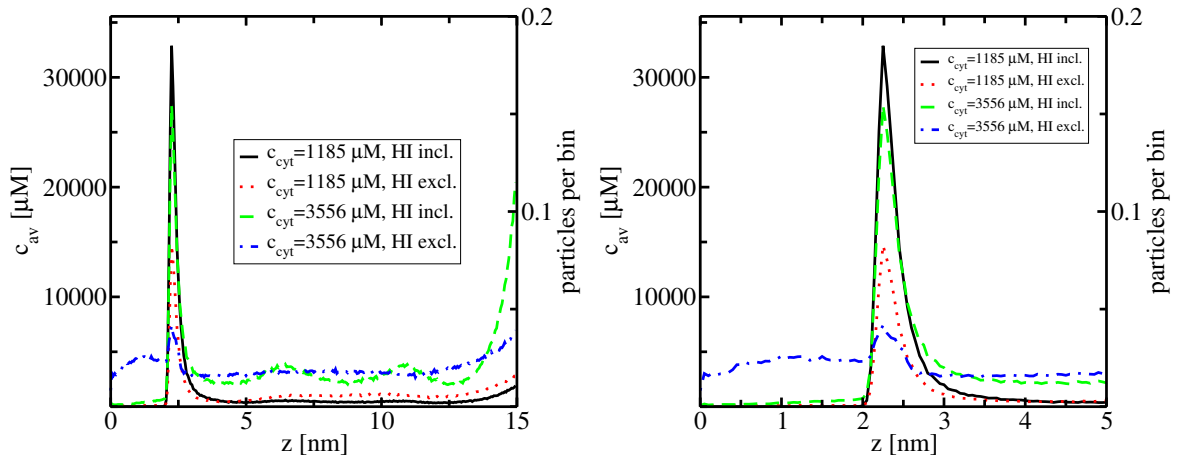


Figure 4.10: Left panel: cyt c distributions in z -direction in the presence of additional dummy particles of radii $R_{dummy} = 1.66$ nm for two different large cyt c densities each with and without hydrodynamics (high concentration regime, box dimension: $15 \times 15 \times 15$ nm³, bin length $\Delta z = 0.05$ nm). Right panel: cyt c distributions from the left panel zoomed in on the vicinity of the membrane surface.

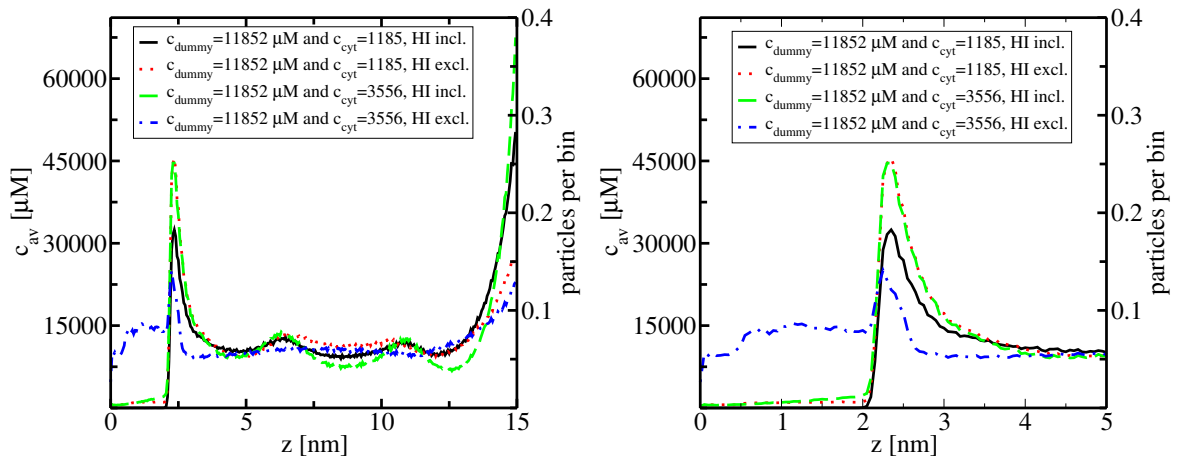


Figure 4.11: Left panel: dummy distributions in z -direction for two different large cyt c densities each with and without hydrodynamics. The dummies' radius is $R_{dummy} = 1.66$ nm and the density is $c_{dummy} = 11852$ μM (high concentration regime, box dimension: $15 \times 15 \times 15$ nm³, bin length $\Delta z = 0.05$ nm). Right panel: dummy distribution from the left panel zoomed in on the vicinity of the membrane surface.

Chapter 5

Simulations and results for $N \neq \text{const.}$

This chapter mainly presents results recently accepted for publication [50]. The new particle insertion algorithm combined with reflecting boundaries as described in subsection 2.3.3 is utilised and thus, the number N of particles in the simulation box is not constant. The analysis focusses on concentration profiles calculated from the particle trajectories. These allow a comparison between the simulations and experiments in which binding isotherms for the association of horse heart cyt c with dioleoyl phosphatidylglycerol (DOPG)/dioleoyl phosphatidylcholine (DOPC) membranes were measured [1].

5.1 Equilibration

A priori we do not know the equilibrium state of the simulated system - or there would be no need for any simulation. We therefore have to guess an initial (nonequilibrium) setup and then let the system relax into its stationary state. In simulations with a fixed number of proteins ($N = \text{const.}$), i.e., without the interfacing algorithm of subsection 2.3.3, we initially distribute the proteins randomly throughout the simulation volume. With the insertion algorithm it is more convenient to start from an empty box which is then filled with particles by the simulation algorithm. Figure 5.1 shows a typical example: starting from an empty box, the number of particles first increases linearly. Apparently all particles that are inserted at z_0 diffuse to the membrane and bind there. The system equilibrates to the externally given density of $c_0 = \rho_0 = 7500 \mu\text{M}^1$ when after about 10^5 time steps of 10 ps enough proteins

¹Note that in the following discussion the interface densities (concentrations) are denoted by c instead of ρ . The reason is that in many publications like in ref. [1] concentrations are denoted by c and given in units of

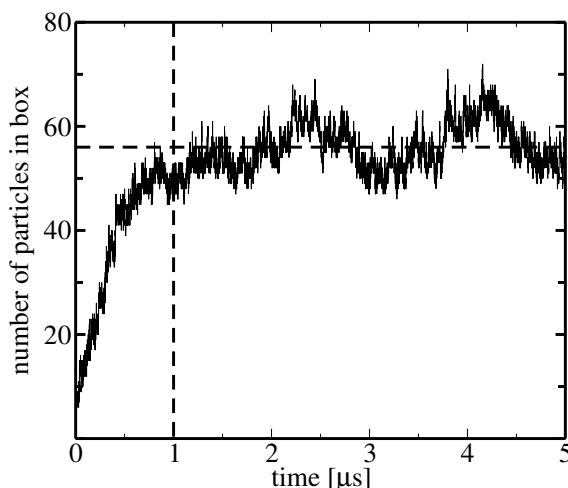


Figure 5.1: Equilibration of the particle number: plot of the total number of particles in a simulation in a $30^2 \times 20 \text{ nm}^3$ box with an interface density $c_0 = 7500 \mu\text{M}$. After about $1 \mu\text{s}$ (vertical broken line) the system can be considered as equilibrated and the total number of particles fluctuates around a constant value of ~ 56 proteins.

have bound to the wall. This relaxation time of $\sim 1 \mu\text{s}$ corresponds to the free diffusion time $T_D = \frac{z_0^2}{2D_0} = 1.3 \mu\text{s}$ through the height z_0 of the simulation volume. After a time T_D the total number of particles in the simulation box fluctuates around a constant average value. The analysis of the simulation only starts after the equilibration phase, i.e., at $t \sim 1 \mu\text{s}$ in Figure 5.1. The total simulation times of the various simulations presented here vary in the range between $10 \mu\text{s}$ and 1 ms .²

5.2 Concentration profiles and bond length

In order to compare the measured binding isotherms of ref. [1] to our computer simulations, we need a criterion to decide when a protein is bound to the membrane. To extract this parameter we deduce concentration profiles from the computed particle trajectories as

moles of solute per litre of solution (molarity).

²In most plots in this work no error bars are shown because they are very small for long simulation times. For $N \neq \text{const}$ it is assumed that the standard deviation of the number of particles N is proportional to its square root \sqrt{N} . Using this assumption, all standard deviations are calculated according to the error law of Gauss.

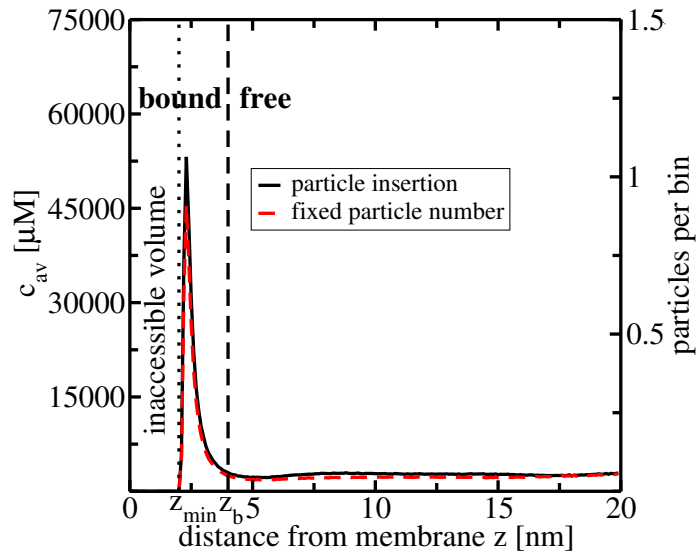


Figure 5.2: Comparison of concentration profiles for simulations with and without particle insertion for $c_0 = 3000 \mu\text{M}$. The simulation box has dimensions $20^2 \times 20 \text{ nm}^3$. c_{av} is the average concentration per bin. A bin length of $\Delta z = 0.1 \text{ nm}$ was used (as for all distribution analyses in this chapter) which corresponds to a bin volume of $\Delta V = 20^2 \times 0.1 \text{ nm}^3$ here.

was already done in Chapter 4 for constant particle simulations. These profiles show the probabilities of finding particles at a given distance from the surface.

At first we compare simulations with a fixed number of particles to simulations using the insertion algorithm. With a fixed particle number, the equilibration phase takes much longer. Apart from that, the resulting density profiles are equal, as shown in Figure 5.2. To facilitate comparison, the external density for the insertion algorithm was set to the equilibrium density that had developed in the fixed number simulation far above the membrane, i.e., at $z > 10 \text{ nm}$. The density profiles consist of a very sharp peak of particles close to the membrane followed by a rapid decrease to the bulk density. The distance where c blends into the bulk density is considered as bond length z_b . In all cases shown here we use a value of $z_b = 4 \text{ nm}$. It should be noted that the results vary only slightly with the exact value of z_b .

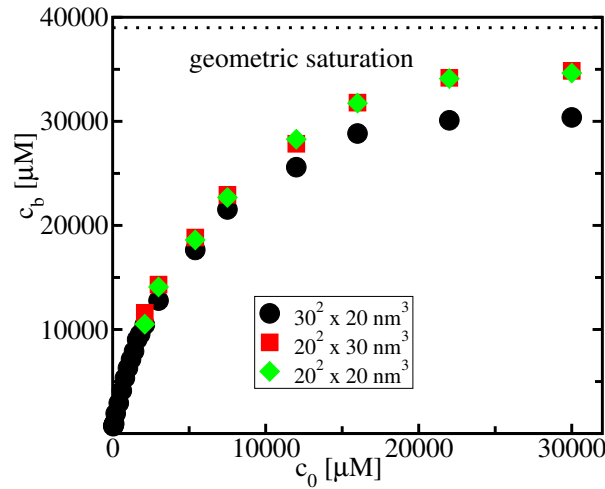


Figure 5.3: Comparison of binding isotherms for different box sizes. For determining the bound concentration a value of $z_b = 4$ nm was used that was estimated from the concentration profiles (see, e.g., Figure 5.2). The interface concentrations c_0 correspond to an average number of 8...90 particles in the simulation box.

5.3 Binding isotherms

As shown in Figure 5.2 there is an inaccessible volume for $0 < z < z_{min} = 2$ nm due to the van der Waals repulsion of the membrane. The integrated density of particles between the minimal distance of z_{min} from the membrane and the previously determined bond length z_b gives the amount of bound particles or, correspondingly, the bound concentration c_b . This reduced volume has to be taken into account when determining bound concentrations. By calculating c_b for simulations with different interface densities c_0 and plotting c_b vs. c_0 one can derive binding isotherms which show how many molecules are actually bound to the charged surface. The binding isotherms deduced from the concentration profiles are shown in Figure 5.3 for three different box sizes. Considering only the van der Waals radius of the particles, the maximal geometric saturation of the membrane surface equals $c_b \simeq 39000 \mu\text{M}$, corresponding to 64 particles bound to a 30^2 nm^2 membrane. The difference between this value and our results can be attributed to the electrostatic repulsion between the proteins. This value is also the limit for the bulk density c_0 .

In the experiment of ref. [1] bound concentrations are related to the total bulk volume which we do not specify and simulate explicitly. This difference between the bound con-

centrations computed here and the ones given in ref. [1] does not change the shape of the binding isotherms but only their absolute values.

5.4 Effective membrane area

The binding isotherms of Figure 5.3 are not independent of the box size: those for the two simulations with the same membrane size (20^2 nm^2) but different box heights coincide, but the result with the bigger membrane (30^2 nm^2) is remarkably smaller. In order to check the influence of the xy -boundaries (the “side walls”: reflecting boundaries in x - and y - directions) several box dimensions were tested.

Generally, for wider boxes the membrane concentrations are smaller. The effect increases with the total concentration. This indicates an increasing influence of the box walls where the particles are simply reflected. With periodic boundary conditions the density distribution parallel to the membrane is flat which is also the case for noninteracting particles between reflecting walls. In fact for noninteracting particles both boundary conditions are equivalent.

The effect of the particle-particle interaction can be seen in the concentration profiles parallel to the membrane, i.e., in x - and y -directions. In Figure 5.4 this profile is compared to the density perpendicular to the membrane (cf. Figure 5.2). In the central part of the simulation volume both concentration profiles are the same, as should be, since the influence of the boundaries is minimal. The system is more or less isotropic in that region. A closer look at the profile parallel to the membrane (inset of Figure 5.4) shows that the walls’ effect extends up to about 5 nm from the box walls. The peaks close to the box walls result from a net pressure towards the walls from the overall repulsion between the proteins. Only in the central part of the box the profile is constant as expected. Thus, an effective box size is defined as that inner part of the membrane area, where the average particle number in the x - and y -directions is constant. In the above example the effective box width is $w_{eff} = (30 - 2 \times 5) \text{ nm} = 20 \text{ nm}$.

The influence of the actual effective box width is shown in Figure 5.5. In both x - and y -directions $b \text{ nm}$ are removed from the box volume, i.e., $w_{eff} = (w - 2*b) \text{ nm}$. In the range of about $w_{eff} = 5 \dots 20 \text{ nm}$ in a box of width $w = x_0 = y_0 = 30 \text{ nm}$ the bound concentrations do not change. Again it becomes clear that the smaller the densities the smaller the side-effects from the walls. E.g., for $c_0 = 2100 \mu\text{M}$ the bound concentrations are almost constant over the whole range of possible effective box widths.

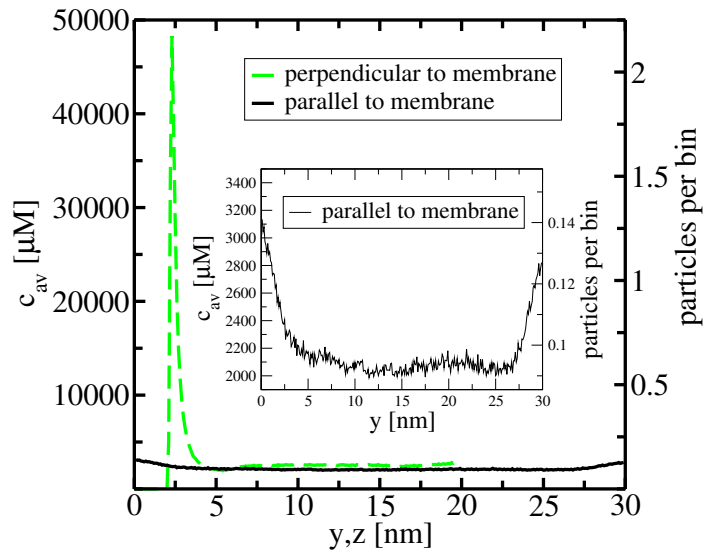


Figure 5.4: Comparison between particle profiles parallel, i.e., in y -direction and perpendicular (z) to the membrane in a box of dimensions $30^2 \times 20 \text{ nm}^3$ for $c_0 = 3000 \mu\text{M}$. c_{av} is the average density per bin. Inset: magnified profiles in y -direction.

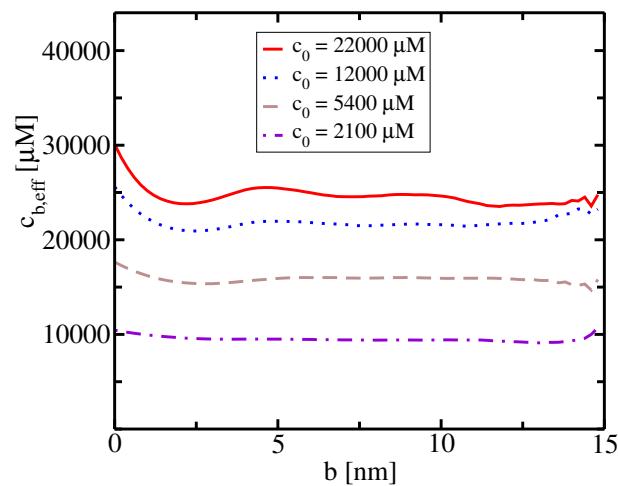


Figure 5.5: Effective bound concentrations against width of removed border b in a box of size $30^2 \times 20 \text{ nm}^3$.

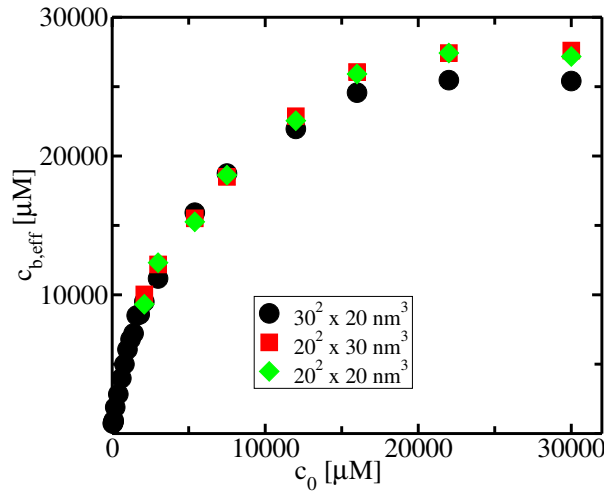


Figure 5.6: Using effective box sizes: comparison between effective binding isotherms for different box sizes. Again $z_b = 4$ nm was used. After examining the profiles parallel to the membrane the box size was reduced by 2×5 nm in both directions and only particles in that volume were considered.

Using effective box sizes, i.e., only particles from the central region, the analysis of Figure 5.3 was repeated. The results are shown in Figure 5.6. The difference between the bound concentrations is becoming smaller. Only for very large concentrations there is still a considerable difference. The box width is therefore no longer important, as long as it is not getting too small or, equivalently, as long as concentrations are not too large.

Besides the fact that the influence of the box walls can now be handled in an easy way, the main result here is that a saturation effect for large cyt c concentrations was found. Yet it is only a qualitative correspondence with the experiments of ref. [1], since there the saturation was already found for much smaller bulk concentrations. In the following section we show that the absolute values of the initial slope and the onset of saturation are very sensitive to the details of the protein-membrane interaction.

5.5 Towards membrane proteins

The membrane model used up to now is structureless. The interaction with the proteins is modelled by Coulomb and van der Waals potentials. The Coulomb potential is determined by the lipids' net charges and the ionic strength, whereas the van der Waals interaction was

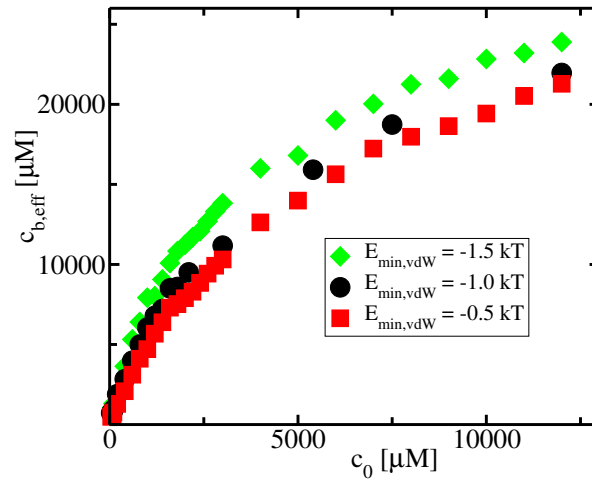


Figure 5.7: Comparison of binding isotherms for three different membrane van der Waals minima.

only estimated (see subsection 2.2.3). That is why we have to check its importance now before studying the influence of simplified membrane proteins.

5.5.1 Influence of the van der Waals potential depth and the surface charge of the membrane

Since the value for the depth of the van der Waals minimum of $E_{min,vdW} = -1 k_B T$ is just an estimate, it is necessary to check its influence on the binding isotherms. Figure 5.7 shows two additional binding isotherms for simulations with different well-depths compared to the results discussed earlier. A stronger van der Waals attraction ($E_{min,vdW} = -1.5 k_B T$) results in a slightly steeper slope at small concentrations. But in all cases the isotherms converge for higher bulk densities to the same geometrically defined saturation density. Consequently, the choice of the van der Waals depth is not critical, it has only a minor effect on the results. For more accurate values one might perform Molecular Dynamics simulations of a single cyt c molecule close to a lipid membrane, both modelled in atomistic detail.

It is clear that besides the influence of the van der Waals parameters a different membrane surface charge density would also change the binding isotherms. A change in the ratio of the membrane's DOPG:DOPC composition is equivalent to a change in the surface charge density. Thus, we also performed several simulations using $\sigma = -0.52 e_0/\text{nm}^2$ which corre-

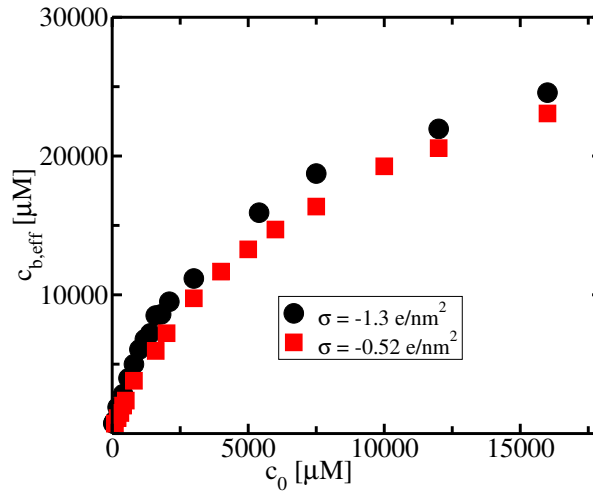


Figure 5.8: Comparison of binding isotherms for two different surface charge densities of the membrane. Note: for both sets of simulations $E_{min,vdW} = -1.0 k_B T$ was used. The black circles correspond to the black circles in Figure 5.7.

sponds to a lipid layer composed to 40 % of negatively charged DOPG and to 60 % of neutral DOPC. The comparison between the results for $\sigma = -1.3 e_0/\text{nm}^2$ and $\sigma = -0.52 e_0/\text{nm}^2$ is shown in Figure 5.8. The differences are surprisingly small. The maximum difference is found for $c_0 = 7500 \mu\text{M}$, where the bound concentration is still only about 13 % smaller in the case of a 40:60 DOPG:DOPC ratio.

The simulations performed in this context did not consider the rotational degrees of freedom so far. The dipole was always held fixed in parallel direction to the membrane surface. Therefore, simulations using a fixed vertical alignment with the positive dipole charge at the bottom of the spheres and also simulations with full rotational motion were performed. Figure 5.9 shows the results in comparison with the parallel dipole binding isotherm (red squares in Figure 5.8) for $\sigma = -0.52 e_0/\text{nm}^2$. In the case that the dipole is oriented towards the surface (perpendicular dipole) there is of course a stronger attraction due to the interaction of the positive dipole charge with the negatively charged membrane. Consequently, the bound concentrations are larger than for a parallel dipole. In the case that rotation is allowed one would expect a similar isotherm as for a perpendicular dipole because it would try to orient towards the membrane surface with its positive charge. This orientation effect was already shown in Figure 4.5 for $\sigma = -1.3 e_0/\text{nm}^2$. The same analysis was therefore done for one of the simulations with $\sigma = -0.52 e_0/\text{nm}^2$ from Figure 5.9. The result in comparison

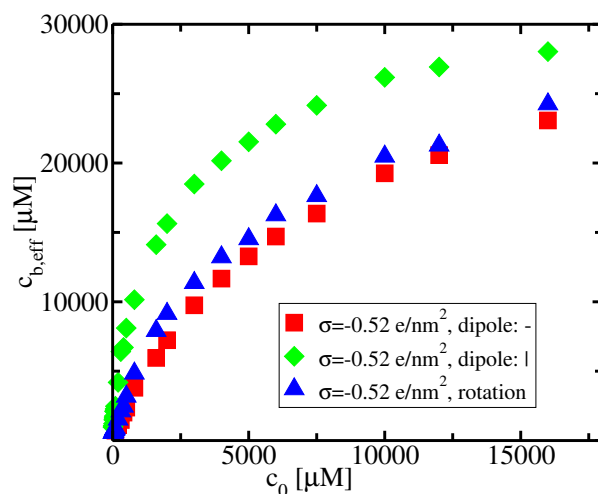


Figure 5.9: Comparison of binding isotherms for three different dipole alignments: dipole parallel, dipole perpendicular to membrane surface and free dipole rotation. The charge density of the membrane is $\sigma = -0.52 e_0/\text{nm}^2$. Note: the red squares correspond to the red data squares in Figure 5.8.

with the one for $\sigma = -1.3 e_0/\text{nm}^2$ from Figure 4.5 is shown in Figure 5.10. In both cases the orientation does only start for distances $z \leq 5$ nm (the region where the densities are highest). For the smaller surface charge density the orientation effect is smaller than for the larger charge density by about 17%. Thus, the electrostatic interaction with the membrane is quite weak for $\sigma = -0.52 e_0/\text{nm}^2$ which explains the difference between the binding isotherms for a perpendicular and a rotating dipole in Figure 5.9.

5.5.2 Reaction centres

As a step towards modelling a structured biological membrane with embedded membrane proteins, simplified reaction centres were added to the surface. This was done by adding a grid of negative charges to the membrane. A value of $-6 e_0$ for all charges was chosen, since this roughly corresponds to the net charge of the solvent-facing surface for the reaction centre of *Rhodobacter sphaeroides* 1PCR [13]. In contrast to other, more complicated membrane proteins such as cytochrome *c* oxidase with large external domains, the reaction centres are fully embedded into the lipid membrane. Therefore, as a first step, it appears reasonable to model them as flat disks with one central charge, as is done here. Three different grids with

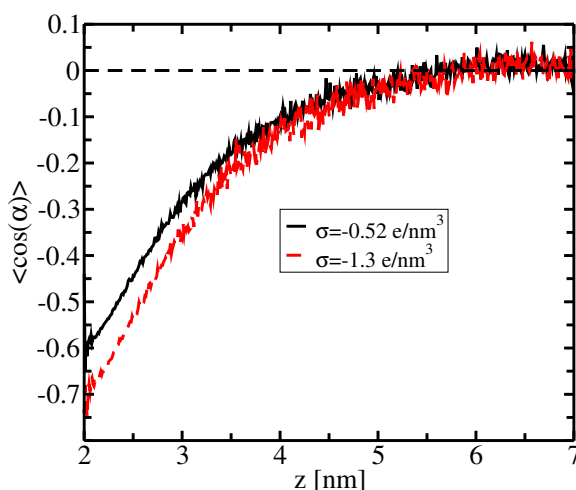


Figure 5.10: Average of the cosine of the dipole orientation as illustrated in Figure 4.5 for two different surface charge densities in the vicinity of the membrane. The curve for $\sigma = -1.3 \text{ e}_0/\text{nm}^2$ is the one from Figure 4.5 without hydrodynamics at $c_{\text{cyl}} = 4000 \mu\text{M}$ (no particle insertion). For $\sigma = -0.52 \text{ e}_0/\text{nm}^2$ the simulation including rotation from Figure 5.9 for the corresponding interface density $c_0 = 4000 \mu\text{M}$ was analysed. Note that the box dimensions are different but in both cases the box length is $z_0 = 20 \text{ nm}$.

3×3 , 4×4 and 5×5 charges were used in order to study the influence of the number of reaction centres on the membrane. Figure 5.11 shows the profiles parallel to the membrane for a typical simulation with 5×5 additional charges. No effective box size is needed for analysis here because the very high peaks due to the new binding sites outweigh by far the walls' side-effects. We emphasise that these additional charges modify the total surface charge density only slightly. With the highest number of additional charges used, i.e., 25 charges with -6 e_0 each, they contribute an additional surface charge density of $\sigma_{\text{grid}} \simeq -0.17 \text{ e}_0/\text{nm}^2$ which is about 13 % of the initial charge density. The binding isotherms for these simulations are depicted in Figure 5.12. At small concentrations up to about $c_0 = 3000 \mu\text{M}$, the “membrane proteins” are the main binding sites and, as a consequence, the saturation already occurs for much lower concentrations of about $500 \mu\text{M}$. This is two orders of magnitude closer to the experimental results than without the binding sites, though their influence on the net surface charge is small. The simulation is very sensitive to the geometric details of the model reaction centres. For very large interface densities the bound densities converge. The reason is that, especially with the small 3×3 grid, there is still enough space

in the gaps between the “binding sites”, where the molecules can be forced into when the density above the membrane is high enough.

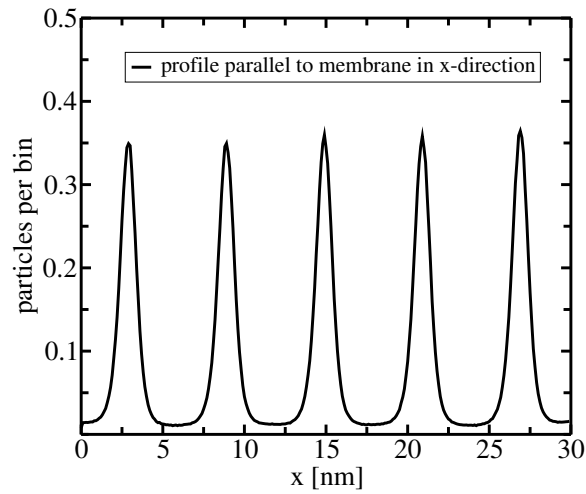


Figure 5.11: Influence of additional charges of $-6 e_0$ at the membrane surface: density profiles parallel to the membrane in x -direction. 25 charges of $-6 e_0$ each were positioned as a 5×5 square grid with a spacing of 6 nm. The box dimension is $30^2 \times 20 \text{ nm}^3$ and the interface density is $c_0 = 500 \mu\text{M}$.

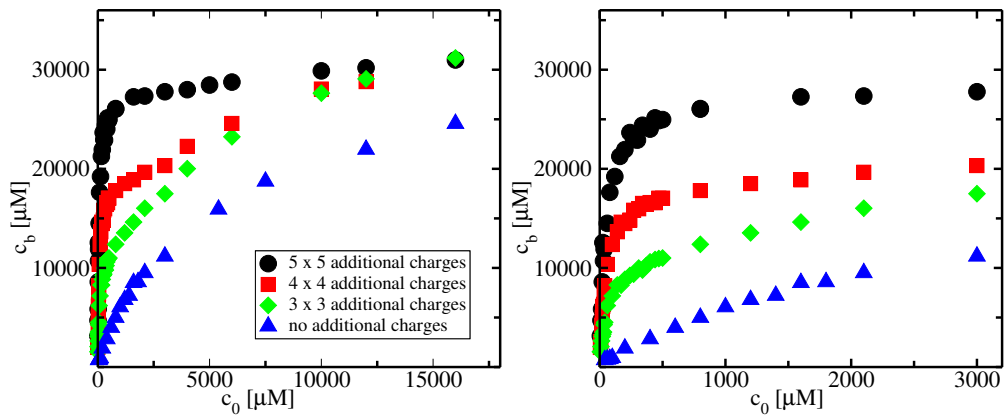


Figure 5.12: Comparison between binding isotherms for different charge grids in a $30^2 \times 20 \text{ nm}^3$ box. The panel on the right shows the small concentration regime from the left panel. As bond length for determining the bound concentration $z_b = 4 \text{ nm}$ was used.

Chapter 6

Simulations and results including a simple model for photosynthetic units

In a coarse-grained simulation approach like the one used in this thesis it is crucial to apply care when modelling complex systems. Hence, before modelling the very complex system of the photosynthetic units as described in the introduction, the single point charge approach for reaction centres was tested in the previous sections. The curve progression in Figure 5.11 maps the particle distribution of the point reaction centres on the membrane very well and the high concentration peaks indicate that these point charges are the preferential binding sites. A real reaction centre and an entire photosynthetic unit (PU) of course also have a volume extension which is totally neglected by a single point approach. Consequently, the next step is to take the systems topology into account as well. The computer code used for the simulations in this work can imitate the spatial extension of a molecule by using van der Waals spheres. On this level of approximation a PU would then consist of several van der Waals spheres containing point charges. In the following simulation hydrodynamics is not included. However, the particles' rotational degrees of freedom are considered because the dipole needs to be able to orient towards the oppositely charged membrane proteins.

As described in the introduction and shown in Figure 1.5 the PUs are regularly arranged on a grid in nature. The simulations presented in the following were performed with two times two such units placed in the membrane of a $60 \times 40 \times 40 \text{ nm}^3$ rectangular box. In order to be able to focus on the interaction between cyt *c* and PU the membrane surface is chosen to be uncharged and therefore only exerts short-ranged van der Waals interactions on the Brownian particles. The overall dimensions were derived approximately from Figures 1.5

and 1.6 [12]. Information about the complexes' dimensions and their electrostatic charges was extracted from various publications. E.g., Kühlbrandt *et al.* presented the structure of the light-harvesting chlorophyll *a/b*-protein complex, determined at 3.4 Å by electron crystallography [51, 52]. The ring structure of LHCs resolved by atomic force microscopy is described in ref. [53] and there also exists a Protein Data Bank entry 1LGH for the crystal structure of LHCII of *Rhodospirillum molischianum* [54]. For modelling the bc_1 complex the data base entry 1KYO was used. This is the crystal structure of the yeast cytochrome bc_1 complex with bound cyt *c* [55]. Finally, Michel *et al.* published the structure of the photosynthetic reaction centre from *Rhodobacter sphaeroides* at 2.65 Å resolution [13]. The according data base entry 1PCR was used for the models presented here.

Three test models were constructed from the aforementioned sources and simulations were performed using particle insertion with reflecting side walls as described in 2.3.3. Model 1 includes a bc_1 complex whereas models 2 and 3 do not. These two differ in the z positions of their RCs as described below. The reason why two models excluding a bc_1 complex are investigated is that Siebert *et al.* raised the question of its location in ref. [56]. No detectable amounts of bc_1 and thus only RC-LH1-PufX complexes could be found in their tubular membrane probes. PufX is a polypeptide which is suggested to be localised within the ring of LHCs. It may act as a portal for quinol export from the RC to the quinone pool, prior to reducing the bc_1 complex [57]. This single polypeptide affects the membrane morphology and is currently discussed in many publications like refs. [56], [57] or [58]. However, the authors of ref. [56] emphasise that their data do not prove that RC-LH1-PufX-cytochrome bc_1 complexes do not exist, only that they are not to be found in tubular membranes. Since the localisation is not yet clear, no model for PufX is included in our simulations.

Figure 6.1 shows the positions of the point charges assigned to each complex of four PUs. For the sake of clarity the van der Waals spheres surrounding each of the point charges are not shown here. Each LHC is modelled as a van der Waals sphere of radius $r_{LHC} = 1$ nm with its centre positioned at $z = 0$, i.e., exactly on the membrane surface so that a 1 nm hemisphere peaks out of the surface. Each of these spheres carries a point charge of $q_{LHC} = -4 e_0$ placed on its north pole. The RCs are modelled as spheres of radii $r_{RC} = 3$ nm with their centres positioned at $z = -2$ nm. Each RC is assigned a charge of $q_{RC} = -6 e_0$. In model 1 and 2 these charges are placed at $z = 0$, i.e., at 1 nm below the north pole whereas in model 3 they are put at $z = 1$ nm, i.e. directly on the north pole. The additional

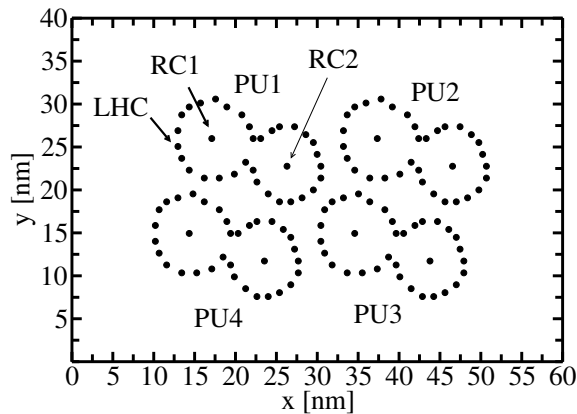


Figure 6.1: Position of the point charges assigned to the various complexes of four photosynthetic units. Each model photosynthetic unit (PU) consists of 16 light harvesting complexes (LHC) and 2 reaction centres (RC). Not shown here are the positions of the bc_1 complexes which are located in-between the two RCs of one PU each (cf. Figure 6.2).

bc_1 complexes between the two RCs in model 1 consists of two overlapping spheres of radii $r_{bc_1, left} = r_{bc_1, right} = 2.5$ nm with their centres at $z = 1$ nm. Both are assigned charges of $q_{bc_1, left} = q_{bc_1, right} = -10 e_0$ at $z = 3$ nm. Figure 6.2 illustrates the sphere and charge positions and dimensions of the different parts of one PU.

Figure 6.3 shows the concentration profiles in z -direction obtained for the three different models. The first significant difference in comparison with the profiles in Figure 5.2 is the shifting of the peak from $z_{max} \simeq 2.3$ nm to $z_{max} \simeq 3.2$ nm. This is due to the extension of the LHC and RC van der Waals spheres and their charges into the periplasm. The second noticeable difference is the small peak at $z \simeq 5.6$ nm in model 1 because of the extension of the bc_1 complex. As a consequence, the binding length in these simulations is defined as $z_b = 6$ nm. It is important to mention that the geometric complexes' radii as shown in Figure 6.2 do not equal their van der Waals radii. Analogously to the cyt c -cyt c interaction, the van der Waals minimum was chosen to be located at $x_{min} = d/2r = 0.1$ as defined already in subsection 2.2.3. Here, r denotes the complex radii. As a consequence, according to the geometric radius of the bc_1 complex $r_{bc_1, left} = r_{bc_1, right} = 2.5$ nm, the actual van der Waals radius is $r_{bc_1, left}^{vdW} = r_{bc_1, right}^{vdW} = 2.75$ nm. That is the reason why the small peak in Figure 6.3 is a bit farther away from the membrane than one would expect from the geometries in

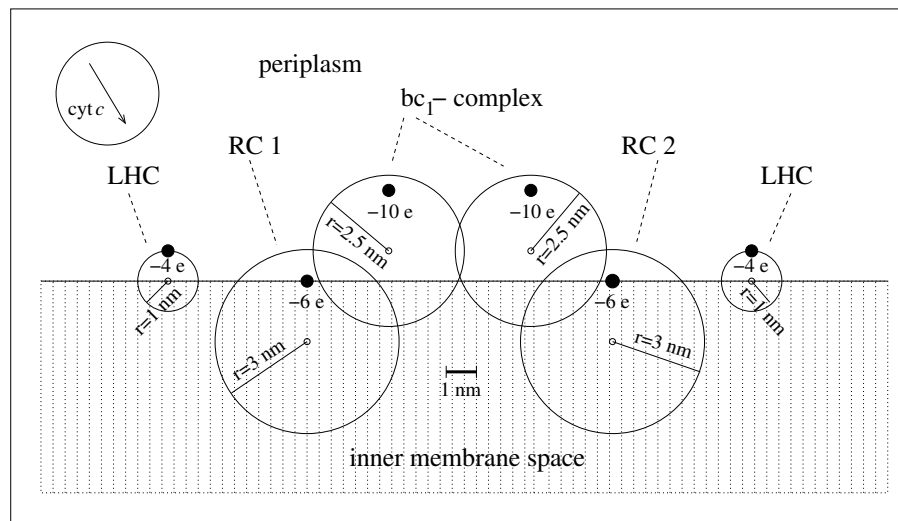


Figure 6.2: Side view of the geometries of the different model parts of one photosynthetic unit embedded into the membrane.

Figure 6.2. For the sake of completeness also effective binding isotherms are calculated like in section 5.4. These are depicted in Figure 6.4. Since there is no overall membrane surface charge, the amount of bound particles is smaller than in 5.6. The saturation effect does not become visible because the interface densities are too small.

The structure of the various membrane proteins should become visible in profiles parallel to the membrane. Figure 6.5 shows concentration plots for the same simulations as in Figure 6.3 and additionally for one higher density for model 3. It can be seen that the large extension of the model bc_1 complex into the periplasm prevents *cyt c* to enter the space in-between the two rings of the LHC in model 1 (upper left). Therefore, only the LHC ring is mapped on this plot approximately. In models 2 and 3 (upper right and lower left), however, the Brownian *cyt c* particles are able to pass through the free space in-between the two rings. The largest particle concentrations are to be found around the LHCs, in the space between the PUs and additional peaks can be seen between two RCs. The plot in the lower right panel equals the one in the lower left panel except that due to the higher particle interface density the free membrane space shows accordingly higher densities just like the PUs themselves. It should be noted that there is a slight asymmetry as can be seen from the peaks between the RCs. There are peaks at $(x, y) \simeq (23, 25)$ nm, $(x, y) \simeq (44, 25)$ nm, $(x, y) \simeq (20, 16)$ nm and $(x, y) \simeq (42, 16)$ nm. These should also to be found at $(x, y) \simeq (22, 22)$ nm,

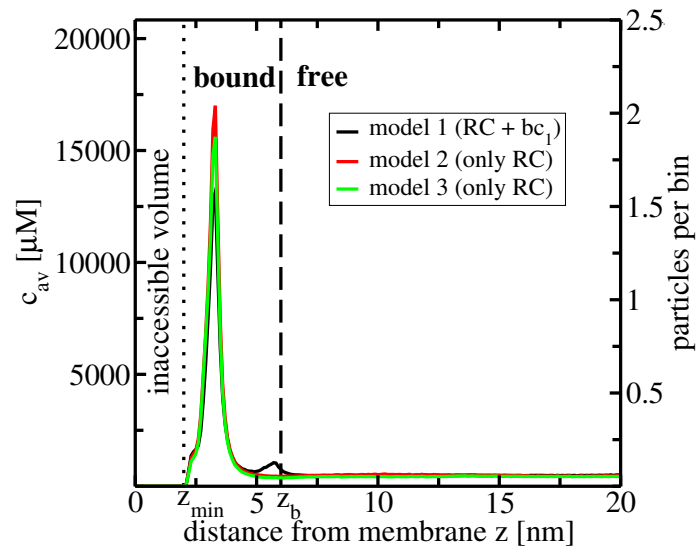


Figure 6.3: Comparison of concentration profiles between three different models including photosynthetic units for $c_0 = 600 \mu\text{M}$. The simulation box has dimensions $60 \times 40 \times 40 \text{ nm}^3$. c_{av} is the average concentration per bin. The values from $z = 20 \text{ nm}$ up to $z = 40 \text{ nm}$ are not shown here for the sake of clarity because the curve does not change between $z \simeq 6 \text{ nm}$ up to $z = 40 \text{ nm}$. A bin length of $\Delta z = 0.1 \text{ nm}$ was used which corresponds to a bin volume of $\Delta V = 60 \times 40 \times 0.1 \text{ nm}^3$.

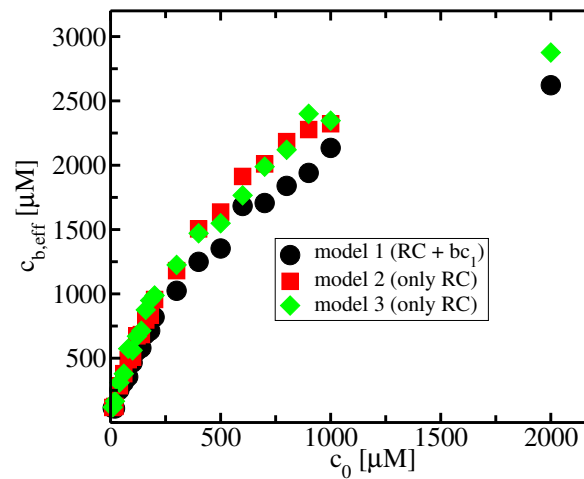


Figure 6.4: Comparison between effective binding isotherms for three different models including photosynthetic units. A binding length of $z_b = 6 \text{ nm}$ was used. After examining the profiles parallel to the membrane the box size was reduced by $2 \times 5 \text{ nm}$ in both directions and only particles in that volume were considered.

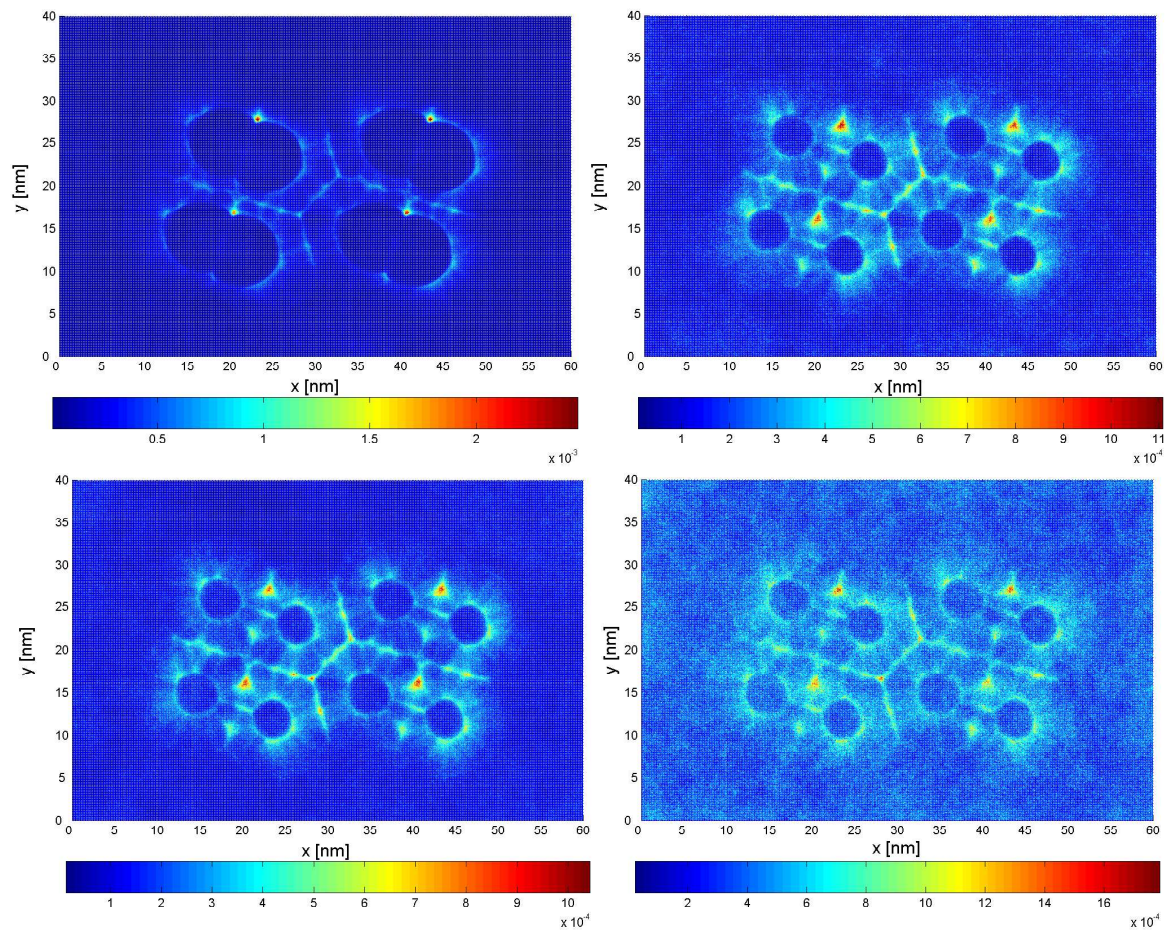


Figure 6.5: xy -concentration plots for simulations including photosynthetic units like in Figure 6.3. Upper left: model 1 for $c_0 = 600 \mu\text{M}$, upper right: model 2 for $c_0 = 600 \mu\text{M}$, lower left: model 3 for $c_0 = 600 \mu\text{M}$ and lower right: model 3 for $c_0 = 2000 \mu\text{M}$. The $c_0 = 600 \mu\text{M}$ profiles are computed from simulations of about $100 \mu\text{s}$ length. The $c_0 = 2000 \mu\text{M}$ profile is extracted from a simulation of only $30 \mu\text{s}$ length.

$(x, y) \simeq (42, 22)$ nm, $(x, y) \simeq (17, 10)$ nm and $(x, y) \simeq (38, 10)$ nm, but they are not there. The reason is that because of the high computational cost the simulations probably did not run long enough to sample the entire box volume and as a consequence certain areas might be spared by the particles. The number of particles against the simulation time is shown in Figure 6.6. An equilibrium is reached after $t \simeq 30 \mu\text{s}$ with an average of about 40 particles. But the large fluctuations and the trend of the curve towards the end of the simulation indicate that there might be oscillations in the particle number with a certain wavelength. The simulation was simply not long enough to cover many periods and therefore produced insufficient statistics.

A negative result is the fact that in none of these simulations there is a peak at the position of the RCs. Thus, *cyt c* does not get into contact with these and therefore is not able to perform an electron transfer. There are several possible reasons for these deviations. It might be that the charges and thus the electrostatic interactions are wrong. In our simulations, the electric field of the rings of LHCs probably prevents the particles to enter the space inside the ring and then to access the RC. Also the dimensions of the van der Waals spheres and the functional form of the van der Waals interaction might be incorrect. In other words, the model is probably not detailed enough. Interestingly, the fact that in the presented simulations there is almost no access to the RCs gives rise to the alternative idea that an additional PufX polypeptide inside the LHC rings could function as a gate for *cyt c* and as a consequence allows binding to the RCs. Figure 6.7 shows a hypothetical schematic representation of the components of the RC-LH1-PufX dimer as suggested in ref. [56]. But anyway, a more accurate model of the PUs is desirable. This line will be addressed by future projects in our group based on these preliminary results.

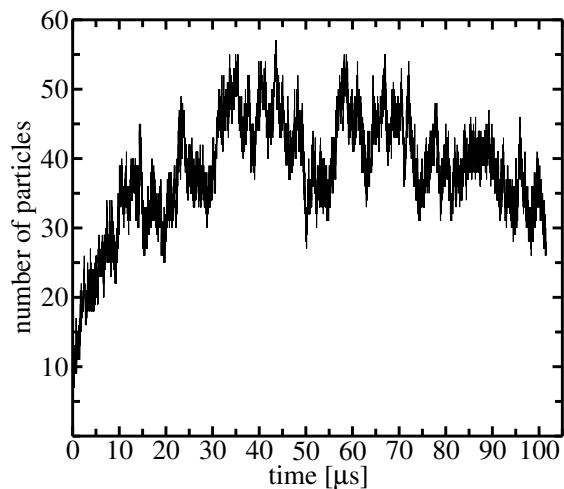


Figure 6.6: Plot of the total number of particles in model 1 for an interface density $c_0 = 600 \mu\text{M}$.



Figure 6.7: Representation of the RC-LH1-PufX dimer components in PufX^+ tubes as suggested in ref. [56]. The typical direction of the longitudinal tube axis relative to the unit cell is indicated by the arrow. The elliptical ring of LH1s is represented in green and the location of the PufX polypeptide is proposed by the red circle. The blue ellipse indicates the RCs. Yellow indicates the approximate location of the Q_B site and the Q_y transition dipoles of the special pair bacteriochlorophylls are shown in red. (from ref. [56]).

Chapter 7

Summary, conclusions and outlook

7.1 Summary and conclusions

Results were presented from Brownian dynamics simulations for cyt *c* molecules approximated as spherical particles with diameter $2R \simeq 3.3$ nm interacting with a charged planar membrane surface. Using the well-known Ermak-McCammon algorithm of ref. [36, 37] for solving the Langevin equations (see Chapter 2), a new computer program in C++ was developed. An overview of the way it is implemented is given in Chapter 3. The program in its current state is able to compute the trajectories (translation and rotation) of hundreds of spherical particles in systems with typical dimensions of $10^3 - 100^3$ nm³. As explained in the introductory Chapter 1 the motivation for studying the dynamics of cyt *c* molecules in such systems came from the progress in the research of photosynthetic bacteria, e.g. While the internal processes of energy transduction (light harvesting, channelling to RC, charge separation) are quite well understood, the dynamics of soluble cyt *c* as an electron transporter in this context is not yet clear. In many textbooks one can find illustrations where a single cyt *c* is responsible for the electron transport between two integral membrane proteins (the reaction centre RC and the bc_1 complex). But as pointed out in publications like refs. [49], [59], [60], [61] or [62] biological cells are crowded with different molecules. Consequently, one can assume that the electron transport between two integral membrane proteins is not simply taken on by one single cyt *c* molecule. Instead it is likely that many of these particles are located in a cyt *c* pool above the membrane and that they perform the electron transport in turns. Thus, it is desirable to have a simulation package that is able

to compute the trajectories of many proteins. Note that the detailed processes of electron transfer and binding to membrane proteins are not modelled here. The details of these processes are quite complicated so that we refrained from including them in the coarse-grained simulations. Here, the actual binding is simply defined by a particle distance z_b from the membrane which marks the beginning of the attractive potential.

The particles interact with each other and with the membrane via electrostatics and van der Waals forces. Both reflecting and 2-dimensional periodic boundary conditions can be applied. Also solvent mediated hydrodynamic interactions can be included. Actually, the limit in the amount of particles is mostly due to computational limits if these forces are included. The standard hydrodynamics is described by diffusion matrices and the computational costs for the necessary Cholesky decomposition (cf. section 3.2) scale at least cubically with the particle number.

The influence of standard hydrodynamics was tested:

As described in Chapter 4 the impact of hydrodynamic interaction using macroscopic formulations as the Oseen or Rotne-Prager tensor is difficult to understand and probably too inaccurate to yield useful results for complex molecules like proteins. Solvent mediated interactions between system walls (membranes) and particles should have an influence on the particles' motion as well. This is beyond the scope of this thesis. Because the focus of this work is on the dynamics of cyt *c* particles in quite large systems compared to typical systems in polymer science where periodic boundaries are essential, we believe that hydrodynamic interaction can be neglected as a first approximation. Consequently this is done in Chapters 5 and 6. To summarise, the simulations presented in Chapter 4 need to be considered as test cases (especially for hydrodynamic interaction) after the source code development had been finished. Apart from measuring diffusion coefficients, concentration profiles were determined in this chapter. E.g., the accumulation of the positively charged particles close to the membrane coincides with what one would expect for an attractive (negatively charged) surface.

CESIP allows to create equilibrated cyt *c* distributions in large boxes of $10^3 - 100^3 \text{ nm}^3$ dimensions up to milliseconds simulation time:

Having real biological systems in mind, a new kind of boundary conditions instead of periodic ones is favoured in subsequent simulations in Chapter 5. Besides the use of reflecting side walls a new particle insertion algorithm is utilised [35]. It allows to separate a simulation into regions where molecules can be considered as free Brownian particles and an interaction region. This region of “interest” is the actual simulation box. There the particles do not only interact with each other but also with the membrane surface and possible membrane proteins. The interface between these two regions is characterised by a fixed particle density. According to the insertion algorithm there is a flow out of and into the simulation box keeping the interface density constant. A big advantage is the existence of a particle bulk in the interface region. Also smaller boxes can be simulated because the box height (z -direction) is now adjustable easily. Using constant particle conditions and a reflecting boundary at the upper box wall, one needs to simulate in very high boxes (large z) in order to avoid a too disturbing influence of the reflections at that wall. To summarise, by using the new method it is easy to create equilibrated particle distributions above the membrane. Using these boundary conditions a step by step approach towards systems with membrane proteins was pursued. Binding of cyt *c* to membranes was investigated by Heimburg *et al.* experimentally [1]. Our simulations could reproduce the saturation effect qualitatively for a homogeneously charged but otherwise structureless membrane. Additional “binding sites” in form of additional point charges on the negatively charged membrane were the next step towards photosynthetic units in the previous chapter. These additional point charges have the effect that the effective space for binding to the surface is decreased. As a result, the saturation occurs for smaller interface densities than for a structureless membrane. Note that in contrast to the electrostatic interactions which are based on the dipolar sphere model and the Poisson-Boltzmann equation with quite realistic parameters, the van der Waals interaction is pretty arbitrary in this work. It is just assumed that typical van der Waals minima of about $-1 k_B T$ should exist at very close distances smaller than the particles’ radii. At least small variations in the van der Waals interactions between cyt *c* and the membrane surface were investigated and did not yield significant differences (cf. Figure 5.7).

A first step towards simulating multi-cyt *c* dynamics in photosynthesis, i.e., in the presence of photosynthetic units was undertaken:

In the previous Chapter 6 models for a photosynthetic unit on a membrane are presented. From additional membrane charges we proceed to membrane proteins in form of additional charges surrounded by van der Waals spheres. In this coarse-grained picture these spheres take the spatial extension of the participating membrane protein complexes like reaction centres (RCs), light harvesting complexes (LHC) and bc_1 complexes into account. Analysis of the cyt *c* trajectories showed that their average distribution is mostly along the ring of LHCs. No significant amount of cyt *c* can be found inside the ring and thus there is no association to the RCs. But in photosynthesis it is crucial that cyt *c* can get into close vicinity of a RC in order to deliver its electron. Consequently, the model of the photosynthetic units is too inaccurate. It might be that the charges of the LHCs are too strong and thus prevent cyt *c* from entering the ring. Another explanation which is discussed in the literature is the existence of the so-called PufX polypeptide at one position where we assumed a LHC. This polypeptide might work as a gate to the RC.

7.2 Outlook

Developing software for biological applications is a very challenging task. On the one hand one has to find a suitable model for the system to be investigated but on the other hand there are computational limits which have to be tackled. Very often this leads to the compromise of using coarse-grained models. The work presented here is based on such a software project. In its current state it can successfully be applied to systems where a coarse-grained modelling is possible. Nevertheless it is desirable to have more detailed knowledge of the interactions involved, especially the short-ranged van der Waals interactions and hydrodynamics for small particle-particle and particle-membrane distances. The non-physiological bound concentrations in the binding isotherms might be due to the inaccurate van der Waals forces between cyt *c* and the surface. At this point we want to emphasise the importance of the van der Waals interaction for short distances. Developing of more elaborate interactions, e.g., including hydrophobic effects will be necessary in future work based on the work presented in this thesis. The difficult task of including improved many-particle hydrodynamics into biological simulations is currently being worked on in our group by T. Geyer.

As to the electrostatic interaction between the Brownian particles it should be possible to increase the accuracy by applying the idea of effective charges. Using the program ECM (Effective Charges for Macromolecules in Solvent) it is possible to determine a point charge distribution of 10 – 30 effective charges from a molecule's PDB data base file [63]. These charges reproduce the molecule's electrostatic potential quite well. Consequently, the use of effective charges would give more accurate results. Although the current source code is already able to include any number of effective charges inside a spherical particle, the dipolar sphere model was favoured here due to its higher computational efficiency. However, in future work effective charges could be tested.

Particularly, the new interfacing (particle insertion) algorithm is a very promising feature. One can in principal create all sorts of (even curved) geometries as compositions of explicit Brownian dynamics regions and regions where it suffices to solve the diffusion equation on a grid.

As discussed, it is not possible to simulate details of molecule encounters with the model interactions used here. Therefore, it is desirable to have better energy functions for small distances, especially between a molecule and the membrane surface or a membrane protein. Then it would make sense, e.g., to consider the actual electron transfer between *cyt c*, the RC and the bc_1 complex by means of dynamically increasing and decreasing *cyt c*'s charge. From such simulations electron transfer rates could be derived and compared with experimental results. But how can one get these energy functions? One can select small parts of the large system, e.g., a membrane embedded bc_1 complex and model it in atomistic detail. Diffusion up to the distance of the so-called encounter complex (approximately 1 nm separation of surfaces) may be treated by Brownian dynamics simulations using atomistic details, as was done in D. Flöck's thesis [64, 65]. From this point onwards, molecular dynamics simulations of the binding event between *cyt c* and the membrane protein need to be performed. It should then be possible to extract information about the detailed interactions. This information can be used to adjust the parameters from the coarse-grained approach so that the results from these detailed simulations can approximately be reproduced. Similarly, future experimental results could be utilised to adjust the force fields. In any case, by improving the accuracy of the simulations, a tool will be available which can help to understand the dynamics in parts of big systems like photosynthetic bacteria.

Appendix A

System parameters

Tables A.1, A.2, A.3, A.4, A.5 and A.6 summarise the simulation parameters and assigns them to the data used for the various figures in this thesis. In all simulations the trajectories were written to the output file after 50 time steps each. PBC denotes 2-dimensional periodic boundary conditions as explained in subsection 2.3.2. In the case of PBC interparticle cutoffs of half the box width were used. For the van der Waals interaction with the membrane surface a cutoff of $z = 3$ nm (distance from the membrane) was used. RBC denotes reflecting boundary conditions together with particle insertion/deletion as explained in subsection 2.3.3. With RBC no cutoffs were used. Typically, simulation times of 0.1 ms could be reached. For small particle densities also milliseconds were possible.

	Figs. 4.1,4.3, Tabs. 3.1,3.2	Figs.4.2,4.4,4.5
general:		
particle insertion:	no	no
boundary conditions	PBC	PBC
time step Δt [ps]	10	10
membrane area [nm] \times [nm]	30×30	20×20
box length [nm]	30	20
Brownian particles:		
cyt c:		
hydrodynamic interaction	see fig.	see fig.
rotation	yes	yes
number part. or interf. concentration c_0	see fig.	see fig.
radius R [nm]	1.66	1.66
monopole charge q [e_0]	+7.25	+7.25
dipole moment p [e_0 nm]	5.2	5.2
dipole orient. w. r. to membrane:	—	—
$E_{min,vdW}^{cyt-cyt}$ [$k_B T$]	-0.91	-0.91
$r_{min,vdW}^{cyt-cyt}$ [nm]	3.652	3.652
vdW energy linearised for $r_{lin}^{cyt-cyt} <$	3.635	3.635
$E_{min,vdW}^{cyt-mem}$ [$k_B T$]	-1.0	-1.0
$r_{min,vdW}^{cyt-mem}$ [nm]	2.324	2.324
vdW energy linearised for $r_{lin}^{cyt-mem} <$	2.025	2.025
free diffusion coefficient D_0 [m^2/s]	1.477×10^{-10}	1.477×10^{-10}
dummy spheres (= cyt c except $q = p = 0$):		
number of dummies	—	—
solvent:		
temperature T [K]	298	298
viscosity η [kg/ms]	0.89×10^{-3}	0.89×10^{-3}
dielectric constant ϵ	78	78
ionic strength Na^+ , Cl^- [mM]	90	90
Debye length l_D [nm]	1.01	1.01
membrane:		
surface charge density σ [e_0/nm^2]	-1.3	-1.3

Table A.1: Parameters used for the simulations presented in Chapter 4.

	Fig. 4.6	Figs.4.7,4.9	Figs. 4.8,4.10,4.11
general:			
particle insertion:	no	no	no
boundary conditions	PBC	PBC	PBC
time step Δt [ps]	10	10	10
membrane area [nm]×[nm]	20 × 20	30 × 30	15 × 15
box length [nm]	20	30	15
Brownian particles:			
cyt c:			
hydrodynamic interaction	no	see fig.	see fig.
rotation	yes	yes	yes
number part. or interf. concentration c_0	16 particles	see fig.	see fig.
radius R [nm]	1.66	1.66	1.66
monopole charge q [e_0]	+7.25	+7.25	+7.25
dipole moment p [e_0 nm]	5.2	5.2	5.2
dipole orient. w. r. to membrane:	—	—	—
$E_{min,vdW}^{cyt-cyt}$ [$k_B T$]	-0.91	-0.91	-0.91
$r_{min,vdW}^{cyt-cyt}$ [nm]	3.652	3.652	3.652
vdW energy linearised for $r_{lin}^{cyt-cyt} <$	3.635	3.635	3.635
$E_{min,vdW}^{cyt-mem}$ [$k_B T$]	-1.0	-1.0	-1.0
$r_{min,vdW}^{cyt-mem}$ [nm]	2.324	2.324	2.324
vdW energy linearised for $r_{lin}^{cyt-mem} <$	2.025	2.025	2.025
free diffusion coefficient D_0 [m^2/s]	1.477×10^{-10}	1.477×10^{-10}	1.477×10^{-10}
dummy spheres (= cyt c except $q = p = 0$):			
number of dummies	—	20	20
solvent:			
temperature T [K]	298	298	298
viscosity η [kg/ms]	0.89×10^{-3}	0.89×10^{-3}	0.89×10^{-3}
dielectric constant ϵ	78	78	78
ionic strength Na^+, Cl^- [mM]	90	90	90
Debye length l_D [nm]	1.01	1.01	1.01
membrane:			
surface charge density σ [e_0/nm^2]	see fig.	-1.3	-1.3

Table A.2: Parameters used for the simulations presented in Chapter 4.

	Fig.5.1	Fig.5.2	Figs. 5.3,5.6
general:			
particle insertion:	yes	see fig	yes
boundary conditions	RBC	RBC	RBC
time step Δt [ps]	10	10	10
membrane area [nm] \times [nm]	30 \times 30	20 \times 20	see fig.
box length [nm]	20	20	see fig.
Brownian particles:			
cyt c:			
hydrodynamic interaction	no	no	no
rotation	no	no	no
number part. or interf. concentration c_0	7500 μM	3000 μM	see fig.
radius R [nm]	1.66	1.66	1.66
monopole charge q [e_0]	+7.25	+7.25	+7.25
dipole moment p [e_0 nm]	5.2	5.2	5.2
dipole orient. w. r. to membrane:	— \rightarrow +	— \rightarrow +	— \rightarrow +
$E_{min,vdW}^{cyt-cyt}$ [$k_B T$]	-1.0	-1.0	-1.0
$r_{min,vdW}^{cyt-cyt}$ [nm]	3.652	3.652	3.652
vdW energy linearised for $r_{lin}^{cyt-cyt} <$	3.635	3.635	3.635
$E_{min,vdW}^{cyt-mem}$ [$k_B T$]	-1.0	-1.0	-1.0
$r_{min,vdW}^{cyt-mem}$ [nm]	2.324	2.324	2.324
vdW energy linearised for $r_{lin}^{cyt-mem} <$	2.025	2.025	2.025
free diffusion coefficient D_0 [m^2/s]	1.477×10^{-10}	1.477×10^{-10}	1.477×10^{-10}
dummy spheres (= cyt c except $q = p = 0$):			
number of dummies	—	—	—
solvent:			
temperature T [K]	298	298	298
viscosity η [kg/ms]	0.89×10^{-3}	0.89×10^{-3}	0.89×10^{-3}
dielectric constant ϵ	78	78	78
ionic strength Na^+, Cl^- [mM]	90	90	90
Debye length l_D [nm]	1.01	1.01	1.01
membrane:			
surface charge density σ [e_0/nm^2]	-1.3	-1.3	-1.3

Table A.3: Parameters used for the simulations presented in Chapter 5.

	Figs. 5.4, 5.5	Fig. 5.7	Fig. 5.8
general:			
particle insertion:	yes	yes	yes
boundary conditions	RBC	RBC	RBC
time step Δt [ps]	10	10	10
membrane area [nm]×[nm]	30 × 30	30 × 30	30 × 30
box length [nm]	20	20	20
Brownian particles:			
cyt c:			
hydrodynamic interaction	no	no	no
rotation	no	no	no
number part. or interf. concentration c_0	see fig.	see fig.	see fig.
radius R [nm]	1.66	1.66	1.66
monopole charge q [e_0]	+7.25	+7.25	+7.25
dipole moment p [e_0 nm]	5.2	5.2	5.2
dipole orient. w. r. to membrane:	− → +	− → +	− → +
$E_{min,vdW}^{cyt-cyt}$ [$k_B T$]	-1.0	-1.0	-1.0
$r_{min,vdW}^{cyt-cyt}$ [nm]	3.652	3.652	3.652
vdW energy linearised for $r_{lin}^{cyt-cyt} <$	3.635	3.635	3.635
$E_{min,vdW}^{cyt-mem}$ [$k_B T$]	-1.0	see fig.	-1.0
$r_{min,vdW}^{cyt-mem}$ [nm]	2.324	2.324	2.324
vdW energy linearised for $r_{lin}^{cyt-mem} <$	2.025	2.025	2.025
free diffusion coefficient D_0 [m^2/s]	1.477×10^{-10}	1.477×10^{-10}	1.477×10^{-10}
dummy spheres (= cyt c except $q = p = 0$):			
number of dummies	—	—	—
solvent:			
temperature T [K]	298	298	298
viscosity η [kg/ms]	0.89×10^{-3}	0.89×10^{-3}	0.89×10^{-3}
dielectric constant ϵ	78	78	78
ionic strength Na^+, Cl^- [mM]	90	90	90
Debye length l_D [nm]	1.01	1.01	1.01
membrane:			
surface charge density σ [e_0/nm^2]	-1.3	-1.3	see fig.

Table A.4: Parameters used for the simulations presented in Chapter 5.

	Fig. 5.9	Fig. 5.10	Figs. 5.11, 5.12
general:			
particle insertion:	yes	see fig.	yes
boundary conditions	RBC	see fig.	RBC
time step Δt [ps]	10	10	10
membrane area [nm] \times [nm]	30 \times 30	20 \times 20/30 \times 30	30 \times 30
box length [nm]	20	20	20
Brownian particles:			
cyt c:			
hydrodynamic interaction	no	no	no
rotation	see fig.	yes	no
number part. or interf. concentration c_0	see fig.	4000 μ M	see fig.
radius R [nm]	1.66	1.66	1.66
monopole charge q [e_0]	+7.25	+7.25	+7.25
dipole moment p [e_0 nm]	5.2	5.2	5.2
dipole orient. w. r. to membrane:	see fig.	—	— \rightarrow +
$E_{min,vdW}^{cyt-cyt}$ [$k_B T$]	-1.0	-0.91/-1.0	-1.0
$r_{min,vdW}^{cyt-cyt}$ [nm]	3.652	3.652	3.652
vdW energy linearised for $r_{lin}^{cyt-cyt} <$	3.635	3.653	3.635
$E_{min,vdW}^{cyt-mem}$ [$k_B T$]	-1.0	-1.0	-1.0
$r_{min,vdW}^{cyt-mem}$ [nm]	2.324	2.324	2.324
vdW energy linearised for $r_{lin}^{cyt-mem} <$	2.025	2.025	2.025
free diffusion coefficient D_0 [m^2/s]	1.477×10^{-10}	1.477×10^{-10}	1.477×10^{-10}
dummy spheres (= cyt c except $q = p = 0$):			
number of dummies	—	—	—
solvent:			
temperature T [K]	298	298	298
viscosity η [kg/ms]	0.89×10^{-3}	0.89×10^{-3}	0.89×10^{-3}
dielectric constant ϵ	78	78	78
ionic strength Na ⁺ , Cl ⁻ [mM]	90	90	90
Debye length l_D [nm]	1.01	1.01	1.01
membrane:			
surface charge density σ [e_0/nm^2]	-0.52	-0.52/-1.3	-1.3
additional membrane charges	—	—	yes (see fig.)

Table A.5: Parameters used for the simulations presented in Chapter 5.

	Figs. 6.3,6.4, 6.5, 6.6
general:	
particle insertion:	yes
boundary conditions	RBC
time step Δt [ps]	10
membrane area [nm] \times [nm]	60×40
box length [nm]	40
Brownian particles:	
cyt c:	
hydrodynamic interaction	no
rotation	yes
number part. or interf. concentration c_0	see fig.
radius R [nm]	1.66
monopole charge q [e_0]	+7.25
dipole moment p [e_0 nm]	5.2
dipole orient. w. r. to membrane:	—
$E_{min,vdW}^{cyt-cyt}$ [$k_B T$]	-1.0
$r_{min,vdW}^{cyt-cyt}$ [nm]	3.652
vdW energy linearised for $r_{lin}^{cyt-cyt} <$	3.635
$E_{min,vdW}^{cyt-mem}$ [$k_B T$]	-1.0
$r_{min,vdW}^{cyt-mem}$ [nm]	2.324
vdW energy linearised for $r_{lin}^{cyt-mem} <$	2.025
free diffusion coefficient D_0 [m^2/s]	1.477×10^{-10}
dummy spheres (= cyt c except $q = p = 0$):	
number of dummies	—
solvent:	
temperature T [K]	298
viscosity η [kg/ms]	0.89×10^{-3}
dielectric constant ϵ	78
ionic strength Na^+, Cl^- [mM]	90
Debye length l_D [nm]	1.01
membrane:	
surface charge density σ [e_0/nm^2]	0.0
additional membrane proteins	see figures and text

Table A.6: Parameters used for the simulations presented in Chapter 6.

Appendix B

Input files

A typical input file (called “simulation_parameters”) for the Brownian dynamics package CESIP is shown in Tables B.1 and B.2. Additionally, there are two input files for compiling the program. One is the file “OUTPUTFLAGS” where the compiler finds information about the output format to be used. Another file called “COMPUTATIONFLAGS” contains compiler flags which determine whether the compiler creates an executable using, e.g., reflecting boundaries, the insertion algorithm, rotation or hydrodynamics.

Number of input parameters (lines -1):	number_input	= 55
Number of steps:	number_steps	= 10000000
Time step [ns]:	delta_t	= 0.01
Write data after every write_steps step:	write_steps	= 50
Temperature [K]:	T	= 298
Fluid viscosity [kg/(m*s)]:	eta	= 0.89e-03
Dielectric constant of fluid:	epsilon	= 78
Debye length [A]:	debye_length	= 10.1
Simulation box side length xy [A]:	box_length_xy	= 300
Simulation box side length z [A]:	box_length_z	= 200
Charge density of membrane surface [e0/A**2]:	charge_density	= -0.013
Number of additional membrane units:	number_units	= 5
Radius of membrane units [A]:	unit_radius	= 15.0
Mass of a membrane unit [kD]:	unit_mass	= 5988.02
Distance of neighbouring membrane units [A]:	unit_distance	= 60.0
Electrostatic cutoff membrane units [box_length_xy]:	el_cutoff_units	= 3.0
Lennard-Jones cutoff membrane units [box_length_xy]:	lj_cutoff_units	= 3.0
Density at upper box wall [mu mol]:	rho_0	= 2100.0
Number of different particle groups in solvent:	number_groups	= 1
Maximum number of particles in solvent:	max_number_movers	= 600
Depth for adding particles [a_0]:	z_test	= 100.0
Number of main moving particles:	number_main_movers	= 1
Radius of main particles [A]:	radius_main_movers	= 16.6
Mass of a main moving particles [kD]:	mass_main_movers	= 12.5
Displacement according to repulsion from walls [radius_particle]:	inf_disp	= 0.045
Electrostatic cutoff movers [box_length_xy]:	el_cutoff_movers	= 3.0
Hydrodynamic cutoff movers [box_length_xy]:	hy_cutoff_movers	= 3.0
Lennard-Jones cutoff movers [box_length_xy]:	lj_cutoff_movers	= 0.1
Lennard-Jones cutoff mover-membrane [box_length_z]:	lj_cutoff_mover_surface	= 0.1
LJ repulsion cutoff mover-mover [distance/(2*radius_movers)]:	LJ_rep_cutoff_mover_mover	= 0.095
LJ repulsion cutoff mover-membrane [distance/(2*radius_movers)]:	LJ_rep_cutoff_mover_surface	= 0.11
LJ repulsion cutoff mover-membrane unit [distance/(2*radius_movers)]:	LJ_rep_cutoff_mover_membrane_unit	= 0.095

Table B.1: Input file for one simulation from Figure 5.12 ($c_0 = 2100 \mu\text{M}$).

```

Dispersive LJ parameter of membrane:          parm_disp_mem    = 1.49e-10
Repulsive LJ parameter of membrane:          parm_rep_mem     = 1.32e-36
Dispersive LJ parameter of membrane units:   parm_disp_mem_prot = 0.0
Repulsive LJ parameter of membrane units:   parm_rep_mem_prot = 0.0
Dispersive LJ parameter of movers:          parm_disp_mov_prot = 1.88e-10
Repulsive LJ parameter of movers:          parm_rep_mov_prot = 4.02e-38
Number of charges in a membrane unit:       number_unit_charges = 1
    charge 0 [e0] = -6.0
        its x coordinate in cms-frame [A] = 0
        its y coordinate in cms-frame [A] = 0
        its z coordinate in cms-frame [A] = 0
Number of charges in a moving particle:      number_mover_charges = 3
    charge 0 [e0] = +7.25
        its x coordinate in cms-frame [A] = 0
        its y coordinate in cms-frame [A] = 0
        its z coordinate in cms-frame [A] = 0
    charge 1 [e0] = +1.725
        its x coordinate in cms-frame [A] = 15.1
        its y coordinate in cms-frame [A] = 0
        its z coordinate in cms-frame [A] = 0
    charge 2 [e0] = -1.725
        its x coordinate in cms-frame [A] = -15.1
        its y coordinate in cms-frame [A] = 0
        its z coordinate in cms-frame [A] = 0

```

Table B.2: Input file for one simulation from Figure 5.12 ($c_0 = 2100 \mu\text{M}$) continued.

Appendix C

Output files

Part of the output for a particle trajectory is shown in Figure C.1. The corresponding output for particle charges is shown in Figure C.2. Since charges are fixed with respect to a particle's centre of mass, the total charge positions include information about the overall rotation of a particle. The coordinates from these two files are then used for further analysis like the computation of the presented concentration profiles. For that purpose several scripts written in Perl are available in CESIP.

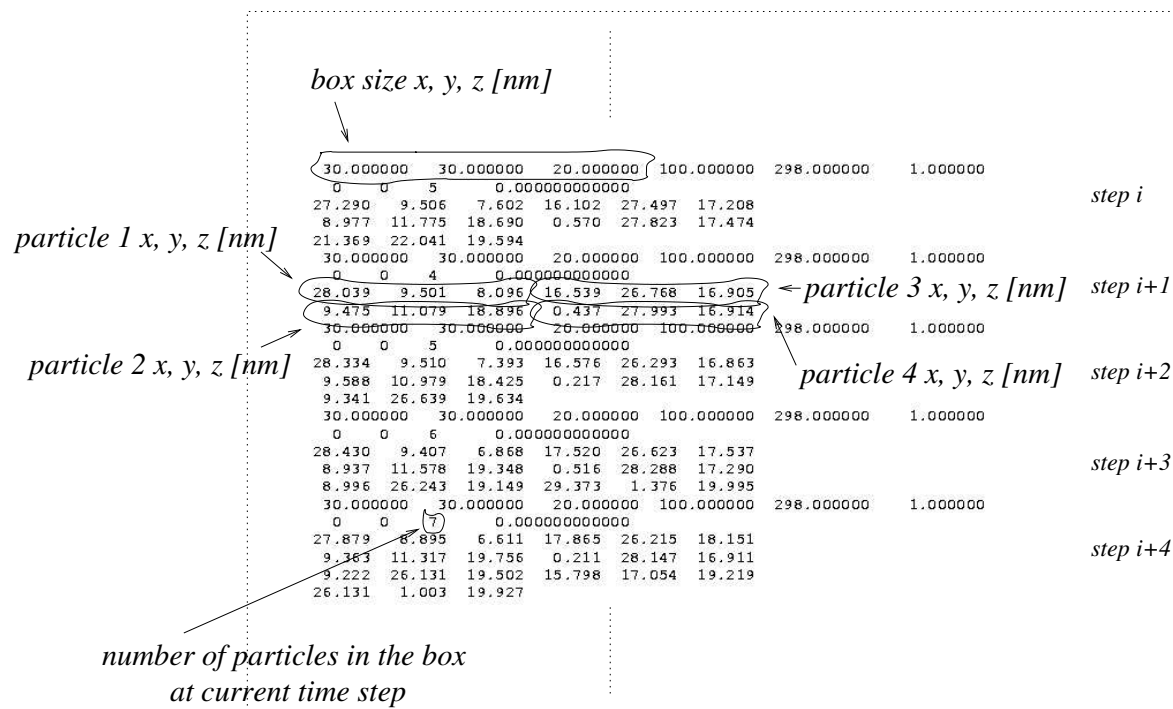


Figure C.1: Part of a particle trajectory. All coordinates are chosen with respect to the origin of the simulation box.

```

30.000000 30.000000 20.000000 100.000000 298.000000 1.000000
0 0 15 0.0000000000000000
27.290 9.506 7.602 26.109 8.567 7.656
28.472 10.445 7.549 16.102 27.497 17.208
15.232 26.267 17.320 16.972 28.726 17.097
8.977 11.775 18.690 8.548 11.659 20.133
9.406 11.891 17.247 0.570 27.823 17.474
-0.068 26.455 17.458 1.208 29.192 17.490
21.369 22.041 19.594 20.363 21.272 18.772
22.375 22.810 20.417
30.000000 30.000000 20.000000 100.000000 298.000000 1.000000
0 0 12 0.0000000000000000
28.039 9.501 8.096 26.806 8.661 8.329
29.272 10.340 7.863 16.539 26.768 16.905
15.793 25.463 16.757 17.286 28.072 17.053
9.475 11.079 18.896 8.812 11.073 20.253
10.138 11.085 17.540 0.437 27.993 16.914
-0.077 26.591 17.139 0.951 29.394 16.688
30.000000 30.000000 20.000000 100.000000 298.000000 1.000000
0 0 15 0.0000000000000000
28.334 9.510 7.393 27.017 8.942 7.866
29.651 10.078 6.920 16.576 26.293 16.863
16.047 24.879 16.869 17.104 27.708 16.858
9.588 10.979 18.425 8.890 11.373 19.704
10.287 10.585 17.145 0.217 28.161 17.149
-0.260 26.857 17.741 0.694 29.466 16.557
9.341 26.639 19.634 7.934 26.186 19.940
10.748 27.093 19.327
30.000000 30.000000 20.000000 100.000000 298.000000 1.000000
0 0 18 0.0000000000000000
28.430 9.407 6.868 27.174 8.573 6.955
29.685 10.241 6.782 17.520 26.623 17.537
16.838 25.337 17.940 18.202 27.908 17.134
8.937 11.578 19.348 8.301 11.906 20.678
9.572 11.251 18.018 0.516 28.288 17.290
0.051 27.097 18.093 0.981 29.480 16.487
8.996 26.243 19.149 7.509 25.982 19.117
10.483 26.504 19.181 29.373 1.376 19.995
28.118 0.542 20.081 30.629 2.211 19.909
30.000000 30.000000 20.000000 100.000000 298.000000 1.000000
0 0 21 0.0000000000000000
27.879 8.895 6.611 26.437 8.447 6.599
29.320 9.344 6.624 17.865 26.215 18.151
17.243 24.851 18.332 18.486 27.580 17.970
9.363 11.317 19.756 8.891 11.273 21.190
9.836 11.362 18.323 0.211 28.147 16.911
-0.425 26.936 17.551 0.847 29.357 16.271
9.222 26.131 19.502 7.747 26.303 19.777
10.697 25.958 19.228 15.798 17.054 19.219
14.536 16.239 19.070 17.060 17.870 19.367
26.131 1.003 19.927 24.698 0.554 19.770
27.564 1.452 20.083

```

Figure C.2: Part of the output for all particle charges corresponding to the output in Figure C.1. The numbers have the same meaning and units like in Figure C.1 except that there are 3 charges per particle. The corresponding order of coordinates is: particle 1 (charge 1 (x, y, z), charge 2 (x, y, z), charge 3 (x, y, z)), particle 2 (charge 1 (x, y, z), charge 2 (x, y, z), charge 3 (x, y, z)), etc.

Bibliography

- [1] T. Heimburg, B. Angerstein, and D. Marsh. Binding of Peripheral Proteins to Mixed Lipid Membranes: Effect of Lipid Demixing upon Binding. *Biophys. J.*, 76:2575, 1999.
- [2] M.P. Allen and D.J. Tildesley. *Computer Simulation of Liquids*. Oxford University Press, Oxford, 1987.
- [3] R. Brown. A Brief Account of Microscopical Observations Made in the Months of June, July and August 1827 on the Particles Contained in the Pollen of Plants; and on the General Existence of Active Molecules in Organic and Inorganic Bodies. London: Taylor, July 30, 1828. Not published. Like many wealthy scientists of his day, Brown had his results published privately and distributed to friends, colleagues, and the press.
- [4] J.K.G. Dhont. *An Introduction to Dynamics of Colloids*. Elsevier Science, Amsterdam, 1996.
- [5] J. Toon. Is Brownian Motion The Secret Of Life After All? *Daily University Science News*, page <http://unisci.com/stories/20012/0607011.htm>, 2001.
- [6] R.F. Fox and M.H. Choi. Rectified Brownian motion and kinesin motion along microtubules. *Phys. Rev. E.*, 63 (5): Art. No. 051901 Part 1, 2001.
- [7] A. Borodich, I. Rojdestvenski, and M. Cottam. Lateral heterogeneity of photosystems in thylakoid membranes studied by Brownian dynamics simulations. *Biophys. J.*, 85:774, 2003.
- [8] L. Stryer. *Biochemie*. Spektrum-der-Wissenschaft, Heidelberg, 1990.
- [9] Karp G. *Cell and Molecular Biology*. John Wiley, New York, 2002.

- [10] G.L. Zubay. *Biochemie*. McGraw-Hill, London, 2000.
- [11] A.W. Roszak, T.D. Howard, J. Southall, A.T. Gardiner, C.J. Law, N.W. Isaacs, and R.J. Cogdell. Crystal Structure of the RC-LHI Core Complex from *Rhodospseudomonas palustris*. *Science*, 302:1969, 2003.
- [12] C. Jungas, J.L. Ranck, J.L. Rigaud, P. Joliot, and A. Verméglio. Supramolecular organization of the photosynthetic apparatus of *Rhodobacter sphaeroides*. *Embo J.*, 18:534, 1999.
- [13] U. Ermler, G. Fritsch, and H. Michel. Structure of the photosynthetic reaction centre from *Rhodobacter sphaeroides* at 2.65 Å resolution: cofactors and protein-cofactor interactions. *Structure*, 2:925, 1994.
- [14] S. Karrasch, P.A. Bullough, and R. Ghosh. The 8.5 Å projection map of the light-harvesting complex I from *Rhodospirillum rubrum* reveals a ring composed of 16 subunits. *Embo J.*, 14:631, 1995.
- [15] G.W. Bushnell, G.V. Louie, and G.D. Brayer. High-resolution three-dimensional structure of horse heart cytochrome *c*. *J. Mol. Biol.*, 214:585, 1990.
- [16] W.H. Koppenol and E. Margoliash. The Asymmetric Distribution of Charges on the Surface of Horse Cytochrome *c*. *J. Biol. Chem.*, 257:4426, 1982.
- [17] L.D. Eltis, R.G. Herbert, P.D. Barker, A.G. Mauk, and S.H. Northrup. Reduction of Horse Heart Ferricytochrome *c* by Bovine Liver Ferrocycytochrome *b5*. Experimental and Theoretical Analysis. *Biochemistry*, 30:3663, 1991.
- [18] J.F. Nagle and S. Tristram-Nagle. Structure of lipid bilayers. *Biochim. Biophys. Acta-Rev. Biomembr.*, 1469:159, 2000.
- [19] M. Subramanian, A. Jutila, and P.K.J. Kinnunen. Binding and dissociation of cytochrome *c* to and from membranes containing acidic phospholipids. *Biochemistry*, 37:1394, 1998.
- [20] J. Hochman, S. Ferguson-Miller, and M. Schindler. Mobility in the mitochondrial electron transport chain. *Biochemistry*, 24:2509, 1985.

- [21] J.M. Thijssen. *Computational Physics*. Cambridge University Press, Cambridge, 1999.
- [22] D. Frenkel and B. Smit. *Understanding Molecular Simulation: From Algorithms to Applications*. Academic Press, San Diego, 1996.
- [23] M. Karplus and McCammon J.A. Molecular dynamics simulations of biomolecules. *Nat. Struct. Biol.*, 9:646, 2002.
- [24] C.M. Soares, V.H. Teixeira, and A.M. Baptista. Protein structure and dynamics in nonaqueous solvents: Insights from molecular dynamics simulation studies. *Biophys. J.*, 84:1628, 2003.
- [25] I. Daidone, A. Amadei, D. Roccatano, and A. Di Nola. Molecular dynamics simulation of protein folding by essential dynamics sampling: Folding landscape of horse heart cytochrome *c*. *Biophys. J.*, 85:2865, 2003.
- [26] T. Castrignano, G. Chillemi, G. Varani, and A. Desideri. Molecular dynamics simulation of the RNA complex of a double-stranded RNA-binding domain reveals dynamic features of the intermolecular interface and its hydration. *Biophys. J.*, 83:3542, 2002.
- [27] K.Y. Chan, Y.W.A. Tang, and I. Szalai. Ion transport in simple nanopores. *Mol. Simul.*, 30:81, 2004.
- [28] C.F. Wong and J.A. McCammon. Protein simulation and drug design. *Adv. Protein Chem.*, 66:87, 2003.
- [29] M. Zloh, D. Esposito, and W.A. Gibbons. Helical net plots and lipid favourable surface mapping of transmembrane helices of integral membrane proteins: Aids to structure determination of integral membrane proteins. *Internet J. Chem.*, 6, 2003.
- [30] S.H. Northrup. *Cytochrome c: A Multidisciplinary Approach*, chapter 16, page 543. University Science Books, Herndon, 1996.
- [31] J.D. Madura, J.M. Briggs, R.C. Wade, M.E. Davis, B.A. Luty, A. Ilin, J. Antosiewicz, M.K. Gilson, B. Bagheri, L.R. Scott, and J.A. McCammon. Electrostatics and diffusion of molecules in solution - simulations with the University-of-Houston Brownian dynamics program. *Comp. Phys. Commun.*, 91:57, 1995.

-
- [32] R.R. Gabdoulline and R.C. Wade. Protein-protein association: Investigation of factors influencing association rates by Brownian dynamics simulations. *J. Mol. Biol.*, 306:1139, 2001.
- [33] R.R. Gabdoulline and R.C. Wade. Simulation of the diffusional association of Barnase and Barstar. *Biophys. J.*, 72:1917, 1997.
- [34] C. Gorba and V. Helms. Diffusional dynamics of cytochrome *c* molecules in the presence of a charged surface. *Soft Mater.*, 1:187, 2003.
- [35] T. Geyer, C. Gorba, and V. Helms. Interfacing Brownian dynamics simulations. *J. Chem. Phys.*, 120:4573, 2004.
- [36] E. Dickinson, S.A. Allison, and J.A. McCammon. Brownian Dynamics with Rotation-Translation Coupling. *J. Chem. Soc. Farad. Trans. 2*, 81:591, 1985.
- [37] D.L. Ermak and J.A. McCammon. Brownian dynamics with hydrodynamic interactions. *J. Chem. Phys.*, 69:1352, 1978.
- [38] P. Mazur and W. van Saarloos. Many-sphere hydrodynamic interactions and mobilities in a suspension. *Physica A*, 115:21, 1982.
- [39] P. Ahlrichs and B. Dünweg. Simulation of a single polymer chain in solution by combining lattice Boltzmann and molecular dynamics. *J. Chem. Phys.*, 111:8225, 1999.
- [40] E.J.W. Verwey and J.TH.G. Overbeek. *Theory of the Stability of Lyophobic Colloids*. Elsevier, New York, 1948.
- [41] H.C. Hamaker. The London-van der Waals attraction between spherical particles. *Physica IV*, 10:1058, 1937.
- [42] D.J. Bicout and M.J. Field. Stochastic dynamics simulations of macromolecular diffusion in a model of the cytoplasm of *Escherichia coli*. *J. Phys. Chem.*, 100:2489, 1996.
- [43] G. Booch, J. Rumbaugh, and I. Jacobsen. *The Unified Modeling Language User Guide*. Addison-Wesley, 1999.

- [44] M. Fowler and K. Scott. *UML Distilled: A Brief Guide to the Standard Object Modeling Language*. Addison-Wesley, 2000.
- [45] W.H. Press, S.A. Teukolsky, and W.T. Vetterling. *Numerical Recipes in C*. Cambridge University Press, Cambridge, 1993.
- [46] C.W.J. Beenakker. Ewald sum of the Rotne-Prager tensor. *J. Chem. Phys.*, 85:1581, 1986.
- [47] D.M. Heyes. Mean-field-hydrodynamics Brownian dynamics simulations of viscosity and self-diffusion of near-hard-sphere colloidal liquids. *J. Phys.-Condens. Matter*, 7:8857, 1995.
- [48] D.M. Heyes and P.J. Mitchell. Mean-field hydrodynamics Brownian dynamics simulations of stabilized colloidal liquids under shear. *J. Non-Newton. Fluid Mech.*, 68:101, 1997.
- [49] R.J. Ellis. Macromolecular crowding: an important but neglected aspect of the intracellular environment. *Curr. Opin. Struct. Biol.*, 11:114, 2001.
- [50] C. Gorba, T. Geyer, and V. Helms. Brownian dynamics simulations of simplified cytochrome *c* molecules in the presence of a charged surface. *J. Chem. Phys.*, 121:457, 2004.
- [51] W. Kühlbrandt, D.N. Wang, and Y. Fujiyoshi. Atomic model of plant light-harvesting complex by electron crystallography. *Nature*, 367:614, 1994.
- [52] D.N. Wang, Y. Fujiyoshi, and W. Kühlbrandt. An atomic model of plant light-harvesting complex by electron crystallography. *Biophys. J.*, 66:A2–A2 Part 2, 1994.
- [53] A. Stamouli, S. Kafi, D.C.G. Klein, T.H. Oosterkamp, W.M. Frenken, R.J. Cogdell, and T.J. Aartsma. The Ring Structure and Organization of Light Harvesting 2 Complexes in a Reconstituted Lipid Bilayer, Resolved by Atomic Force Microscopy. *Biophys. J.*, 84:2483, 2003.
- [54] J. Koepke, X.C. Hu, C. Muenke, K. Schulten, and H. Michel. The crystal structure of the light-harvesting complex II (B800-850) from *Rhodospirillum rubrum*. *Structure*, 4:581, 1996.

- [55] C. Lange and C. Hunte. Crystal structure of the yeast cytochrome bc_1 complex with its bound substrate cytochrome c . *Proc. Natl. Acad. Sci. U.S.A.*, 99:2800, 2002.
- [56] C.A. Siebert, P. Qian, D. Fotiadis, A. Engel, C.N. Hunter, and P.A. Bullough. Molecular architecture of photosynthetic membranes in *Rhodobacter sphaeroides*: the role of PufX. *Embo J.*, 23:690, 2004.
- [57] R.J. Cogdell, P.K. Fyfe, S.J. Barrett, S.M. Prince, A.A. Freer, N.W. Isaacs, P. McGlynn, and C.N. Hunter. The purple bacterial photosynthetic unit. *Photosynth. Res.*, 48:55, 1996.
- [58] R.N. Frese, J.D. Olsen, R. Branvall, W.H.J. Westerhuis, C.N. Hunter, and R. van Grondelle. The long-range supraorganization of the bacterial photosynthetic unit: A key role for PufX. *Proc. Natl. Acad. Sci. U.S.A.*, 97:5197, 2000.
- [59] G.L. Lukacs, P. Haggie, O. Seksek, D. Lechardeur, N. Freedman, and A.S. Verkman. Size-dependent DNA mobility in cytoplasm and nucleus. *J. Biol. Chem.*, 275:1625, 2000.
- [60] C.N. Patel, S.M. Noble, G.T. Weatherly, A. Tripathy, D.J. Winzor, and G.J. Pielak. Effects of molecular crowding by saccharides on alpha-chymotrypsin dimerization. *Protein Sci.*, 11:997, 2002.
- [61] D.F. Gomez-Casati, S. Cortassa, M.A. Aon, and A.A. Iglesias. Ultrasensitive behavior in the synthesis of storage polysaccharides in cyanobacteria. *Planta*, 216:969, 2003.
- [62] J. Ovadi and V. Saks. On the origin of intracellular compartmentation and organized metabolic systems. *Mol. Cell. Biochem.*, 256:5, 2004.
- [63] R.R. Gabdouliline and R.C. Wade. Effective Charges for Macromolecules in Solvent. *J. Phys. Chem.*, 100:3868, 1996.
- [64] D. Flöck. *Protein-Protein Docking and Brownian Dynamics Simulation of Electron Transfer Proteins*. PhD thesis, Johann Wolfgang Goethe - Universität Frankfurt am Main, Fachbereich Physik, Frankfurt, Germany, Okt. 2003.
- [65] D. Flöck. A Brownian Dynamics Study: The Effect of a Membrane Environment on an Electron Transfer System. *Biophys. J.*, 87:65, 2004.

Danksagung

Mein ganz besonderer Dank gilt Prof. V. Helms für die freundliche Aufnahme in die ehemalige Nachwuchsgruppe „theoretische Biophysik“ des Max-Planck-Instituts für Biophysik in Frankfurt und die Möglichkeit, die Arbeit an der Universität des Saarlandes fortzuführen und abzuschließen. Insbesondere danke ich für die intensive Betreuung dieser Arbeit und die Bereitschaft, auftretende Fragen und Probleme jederzeit zu diskutieren.

Ganz herzlich danken möchte ich auch Prof. W. Mäntele für die Betreuung der Arbeit an der Johann-Wolfgang-Goethe-Universität in Frankfurt.

Weiterhin danke ich den Mitgliedern der Arbeitsgruppe Dr. M. Hutter, Dr. M. Lill, R. Staritzbichler und T. Frigato für die vielen Diskussionen und Hilfestellungen. Besonders bedanken für die gute Zusammenarbeit möchte ich mich bei Dr. D. Flöck. Außerdem danke ich Dr. T. Geyer, ohne den viele der vorgestellten Simulationen und Resultate nicht möglich gewesen wären.

Ich danke auch allen, die das Manuskript korrektur gelesen haben.

Finanziell unterstützt wurde diese Arbeit von der Klaus Tschira Stiftung gGmbH.

Lebenslauf



- 26.12.1971 Geboren in Dinslaken (Niederrhein)
- 30.08.1982 - 30.06.1991 Ernst Barlach Gymnasium in Dinslaken
- 01.07.1992 - 30.06.1992 Wehrdienst in Delmenhorst
- 01.10.1992 - 30.09.1994 Grundstudium in Physik an der Universität Dortmund
- 01.10.1994 - 31.03.1995 Beginn des Hauptstudiums an der Universität Bonn
- 01.04.1995 - 25.02.1999 Fortführung des Hauptstudiums an der Universität Dortmund und Diplom in Physik
- Dez. 1997 - Dez. 1998 Diplomarbeit bei Priv. Doz. Dr. A. Hirshfeld:
„Erwartungen für Microlensing in Richtung des galaktischen Bulge und der Magellanschen Wolken“
- 01.07.1999 - 31.03.2000 Systemanalytiker bei der Firma Thinking Networks GMI GmbH
- 01.05.2000 - 30.09.2003 Doktorand am Max-Planck-Institut für Biophysik in Frankfurt bei Prof. Dr. Helms
- 01.10.2003 - 30.06.2004 Fortführung und Abschluß der Doktorarbeit am Zentrum für Bioinformatik der Universität des Saarlandes in Saarbrücken bei Prof. Dr. Helms